Plexin-B2 controls the timing of differentiation and the motility of cerebellar granule neurons.

Eljo Van Battum[1,#], Céline Heitz-Marchaland[1], Yvrick Zagar[1], Stéphane Fouquet[1], Rohini Kuner[2] and Alain Chédotal[1]

[1]Sorbonne Université, INSERM, CNRS, Institut de la Vision, 17 Rue Moreau, 75012 Paris, France

[2] Pharmacology Institute, Im Neuenheimer Feld 366, Heidelberg University, Heidelberg, 69118 Germany

#present address: University Medical Center Utrecht, Dept. of Translational Neuroscience, Universiteitsweg 100, 3584 CG Utrecht, The Netherlands

Lead contact and corresponding author: alain.chedotal@inserm.fr

Summary

Plexin-B2 deletion leads to aberrant lamination of cerebellar granule neurons (CGNs) and Purkinje cells. Although in the cerebellum Plexin-B2 is only expressed by proliferating CGN precursors in the outer external granule layer (oEGL), its function in CGN development is still elusive. Here, we used 3D imaging, *in vivo* electroporation and live-imaging techniques to study CGN development in novel cerebellum-specific *Plxnb2* conditional knockout mice. We show that proliferating CGNs in *Plxnb2* mutants not only escape the oEGL and mix with newborn postmitotic CGNs. Furthermore, motility of mitotic precursors and early postmitotic CGNs is altered. Together, this leads to the formation of ectopic patches of CGNs at the cerebellar surface and an intermingling of normally time-stamped parallel fibers in the molecular layer (ML), and aberrant arborization of Purkinje cell dendrites. There results suggest that Plexin-B2 restricts CGN motility and might have a function in cytokinesis.

Introduction

Plexins are single-pass transmembrane receptors for Semaphorins regulating cell-cell interactions in normal and pathological contexts (Pasterkamp, 2012; Tamagnone et al., 1999; Worzfeld and Offermanns, 2014). In the developing central nervous system (CNS), Semaphorin/Plexin signalling has been involved in axon guidance and regeneration, neuronal migration (Pasterkamp, 2012; Sekine et al., 2019; Yoshida, 2012) and synaptogenesis (Hung et al., 2010; Kuzirian et al., 2013; Molofsky et al., 2014; Orr et al., 2017; Pecho-Vrieseling et al., 2009). There is also evidence linking plexins to a variety of neurological diseases such as autism spectrum disorders, multiple sclerosis, Alzheimer's, pathological pain and spinal cord injury (van Battum et al., 2015; Binamé et al., 2019; Paldy et al., 2017; Zhou et al., 2020).

B-type plexins form a small subclass of plexins, with 3 members (Plexin-B1, -B2 and -B3) in mammals (Pasterkamp, 2012; Worzfeld et al., 2004). B-type plexins are not only expressed by neurons but also astrocytes and oligodendrocytes, with some overlapping expression. Like all plexins, their cytoplasmic domain contains a GTPase activating protein (GAP) in which a Rho-binding domain (RBD) is embedded (Oinuma, 2004; Seiradake et al., 2016; Tong et al., 2007). Their C-terminal region also interacts with the PDZ (PSD-95, Dlg-1 and ZO-1) domains of two guanine nucleotide exchange factors (GEF), PDZeRhoGEF and leukemia-associated RhoGEF (LARG) (Pascoe et al., 2015; Perrot et al., 2002; Seiradake et al., 2016; Swiercz et al., 2002). Plexin dimerization is induced by Semaphorin binding and activates GAP activity, but dimerization was reported to be weaker for Plexin-B2 which might primarily act as a monomer (Wang et al., 2012; Zhang et al., 2015). Class 4 transmembrane semaphorins are the main ligands for B-type plexins

(Pasterkamp, 2012; Seiradake et al., 2016; Tamagnone et al., 1999) but Plexin-B1 and Plexin-B2 were also shown to interact with the receptor tyrosine kinases ErbB-2 and MET (Giordano et al., 2002; Swiercz et al., 2004). It was also recently demonstrated that Plexin-B2 is a receptor for angiogenin, a secreted ribonuclease involved in angiogenesis and amyotrophic lateral sclerosis (Subramanian et al., 2008; Yu et al., 2017).

Knockout mice for all B-type plexins have been generated but surprisingly, no major brain anomalies have been detected so far in *Plxnb1* (Deng et al., 2007) and *Plxnb3* (Worzfeld et al., 2009) knockouts. However, altered photoreceptor outer segment phagocytosis in the retina (Bulloj et al., 2018) and abnormal migration of Gonadotropin hormone releasing hormone neurons to the hypothalamus (Giacobini et al., 2008) were reported in *Plxnb1* knockouts. In contrast, *Plxnb2* knockout mice display severe CNS defects including exencephaly and increased apoptosis (Deng et al., 2007; Friedel et al., 2007), nociceptive hypersensitivity (Paldy et al., 2017) and fear response (Simonetti et al., 2019).

The most striking neurodevelopmental defect reported in *Plxnb2* knockout mice is a severe disorganization of the layering and foliation of the cerebellar cortex (Deng et al., 2007; Friedel et al., 2007; Maier et al., 2011; Worzfeld et al., 2014). The cerebellum contains a limited and well characterized number of neuronal types (about 9) and its cortex has only 3 layers: the inner granular layer (IGL), the deepest one, contains granule cells (CGNs), the Purkinje cell layer, and most externally, the molecular layer, which hosts Purkinje cell dendrites, CGN axons and two types of interneurons, the stellate and basket cells (Sotelo, 2011; Voogd, 2003). Purkinje cell axons are the sole output of the cerebellar cortex. Cerebellar neurons originate from the ventricular zone of the cerebellum primordium, except CGNs and unipolar brush

cells that arise in the so-called upper rhombic lip (Leto et al., 2016). In the mouse brain, cerebellar CGNs account for about half of the neurons all generated after birth from progenitors localized in a transient neuroepithelium, the external granular layer (EGL), occupying the surface of the cerebellum until about the third postnatal week (Chédotal, 2010). The EGL develops embryonically as CGN precursors migrate from the rhombic lip to colonize the surface of the cerebellar anlage (Miale and Sidman, 1961). Symmetrical division amplifies the pool of precursors until birth, after which they start dividing asymmetrically to generate CGNs. Post-mitotic CGNs segregate from dividing precursors and move inward splitting the EGL into two sublayers: the outer EGL (oEGL) containing proliferating cells, and the inner EGL (iEGL) containing newly born CGNs. In the iEGL, CGNs migrate tangentially (parallel to the cerebellar surface), grow two processes (their presumptive axons or parallel fibers) and adopt a bipolar morphology (Komuro et al., 2001; Ramón y Cajal, 1909). CGNs next extend a third process perpendicular to the surface, which attaches to Bergmann glia fibers and guide the inward radial migration of CGNs across the molecular layer to the inner granule cell layer. Strikingly, Plexin-B2 is only expressed in the oEGL and downregulated in post-mitotic CGNs (Friedel et al., 2007). The phenotypic analysis of two *Plxnb2* complete knockout lines showed that the lack of Plexin-B2 maintains some migrating CGNs in a proliferating state which leads to a massive disorganization of cerebellar cortex layers (Deng et al., 2007; Friedel et al., 2007). This phenotype has been also observed in a conditional knockout lacking Plexin-B2 in CGN precursors (Worzfeld et al., 2014). However, the exact consequences of Plexin-B2 deficiency on CGN development are unknown and were not studied at a cellular level. Here, we used a combination of 3D imaging, *in vivo* electroporation and live imaging to study the development of CGNs in cerebellum-specific conditional

knockouts. We show that the transition from a multipolar to a bipolar morphology, the migration speed and CGN axon distribution are altered in absence of Plexin-B2.

Results

Cerebellum specific inactivation of Plxnb2 affects foliation and lamination

In the mouse cerebellum, which matures during the first 3 postnatal weeks, proliferating CGN precursors in the EGL, which can be labeled using 5-Ethynyl-2'-deoxyuridine (EdU), express Plexin-B2 (Friedel et al., 2007; Worzfeld et al., 2004) (Figure 1A, B). Plexin-B2 expression diminishes when CGNs start to migrate in a tangential direction (Figure 1B). As the EGL resorbs (Figure 1C) and becomes depleted of CGN precursors and post-mitotic CGNs, Plexin-B2 expression progressively disappears (Figure 1C). As previously shown, a small fraction of *Plxnb2*$^{-/-}$ mutant mice, bred in the CD1 background, survive and display severe cerebellar disorganization (Friedel et al., 2007; Maier et al., 2011)(Figure 1D).

To circumvent lethality of the *Plxnb2* full knockout mouse model, a *Plxnb2* gene with floxed exons 19-23 (Figure 1E, Worzfeld *et al.*, 2014) was crossed with *Engrailed En1*^{Cre} and *Wnt1-Cre* lines (see methods). Under the *En1* promoter, *Cre* is driven in all mesencephalon and rhombomere 1 leading to expression in the midbrain, a part of the hindbrain and the entire cerebellum (Kimmel et al., 2000; Zervas et al., 2004). Under the *Wnt1* promoter, *Cre* is initially expressed in the cerebellum by CGNs and sparsely in other cell types in the cerebellum (Nichols and Bruce, 2006). Both *En1*^{Cre}*;Plxnb2*$^{fl/fl}$ and *Wnt1-Cre;Plxnb2*$^{fl/fl}$ lines were viable. *In situ* hybridization with a *Plxnb2* probe encompassing exons 19-23, confirmed that, unlike in *Plxnb2*$^{fl/fl}$ controls, *Plxnb2* expression was undetectable in the EGL of *En1*^{Cre}*;Plxnb2*$^{fl/fl}$ and *Wnt1-Cre;Plxnb2*$^{fl/fl}$ mice (Figure 1F). In addition, the EGL of *En1*^{Cre}*;Plxnb2*$^{fl/fl}$ (P5) and

Wnt1-Cre;Plxnb2$^{fl/fl}$ (P7) cerebellum was completely devoid of Plexin-B2 protein immunoreactivity (Figure 1G). Importantly, a severe disorganization of the foliation and layering of the cerebellum was observed in both conditional knockouts (Figure 1F, G, H) which phenocopied what has been previously reported in the *Plxnb2* null knockout (Figure 1B, Friedel *et al.*, 2007). The mutant Purkinje cell layer (visualized using anti-Calbindin (CaBP) immunostaining, Figure 1H) showed the characteristic Purkinje cell islets, and the IGL appeared very disorganized. We focused for the rest of the study on *En1*^{Cre}*;Plxnb2*$^{fl/fl}$ knockouts as En1 has a more restricted expression than Wnt1 (which is expressed in all sensory ganglia), and *En1*^{Cre}*;Plxnb2*$^{fl/fl}$ mice displayed a more severe cerebellar phenotype. Moreover, midbrain defects were reported in *Wnt1-Cre* mice (Lewis et al., 2013).

We next studied the postnatal development of cerebellum lamination and folding in *En1*^{Cre}*;Plxnb2*$^{fl/fl}$ mutants. A striking delay in the formation of the cerebellar fissures was observed in *En1*^{Cre}*;Plxnb2*$^{fl/fl}$ mutant mice, which was already visible at birth (Figure 2A). In normal mice, the principle cerebellar fissures start to appear from E17.5 onwards (Sudarov and Joyner, 2007). Whereas in control animals the 6 principal cerebellar fissures were clearly visible at P0, the cerebellum remained smooth in the *Plxnb2* mutant (Figure 2A). Even if most fissures eventually emerged after P4 in *En1*^{Cre}*;Plxnb2*$^{fl/fl}$, they were not as deep as in *Plxnb2*$^{fl/fl}$ controls (Figure 2A). Another hallmark of the phenotype described for *Plxnb2*$^{-/-}$ mice are ectopic islets of Purkinje cells in the midst of the IGL (Friedel et al., 2007). In *En1*^{Cre}*;Plxnb2*$^{fl/fl}$ cKO cerebella displaced PCs were first detected at P2 but became more conspicuous from P4 (Figure 2A).

To better comprehend the cerebellar alterations in *En1*^{Cre}*;Plxnb2*$^{fl/fl}$ cerebellum we performed 3D light sheet fluorescence microscopy (LSFM) of iDISCO+ cleared brains

(Renier et al., 2016). Nuclear TO-PRO-3 staining confirmed the altered fissure formation in P4 cerebellum and also showed the development of additional folds of the IGL perpendicular to the main fissures (Figure 2B). Despite the aberrant folds, CGNs and Purkinje cell lamination was grossly preserved (Video 1).

As cerebellar development progresses, the *Plxnb2* mutant phenotype became more severe. In P14 controls, cerebellar fissures were fully developed, the EGL was almost absent and IGL structure was very smooth and homogeneous (Figure 3A). In contrast, *Plxnb2* mutants showed patches of CGNs remaining at the cerebellar surface, an IGL structure with many invaginations in different orientations, and original fissures could not be defined easily (Figure 3B, Video 2). The aberrant IGL structure and the patches of granule cells at the surface persisted in adult, well after cerebellar development was completed (Figure 3C, D, Video 3). All aberrant IGL folds in the *Plxnb2* mutant were lined with a monolayer of Purkinje cells (Video 4). These 3D-data convey that the Purkinje cell 'islets' observed in *Plxnb2* mutant cerebellar sections actually correspond to stretches of Purkinje cells that line the heavily corrugated, but still continuous IGL.

Because *Plxnb2* mutant cerebella seemed to be smaller than controls on sections, we next analyzed the cerebellar volume in 3D. Indeed, a limited, but significant reduction was observed throughout cerebellar development (Figure 3-figure supplement 1A).

Plxnb2 mutant did not display any noticeable motor or behavioral defects and their performance on an accelerating rotarod was similar to control mice (Figure 3-figure supplement 1B).

Plxnb2 mutant CGNs disorganize the EGL and proliferate slightly different

Since in the cerebellum, Plexin-B2 is only expressed in proliferating CGN precursors in the EGL, we characterized the cellular organization of this layer in more detail. We visualized the outer layer of proliferating CGNs in the EGL by injecting P9 mouse pups with EdU 2 hours before perfusing them (Figure 4A). Purkinje cells were immunostained with anti-CaBP (Figure 4A). In controls, whereas EdU^+ CGN precursors were usually confined to the thin outer EGL (oEGL), they were more dispersed in *Plxnb2* mutants (Figure 4A). In addition, the developing ML was much thinner (Figure 4A). We next performed double immunostaining for Ki67, a marker of proliferating precursors, and Tag-1 (Transient axonal glycoprotein 1, also known as Contactin-2), which labels tangentially migrating CGNs in the iEGL (Figure 4B). In control P9 cerebellum, both markers were segregated (Figure 4B), whereas in *Plxnb2* mutants, CGN precursors lost their confinement to the oEGL and intermingled with tangentially migrating $Tag1^+$ CGNs in the iEGL (Figure 4B). However, as Ki67 and Tag1 are expressed in different cell compartments (nucleus and cell surface respectively), we could not determine if some of the Tag1+ cells were also Ki67+.

These results lead us to investigate potential differences in *Plxnb2* mutant CGN precursor proliferation. Mice were given a short (2 h before fixation at P8) or a long (24 h before fixation at P8) EdU pulse, and the number of EdU-positive cells in the EGL was counted (Figure 4C, Figure 4-figure supplement 1A). No difference in the amount of EdU positive cells was detected for either time of EdU administration, and there was no difference in the uptake of EdU by dividing cells over time (Figure 4C). In addition, the quantification of the amount of EdU^+ CGNs in the EGL (EdU injected 2h before brain collection) that colocalized with Ki67 immunostaining did not show a difference in proliferation rate in *Plxnb2*-mutant brains (Figure 4-figure supplement 1B). Since it is estimated that CGN precursors divide approximately every 20h

(Espinosa and Luo, 2008), cerebellum sections of pups injected with EdU were stained after 24 h for Phospho-histone H3 (H3P), an M-phase marker. This enabled us to quantity the proportion of cells that took up EdU the day before (and theoretically should have ended division hours ago) and were still in their cycle. Interestingly, we observed a significant increase in the percentage of cells double-positive for EdU and H3P (Figure 4D). This implies that the cell cycle for *Plxnb2* mutant CGNs is slightly longer. Together, these results suggest that there is probably no alteration of cell cycle progression in absence of Plexin-B2 although more experiments will be required to determine if the M phase is affected.

Migrating Plxnb2 mutant CGNs show different morphology and proliferation markers

The high cell density of the EGL makes it difficult to follow the morphological changes that developing CGNs undergo during the different steps of their development. To follow newborn CGNs throughout their developmental sequence, we targeted CGNs in the EGL of P7 mouse pups with GFP using *in vivo* electroporation (Figure 5A). By adapting a tripolar electrode electroporation technique developed for embryos (dal Maschio et al., 2012) to postnatal mice, we could reproducibly target a wide area of the dorsal cerebellum. With this method 99.6% of all targeted GFP^+ cells in the cerebellum were CGNs and co-expressed Pax6 (Figure 5-figure supplement 1A). The developmental sequence of CGNs is stereotypically phased, and by collecting cerebella at specific time-points post-electroporation we could study their morphological evolution, from precursors to tangential migrating cells, radial migrating cells, and maturing CGNs in the IGL (Figure 5B). After 24 hours, most electroporated GFP^+ CGNs were in the tangential phase, while some still resided in

239 the oEGL. Two days after electroporation, GFP$^+$ CGNs had started radial migration,
240 and extended parallel fibers (adopting a characteristic T-shape, Figure 5B).
241 Subsequently, one week after electroporation, all GFP$^+$ CGNs had reached the IGL
242 and started the process of dendritogenesis. Eventually, all GFP$^+$ CGNs displayed
243 their stereotypical morphology with a small cell body bearing 3-4 claw-shaped
244 dendrites (Figure 5B).
245 By comparing the initial steps of postmitotic CGN development, we found a
246 significant reduction in the length of the processes (and future parallel fibers)
247 extended by tangentially migrating CGNs in *Plxnb2* mutants compared to controls
248 (Figure 5C, D). Cell body size and shape for proliferating and tangentially migrating
249 CGNs was similar in both genotypes (Figure 5-figure supplement 1B). As implied by
250 the EdU and Ki67/Tag1 immunohistochemistry (Figure 4A, B), we observed that
251 GFP$^+$ CGN precursors intermingled with migrating bipolar CGNs in the EGL of
252 *Plxnb2* mutant animals (Figure 5C). Indeed, quantification of the location of multipolar
253 and bipolar CGNs in the outer, inner EGL or ML, shows that multipolar and bipolar
254 CGNs in the *Plxnb2* mutant were spread throughout the EGL and that bipolar CGNs
255 sometimes even resided in the ML (Figure 5-figure supplement 1C). Intriguingly, in
256 *Plxnb2* mutants, a fraction of the bipolar and tangentially migrating GFP$^+$ CGNs, were
257 also labeled with EdU (which only labels dividing cells), administered 2 hours before
258 fixation. By contrast, only a very small fraction of tangentially migrating bipolar GFP$^+$
259 CGNs were found in controls (Figure 5C, E). When combining the EdU staining with
260 H3P to mark acutely dividing cells, we could confirm that, although rare, some of the
261 bipolar GFP$^+$/EdU$^+$ were indeed proliferating (Figure 5-figure supplement 1D). Some
262 bipolar GFP$^+$ CGNs also co-expressed H3P and Tag-1 (Figure 5F). This suggests
263 that in *Plxnb2* mutants, the CGN switch from proliferation to tangential migration is

altered and that these two phases are not spatio-temporally separated anymore. To further support this hypothesis, we next analyzed GFP^+ CGNs 48 hours after electroporation. Again, there was a significant reduction in the proportion of CGNs that had initiated radial migration in *Plxnb2* mutants (Figure 5G). This, together with the slight delay in M-phase (Figure 4D), suggest that *Plxnb2*-deficient CGNs might remain longer in both their proliferative and tangential phases.

As soon as *Plxnb2* mutant CGNs started radial migration, their morphology closely resembled that of control CGNs. Differences in leading process length were no longer observed, and their ascending axons in the ML were of comparable length (Figure 5-figure supplement 1E). At this radial stage in both control and mutant GFP^+ CGNs, proliferation markers were seldom observed (Figure 5G). Conversely, during radial migration, CGN cell bodies had a slightly more circular shape in *Plxnb2* mutants (Figure 5-figure supplement 1E). Moreover, in *Plxnb2* mutants, CGNs in the IGL acquired their stereotypical CGN morphology with a cell body of 7-8 µm in diameter bearing 3-4 claw-shaped primary dendrites, slightly faster than in controls (Figure 5-figure supplement 1F, G). Together, this suggests that in the IGL, CGNs might differentiate faster in *Plxnb2* mutants than in controls.

After completion of cerebellar development, *Plxnb2* mutant CGNs displayed strikingly disorganized parallel fibers (Figure 5H, Videos 5 and 6). Instead of being restricted to a thin sub-layer of the ML in controls, parallel fibers were more spread out in *Plxnb2* mutants. Some CGN axons were even completely misprojecting deep into the cerebellar white matter where they run along myelinated Purkinje cell axons and mossy fibers (Figure 5F, 5F-II and Figure 5-figure supplement 2A). The ectopic CGN axons keep some of their normal characteristics since they did not get myelinated (Figure 5-figure supplement 2A, B). In the IGL of *Plxnb2* mutants, the labeled CGNs

were more dispersed, and some formed patches at the cerebellar surface (Figure 5G, 5H-III).

According to the 'stacking model', developing parallel fibers accumulate in the ML in an inside-out time sequence, with CGNs born later extending parallel fibers above those of earlier born CGNs (Espinosa and Luo, 2008). The dispersion of proliferating CGNs in the *Plxnb2* mutants EGL together with the presence of proliferation markers in tangentially migrating CGNS, suggest that their developmental clock is perturbed. Accordingly, *Plxnb2* mutant parallel fibers were much more scattered across the ML. To better visualize the spatiotemporal organization of parallel fibers in the ML, we electroporated a GFP-expressing vector at P7, followed by a td-Tomato-expression vector at P11. With this method, we could label two pools of early-born (GFP^+) and late-born ($Tomato^+$) CGNs in the same mouse (Figure 6A). As expected, GFP^+ and $Tomato^+$ parallel fibers were clearly segregated in control mice. Strikingly, in *Plxnb2* mutants, parallel fibers lost this inside-out organization in the ML (Figure 6A). At P11, early GFP^+ fibers occupied a space within the ML twice larger than in controls and largely overlap with later-born $Tomato^+$ parallel fibers, which were also more spread than in controls (Figure 6A).

We next explored the development of Purkinje cell dendritic arbors and their connections with parallel fibers. Immunohistochemistry of thick sagittal sections made of cerebella 48 hours after electroporation with GFP, showed that the distal tips of Purkinje cell dendrites reached until the newly formed GFP^+ CGN processes (the forebears of parallel fibers) at the border of the EGL and ML (Figure 6B, Figure 6-figure supplement 1A). $Vglut1^+$ puncta, specific to CGN-Purkinje synapses, were distributed in a proximal-to-distal gradient: high at the trunk of the Purkinje dendritic tree, and low at the distal branches (Figure 6-figure supplement 1A). In P9 *Plxnb2*

mutants, the young GFP$^+$ parallel fibers ran throughout the entire ML between the Purkinje cell dendrites, which in turn appeared disorganized and more branched than controls. Interestingly, in *Plxnb2* mutants, Vglut1$^+$ synapses extended to the tip of the Purkinje cell dendrites. We quantified the ratio between Vglut1$^+$ puncta (fluorescent integrated density) at the distal ends and the proximal base of the dendritic arbor, and found significantly more synapses on the distal end compared to control (Figure 6-figure supplement 1A). At later stages, no difference could be observed in the distribution of CGN-Purkinje synapses (Figure 6-figure supplement 1B).

We next compared the position of the nascent parallel fibers in the cerebellum of control and mutant mice electroporated at P7 (Figure 6B) or P11 (Figure 6C) and collected 2 days later. In controls, nascent parallel fibers extended at the bottom of the iEGL just above the tips of Purkinje dendrites *Plxnb2* mutant brains. Where at P9 the Purkinje cells in the *Plxnb2* mutant seem underdeveloped and developing parallel fibers cross the entire ML (Figure 6B). New parallel fibers crisscrossing deep into the ML were also found in P13 *Plxnb2* mutant, when the ML is much larger and the Purkinje dendrites more developed (Figure 6C).

Plxnb2 mutant CGNs display striking migration phenotype in vitro

To gain more insights into the behavior of *Plxnb2* mutant CGNs, we cultured EGL explants from 4-5-day-old pups. As previously described, CGNs exiting the explants follow a developmental sequence closely resembling *in vivo* CGNs (Kawaji et al., 2004; Kerjan et al., 2005). As in the oEGL, CGN precursors divide inside the explant or close to it (see below and Yacubova and Komuro, 2002). After plating, postmitotic cells become bipolar, grow long neurites and migrate away from the explant by nuclear translocation, as during tangential migration in the iEGL (Figure 7A). 2-3

339 days later, CGNs start aggregating and form satellites around the explant (Figure 7A)
340 (Kawaji et al., 2004). Immunocytochemical analysis of young explants with Pax6, a
341 marker for pre-and postmitotic CGNs, confirmed that the cells migrating away from
342 the explant were CGNs (Figure 7-figure supplement 1A). Although the explant
343 contained GFAP^{+} glial cells extending processes outward, their cell bodies seldom
344 left the explant (Figure 7-figure supplement 1B).
345 We next compared explants from P4-5 *Plxnb2*$^{fl/fl}$ or *En1*^{Cre}*;Plxnb2*$^{fl/fl}$ EGL after 1 day
346 *in vitro* (DIV) and noticed a difference in outward CGN migration. DAPI-stained nuclei
347 from *Plxnb2* mutant CGNs stayed closer to the explant (Figure 7B, C). Furthermore,
348 β-III tubulin staining revealed a difference in neurite outgrowth (Figure 7B), with
349 shorter and more fasciculated neurites in *Plxnb2* mutants. To better analyze the
350 morphology of individual CGNs, we labeled a subset of CGNs with GFP by *ex vivo*
351 electroporation just prior to dissecting the cerebella for EGL cultures. Almost all GFP^{+}
352 cells were positive for CGN markers such as Pax6 (Figure 7-figure supplement 2A)
353 and Sema6A (Figure 7-figure supplement 2B), and did not resemble GFAP^{+} glial
354 cells (Figure 7-figure supplement 2C). In controls, GFP^{+} CGNs migrating away from
355 the explant at DIV1 either had a bipolar morphology, with ovoid cell bodies and long
356 processes, or were more roundish cells without clear polarity and only short
357 protrusions (Figure 7D). These multipolar cells, are probably CGN precursors as
358 previously proposed (Yacubova and Komuro, 2002). Strikingly, at DIV1 in *Plxnb2*
359 mutant explant cultures, the proportion of multipolar GFP^{+} CGNs was significantly
360 increased (65.42 ± 2.37% in mut *vs.* 48.88 ± 2.65% in ctl, MWU(353) $p < 0.0001$) and
361 the proportion of bipolar cells was decreased (Figure 7D, E). However, by DIV2
362 almost all cells - control or mutant - had a bipolar morphology (Figure 7D, E).
363 Interestingly, as observed *in vivo* (Figure 5C), DIV1 bipolar *Plxnb2* mutant CGNs had

364 shorter processes than control cells (Figure 7D, F). Finally, bipolar cells could be
365 further subdivided into two categories: cells that connected with their trailing process
366 to the original explant, and cells that were disconnected from the explant.
367 Interestingly, at DIV2, *Plxnb2* mutant had a higher proportion of GFP^+ CGNs that
368 were not attached to the explant (Figure 7D, G).
369 To better evaluate the consequence of *Plxnb2* deletion on the migration of bipolar
370 CGNs, we next performed time-lapse video-microscopy of DIV1 and DIV2 EGL
371 explant cultures. Interestingly, whereas control GFP^+ CGNs usually migrated away
372 from the explant in a straight and radial direction, *Plxnb2* mutant GFP^+ CGNs
373 sometimes reversed direction one or even multiple times during the acquisition
374 period (Figure 8A, Video 7). The afore-mentioned difference in CGN process lengths
375 during tangential migration could also be observed in Videos. Although the speed of
376 migrating bipolar CGNs was not changed (Figure 8B), both the relative amount of
377 distance and time going in negative direction (moving back towards the explant) were
378 significantly increased in *Plxnb2* mutant CGNs (Figure 8C). These results probably
379 explain why in fixed DIV1 cultures, *Plxnb2* mutant CGN nuclei appear closer to the
380 explant (Figure 7B).
381 Taken together, both our *in vivo* and *in vitro* data support an abnormal outgrowth of
382 processes in *Plxnb2*-deficient tangentially migrating CGNs.
383
384 ***Plxnb2 mutant CGN precursors show aberrant proliferation and movement***
385 Since we observed slight differences in cell-cycle completion and an aberrant
386 localization of proliferating precursors in EGL sections (Figure 4), we also aimed at
387 analyzing proliferation in EGL explant cultures. EdU was added to the medium 2
388 hours before fixation (Figure 9A). Although there was a much lower amount of DAPI

nuclei visible around the explant (Figure 9A, B), a similar amount of EdU-positive nuclei was observed (Figure 9A, C). In addition, the explants did not show a difference in EdU-positive nuclei that also stained for H3P (Figure 9A, D).

With longer application of EdU, there was still no difference in the distribution of EdU between multipolar and bipolar cells at DIV1 (Figure 9E, F). Nevertheless, a larger portion of multipolar cells was positive for EdU (Figure 9F), suggesting that these multipolar cells actually were CGN precursors that escaped from the explant. Interestingly, at DIV2, many more cells with a bipolar appearance had an EdU-positive nucleus in *Plxnb2* mutant explants (Figure 9E, G). Therefore, these data suggest that in mutant explants, bipolar cells are still generated long after the explants are seeded, suggesting that the *in vitro* proliferation of CGN precursors is differentially phased compared to controls.

Intrigued by the potential precursor properties of the multipolar GFP^+ CGNs in the cultures, we attempted to follow their behavior in our time-lapse recordings. As evident from the fixed cultures, the proportion of multipolar cells at the beginning of the time-lapse acquisition period (at DIV1) was twice as big in mutant explants compared to control (Figure 10-figure supplement 1B). At the end of the time-lapse acquisition period (around DIV2) almost all control cells reached a bipolar state, whereas in *Plxnb2* mutant explants a large portion still appeared multipolar (Figure 10-figure supplement 1B). The time-lapse acquisitions of multipolar CGNs confirmed their ability to proliferate. They divided and produced two daughter cells that became bipolar and henceforth commenced their tangential migration phase (Figure 10A, Video 8). This confirms that multipolar cells are probably CGN precusors. Before they divided, *Plxnb2* mutant multipolar CGNs showed a striking increase of movement compared to controls (Figure 10B, C). The presence of at least twice as much

multipolar CGNs moving around mutant explants compared to controls (Figure 10-figure supplement 1), probably explained why more multipolar cell divisions per explant were counted throughout the acquisition period (Figure 10D). We never observed more than one division of a single multipolar cell in our acquisitions, and whenever visible, all daughter cells eventually adopted a bipolar shape and started migration. However, we found that the time taken by the daughter cells to become bipolar after cytokinesis was increased in mutants compared to controls (Figure 10E). During this in-between period the daughter cells were again very motile and they appeared to struggle to become polarized (Video 8).

Discussion

Revisiting Plexin-B2 function in cerebellum development at a cellular level

Cerebellar granule cells are one of the best models to study neuronal migration as they display a large palette of migratory behavior at embryonic and postnatal stages (Chédotal, 2010). Our work confirms that the expression pattern and function of the Plexin-B2 receptor in CGN development, is quite unique. Plexin-B2 is only expressed in proliferating CGN precursors and silenced as soon as CGNs enter the iEGL and initiate their migration. Previous studies have shown that molecular layer organization is severely perturbed in Plexin-B2 knockouts (Deng et al., 2007; Friedel et al., 2007). Here, we used two distinct Cre lines (*En1*^{Cre} and *Wnt1-Cre*) to silence *Plxnb2* function in the EGL and show that they fully phenocopy the null allele but have a normal viability. This, together with similar observation made with the *Atoh1cre* line (Worzfeld et al., 2014) and our time-lapse studies in EGL explants, shows that *Plxnb2* acts cell autonomously in cerebellar CGN precursors. However, the

consequence of Plexin-B2 deficiency at cellular and subcellular levels were unknown as the extremely high number and density of cerebellar CGNs, as well as their molecular and genetic homogeneity do not facilitate the *in situ* analysis of the evolution of their morphology during development. Here, we show that the use of a tripolar electrode is an optimal method to express transgenes in postnatal CGNs. Mosaic analysis with double markers (MDAM) can reveal the individual morphology of developing CGNs but it requires specific lines and complex genetic crosses (Zong et al., 2005). Viral vectors have been used to express fluorescent proteins in developing CGNs but the delay between the infection and the transgene expression does not allow to observe the early phases of CGN development in the EGL (Park et al., 2019). The size of the transgene is also limited. In rodents, CGNs are produced postnatally and the superficial location of the EGL under the skull makes it easily accessible. Therefore, direct electroporation of plasmids into the cerebellum using tweezer electrodes has been performed to target developing CGNs *ex vivo* (Govek et al., 2018; Renaud and Chédotal, 2014) or *in vivo* (Konishi et al., 2004; Umeshima et al., 2007). Here we have successfully adapted a triple electrode method, previously designed to target ventricular zone progenitors in the embryonic cerebellum (dal Maschio et al., 2012), to express fluorescent proteins in a large domain of the postnatal EGL covering multiple folia. The methods have been used between birth and at least P11 with comparable outcome. Importantly, we show that it allows multiple rounds of electroporation at different time-points, which allows to study parallel fiber layering in the molecular layer without viral vectors or MADM lines.

The analysis of CGN morphology with GFP electroporation, showed that in absence of Plexin-B2, CGNs still follow the normal sequence of differentiation that in controls (Komuro et al., 2001; Renaud and Chédotal, 2014). They become bipolar, migrate

tangentially, then tripolar and migrate radially across the molecular layer leaving behind parallel fibers. They also extend 3-4 dendrites undistinguishable from controls. However, it also shows that their parallel fibers are not properly layered and that some CGN axons are lost in the white matter. Interestingly, our results suggest that the mislocalized CGN axons remain unmyelinated in agreement with previous studies showing that axons have a unique profile of myelination (Tomassy et al., 2014).

Plexin-B2 controls the timing of cell division in the EGL

Our results show that the size of the cerebellum is only slightly reduced in *En1*^{Cre}*;Plxnb2*$^{fl/fl}$ mice thereby indicating that the generation of cerebellar neurons is almost unaffected by the lack of Plexin-B2. In addition, a significant fraction of tangentially migrating CGNs are still mitotically active in the EGL indicating that CGN precursors initiated differentiation before the completion of cell division. Interestingly, we also found that in EGL explant cultures the number of mitotically active CGNs with multipolar morphology is three times higher in *Plxnb2* mutant. Moreover, the time taken by the daughter cells to become bipolar after cytokinesis is increased in mutants compared to controls. This suggests that *Plxnb2* mutant CGNs might be maintained for a longer time in a multipolar and proliferating state, and that their ability to perform their final division could be altered, although they ultimately divide and produce a close to normal number of daughter cells. These results support a role for Plexin-B2 in cell division as previously described in cancer cell lines (Gurrapu et al., 2018) and in the developing kidney (Xia et al., 2015) where Plexin-B2 controls the orientation of the mitotic spindle. Interestingly, several studies suggest that plexins could control abscission, the final step of cell division, by promoting cytoskeleton

disassembly at the intercellular bridge linking the two daughter cells. MICALs (molecule interacting with CasL) are oxidoreductases which regulate actin depolymerization and act directly (Van Battum et al., 2014; Terman et al., 2002) or indirectly (Ayoob, 2006; Orr et al., 2017) downstream of plexins (Pasterkamp, 2012; Seiradake et al., 2016). Interestingly, MICALs have been shown to control F-actin clearance during abscission (Frémont et al., 2017). Likewise, LARG, which associates with B-type plexins (Pascoe et al., 2015) is required for abscission in Hela cells (Martz et al., 2013). Although hypothetical, an involvement of Plexin-B2 in cytokinesis is also supported by a recent proteomic study which identified Plexin-B2 as one of the 489 proteins constituting the midbody, the large protein complex at the center of the intercellular bridge linking dividing cells (Addi et al., 2020). Of note, patients with mutations in citron kinase, a key component of the abscission machinery, display a severe disorganization of cerebellar cortex including the ectopic patches of CGNs observed in *Plxnb2* mutants (Harding et al., 2016; Li et al., 2016). Together, these results suggest that Plexin-B2 might control cell division in the outer EGL, a process which is also essential for orchestrating cerebellar foliation (Legue et al., 2015; Otero et al., 2013).

Plexin-B2 controls CGN migration

Our present study also shows that Plexin-B2 influences the migration of cerebellar CGNs. The overall distance reached by CGNs in EGL explants cultures is reduced in *Plxnb*2 mutants, as previously described (Maier et al., 2011). Although delayed cell division probably contributes to this defect, it cannot be explained by a slower tangential migration, as our time-lapse analysis rather indicates that in *Plxnb2* mutants, multipolar CGNs are more motile, and cover twice as much cumulative

distance than in controls. Moreover, in *Plxnb2* mutants, tangentially migrating bipolar CGNs alternate between forward (away from the explant) and rearward direction while control CGNs essentially migrate forward in this culture setup. The significant increase of multipolar and mitotically active CGNs, migrating around the explants suggest that CGN precursors become more motile without Plexin-B2.

Our data also provide evidence for altered CGN migration *in vivo*. The combination of GFP electroporation and EdU labelling shows that in *Plxnb2* mutants, CGNs remain for a longer time in tangential migration and that they take longer to initiate their radial migration. Moreover, tangentially migrating CGNs mix with CGN precursors and a significant fraction divides during tangential migration. These observations are in good agreement with previous studies which reported enhanced motility of *Plxnb2*$^{-/-}$ macrophages (Roney et al., 2011) and neuroblasts in the rostral migratory stream (Saha et al., 2012). Sema4D and Plexin-B2 were also reported to function as motogens for newborn cortical neurons (Hirschberg et al., 2010). A recent study also linked Plexin-B2 to microglial cell motility in the injured spinal cord, albeit negatively (Zhou et al., 2020). Together, these results show that in many developing tissue, Plexin-B2 is a key regulator of cell migration decisions.

What could be the ligands and downstream partners mediating Plexin-B2 function in CGNs?

Our results confirm the essential and unique function of Plexin-B2 in granule cell development but the underlying molecular mechanisms remains an enigma. At least five of the Class 4 semaphorins (Sema4A, 4B, 4C, 4D and 4G) bind to Plexin-B2 (Deng et al., 2007; Hirschberg et al., 2010; Maier et al., 2011; Tamagnone et al., 1999; Xia et al., 2015; Yukawa et al., 2010). However, knocking down, *Sema4C* and

539 *Sema4G*, the two class 4 semaphorins expressed in the developing cerebellar
540 cortex, results in a mild phenotype (Friedel et al., 2007; Maier et al., 2011). This
541 suggests that additional semaphorins could act redundantly or that other Plexin-B2
542 ligands could be involved. Angiogenin was recently shown to bind and signal through
543 Plexin-B2 ligand in various cell types, but angiogenin does not activate the same
544 pathways as class 4 semaphorins downstream of Plexin-B2 (Yu et al., 2017).
545 Therefore, and although its expression in the developing cerebellum is unknown,
546 angiogenin is unlikely to mediate Plexin-B2 function in the EGL. In addition, a
547 spontaneous monkey mutant of angiogenin, does not display cerebellum defects
548 (Zhang and Zhang, 2003).
549 Elegant genetic studies showed that the GAP and RBD domains of Plexin-B2, which
550 mediate semaphorin activity, are essential for Plexin-B2 function in developing
551 CGNs, but that the PDZ binding domain is dispensable (Worzfeld et al., 2014). I*n*
552 *vitro* experiments suggested that the RBD domain of B-type plexins regulates their
553 activity by interacting with Rho family small GTPases such as Ras, Rac1, Rnd1-3
554 and Rap1 (Oinuma, 2004; Rohm et al., 2000; Tong et al., 2007; Turner et al., 2004;
555 Vikis et al., 2000; Wang et al., 2012, 2013; Wylie et al., 2017; Zanata et al., 2002).
556 However, structural biology studies showed that B-type plexins do not interact with
557 M-Ras/R-Ras (Wang et al., 2012, 2013) and accordingly, *in vivo* evidence indicate
558 that CGN developmental defects in *Plxnb2* mutants do not involve M-Ras/R-Ras
559 (Worzfeld et al., 2014). Rac1 and to a lesser extent Rac3 are expressed in the
560 postnatal EGL (Nakamura et al., 2017), but although their simultaneous inactivation
561 perturbs CGN development, they primarily act on neuritogenesis and tangential
562 migration of CGN precursors in the embryo, unlike Plexin-B2. Plexin-B2 interacts
563 preferentially with Rnd3 (Azzarelli et al., 2014; McColl et al., 2016; Wylie et al., 2017)

and in radially migrating cortical neurons, Plexin-B2 and Rnd3 have antagonistic function (Azzarelli et al., 2014). Although Rnd3 is expressed in EGL (Ballester-Lurbe et al., 2009), the structure of the cerebellum is normal in *Rnd3* knockout mice (Mocholí et al., 2011) (and data not shown). Interestingly, mammalian plexins have a higher GAP activity for Rap1 GTPases (Wang et al., 2012) and Plexin-B2/Rap1 interaction does not required Rnd3 (McColl et al., 2016). Therefore, Rap1 GTPases could be the main Plexin-B2 partners in developing CGNs, regulating the transition of CGN precursors from the oEGL to the iEGL. Accordingly, Rap1A/Rap1B are required for the transition of newborn cortical neurons from a multipolar to a bipolar state and their radial migration (Jossin and Cooper, 2011; Shah et al., 2017). In the dentate gyrus, Plexin-A2 negatively regulates Rap1 in migrating neurons (Zhao et al., 2018). Rap1 expression has been detected in postnatal CGNs (Obara et al., 2007) and therefore it will be interesting in future studies to assess Rap1A/B function in CGN development.

In conclusion, we show here that the timing of expression of Plexin-B2 in CGN precursors in the EGL, sets the pace for cell division and migration and that its downregulation is required for segregating post-mitotic CGNs from cycling precursors. The abnormal association of proliferation and migration in the *Plxnb2* mutant together with an excessive motility probably explain the alteration of foliation and layering observed in *Plxnb2* knockout cerebellum (Legue et al., 2015). Interestingly, the transcription factor Zeb1, is also selectively expressed in CGN precursors in the outer EGL and inhibits the CGN differentiation (Singh et al., 2016). Moreover, it inhibits the expression of Rnd1 and Rnd3 GTPases. It will be interesting to determine if *Plxnb2* is a target of Zeb1.

Acknowledgements

We thank Dr Roland Friedel for providing the *Plxnb2* conditional knockout and Dr Okabe for the pCX plasmid. The authors wish to thank Morgane Belle for invaluable assistance with confocal- and ultramicroscopes and Imaris software, and all members of Alain Chédotal and Xavier Nicol teams for helpful discussions and input during the project. This work was completed with the financial support of the Programme Investissements d'Avenir IHU FOReSIGHT (ANR-18-IAHU-01), and a grant from the Fondation pour la recherche médicale (FRM).

Competing interests

The authors declare no competing interests

Materials and methods

Key Resources Table

Reagent type (species) or resource	Designation	Source or reference	Identifiers	Additional information
strain; strain background (*Mus musculus*)	*En1*^{Cre} (C57BL/6J)	DOI : 10.1101/gad.14.11.1377	*En1*$^{tm2(cre)Wrst}$/J RRID: IMSR_JAX:007916	
strain; strain background (*Mus musculus*)	*Wnt1-Cre* (C57BL/6J)	DOI : 10.1002/dvdy.20611	B6.Cg-*E2f1*$^{tg(Wnt1-cre)2Sor}$/J RRID: IMSR_JAX:022501	
strain; strain background (*Mus musculus*)	*Plxnb2*$^{-/-}$	DOI : 10.1523/JNEUROSCI.4710-06.2007	*Plxnb2*^{tm1Matl} RRID: MGI:4881705	

strain; strain background (*Mus musculus*)	*Plxnb2 cKO*	DOI: 10.1523/JNEUROSCI.4710-06.2007 DOI: 10.1073/pnas.1308418111		Gift from Roland Friedel
antibody	anti-Calbindin D-28k (Rabbit antiserum)	Swant	Cat# CB38, RRID: AB_2721225	IF(1:1000),
antibody	anti-Calbindin D-28k (Mouse monoclonal)	Swant	Cat# 300, RRID: AB_10000347	IF(1:1000)
antibody	anti-Foxp2 (N16) (Goat polyclonal)	Santa Cruz	Cat# sc-21069, RRID: AB_2107124	IF(1:1000)
antibody	anti-Glial fibrillary acidic protein (GFAP) (Mouse monoclonal)	Millipore	Cat# MAB360, RRID:AB_11212597	IF(1:500)
antibody	anti-Green Fluorescent Protein (GFP) (Rabbit polyclonal)	ThermoFisher Scientific	Cat# A-11122, RRID:AB_221569	IF(1:2000)
antibody	anti-Green Fluorescent Protein (GFP) (Chicken polyclonal)	Aves	Cat# GFP-1010, RRID:AB_2307313	IF(1:2000)
antibody	anti-Phospho-Histone H3(Ser10) (Rabbit polyclonal)	Cell Signaling	Cat# 9701; RRID:AB_331535	IF(1:1000)
antibody	anti-Ki67 (Rabbit polyclonal)	Abcam	Cat# Ab15580; RRID: AB_443209	IF(1:500)
antibody	anti-Olig-2 (Rabbit monoclonal)	Millipore	Cat# AB9610; RRID: AB_10141047	IF(1:500)
antibody	anti-Pax6 (Rabbit polyclonal)	Millipore	Cat# AB2237; RRID: AB_1587367	IF(1:1000)

antibody	anti-Plexin-B2 (Armenian Hamster monoclonal)	Novus	Cat# NBP1-43310; RRID: AB_10006672	IF(1:1000)
antibody	anti-Sema6A (Goat polyclonal)	R&D systems	Cat# AF1615; RRID: AB_2185995	IF(1:500)
antibody	anti-Contactin-2/TAG-1 (Goat polyclonal)	R&D systems	Cat# AF4439; RRID: AB_2044647	IF (1:500)
antibody	anti- beta-Tubulin III (Rabbit polyclonal)	Sigma-Aldrich	Cat# T2200; RRID: AB_262133	IF (1:1000)
antibody	anti- VGLUT1 (Guinea pig polyclonal)	Millipore	Cat# AB5905; RRID: AB_2301751	IF (1:3000)
antibody	Donkey Anti-Rabbit IgG (H+L) Alexa Fluor 488	Jackson Immunoresearch	Cat# 711-545-152; RRID: AB_2313584	IF (1:750)
antibody	Donkey Anti-Rabbit IgG (H+L) Cy3	Jackson Immunoresearch	Cat# 711-165-152; RRID:AB_2307443	IF (1:750)
antibody	Donkey Anti-Rabbit IgG (H+L) Alexa Fluor 647	Jackson Immunoresearch	Cat# 711-605-152; RRID:AB_2492288	IF (1:750)
antibody	Bovine Anti-Goat IgG (H+L) Alexa Fluor 647	Jackson Immunoresearch	Cat# 805-605-180; RRID:AB_2340885	IF (1:750)
antibody	Donkey Anti-Goat IgG (H+L) Cy3	Jackson Immunoresearch	Cat# 705-165-147; RRID:AB_2307351	IF (1:750)

antibody	Donkey Anti-Mouse IgG (H+L) Alexa Fluor 647	Jackson Immunoresearch	Cat# 715-605-150; RRID:AB_2340862	IF (1:750)
antibody	Donkey Anti-Chicken IgG (H+L) Alexa Fluor 488	Jackson Immunoresearch	Cat# 703-545-155; RRID:AB_2340375	IF (1:750)
antibody	Donkey Anti-Chicken IgY (H+L) Cy3	Jackson Immunoresearch	Cat# 703-165-155; RRID:AB_2340363	IF (1:750)
antibody	Goat Anti-Armenian Hamster IgG (H+L) Alexa Fluor 488	Jackson Immunoresearch	Cat# 127-545-160; RRID:AB_2338997	IF (1:750)
antibody	Goat Anti-Armenian Hamster IgG (H+L) Cy3	Jackson Immunoresearch	Cat# 127-165-160; RRID:AB_2338989	IF (1:750)
antibody	Donkey Anti-Guinea Pig IgG (H+L) FITC	Jackson Immunoresearch	Cat# 706-095-148; RRID:AB_2340453	IF (1:750)
antibody	Donkey Anti-Guinea Pig IgG (H+L) Cy3	Jackson Immunoresearch	Cat# 706-165-148; RRID:AB_2340460	IF (1:750)
antibody	Donkey Anti-Goat IgG (H+L) Alexa Fluor 488	Thermo Fisher Scientific	Cat# A-11055; RRID:AB_2534120	IF (1:750)
antibody	Donkey Anti-Goat IgG (H+L) Alexa Fluor 555	Thermo Fisher Scientific	Cat# A21432; RRID:AB_2535853	IF (1:750)
antibody	Donkey Anti-Mouse IgG (H+L) Alexa Fluor 488	Thermo Fisher Scientific	Cat# A21202; RRID:AB_141607	IF (1:750)
other	Hoechst 33342	Thermo Fisher Scientific	Cat# H3570	IF (1:1000)

commercial assay or kit	Click-iT™ EdU Cell Proliferation Kit for Imaging, Alexa Fluor™ 647 dye	Thermo Fisher Scientific	Cat# C10340	
chemical compound, drug	Gelatin	VWR Chemicals	Cat# 24350.262 CAS Number: 9000-70-8	
chemical compound, drug	Thimerosal	Sigma-Aldrich	Cat# T8784-5g CAS Number: 54-64-8	
chemical compound, drug	TritonX-100	Sigma-Aldrich	Cat# X100-500ml CAS Number: 9002-93-1	
chemical compound, drug	SYBR Gold nucleic acid stain	Thermo Fisher Scientific	Thermo Fisher Scientific:S11494	
software, algorithm	Fiji	NIH	RRID:SCR_002285	Analysis
software, algorithm	GraphPad Prism	GraphPad	RRID:SCR_002798	Analysis
software, algorithm	Imaris	Oxford Instruments	RRID:SCR_007370	Analysis
software, algorithm	iMovie	Apple	http://www.apple.com/fr/imovie/	Analysis

Mouse lines

Full *Plxnb2* knockout mice were obtained by breeding *Plxnb2*^{tm1Matl} mouse (RRID:MGI:4881705), harboring a targeted secretory trap mutation between exon 16 and 17 in a CD1 background (Friedel et al., 2007). Conditional *Plxnb2* knockout mice

(Deng et al., 2007; Worzfeld et al., 2014), harboring loxP sites encompassing *Plxnb2* exons 19-23, were kept in a C57BL/6 genetic background, as were the *En1*^{Cre} (JAX #007916, *En1*$^{tm2(cre)Wrst}$/J) (Kimmel et al., 2000) and *Wnt1-Cre* (JAX #022501, B6.Cg-*E2f1*$^{tg(Wnt1-cre)2Sor}$/J (Danielian et al., 1998) mouse lines. For all experiments with conditional lines, *Plxnb2*$^{fl/fl}$ mice were crossed with heterozygous-*Cre*/homozygous-*floxed* animals to obtain *cre*-positive mutants and *Cre*-negative control animals in the same litter. Genotypes were determined by PCR from genomic DNA isolated from tail samples. All animal housing, handling and experimental procedures were carried out in accordance to institutional guidelines, approved by the Sorbonne University ethic committee (Charles Darwin). Noon on the day of a vaginal plug was considered E0.5 and date of birth as P0.

Rotarod.

The accelerating Rotarod (Columbus) consists of a horizontal rod, 3 cm in diameter, turning on its longitudinal axis. During the training phase, mice walked on the rod at a rotational speed varying from 4 to 40 rpm for one minute. The mice were then subjected to four trials in which the speed of rotation increased gradually from 4 rpm to 40 rpm over 5 min. Time spent on the rod was recorded and averaged for the 4 trials. The test was repeated three days in a row with the same procedure on the same animals, except that the training session was performed only on the first day. Animals of both sexes were used since no sex-dependent effect on locomotion was expected.

In situ hybridization

Sense and antisense RNA probes were designed to cover the floxed exons (19-23) of *Plxnb2* and *in vitro* transcribed from cDNA encoding the full-length mouse *Plxnb2* gene using the following primers (both including the T7 and T3 RNA polymerase binding sequences respectively: Forward 5'-TAATACGACTCACTATAGGGGCCTTTGAGCCATTGAGAAG -3' and Reverse 5'-AATTAACCCTCACTAAAGGGACGTCATTCGTCTGGTCCTC -3'. Probes were labeled with digoxigenin-11UTP (Roche Diagnostics) and *in situ* hybridizations were performed as previously described (Marillat et al., 2004). Slides were scanned with a Nanozoomer (Hamamatsu), images were handled in NDP.view2 (Hamamatsu) and corrected for brightness and contrast in Photoshop 21.0.2 (Adobe).

Immunohistochemistry

Pups were deeply anesthetized with ketamine (200 mg/kg) and xylazine (20 mg/kg) before transcardiac perfusion with 4% PFA in PBS. Brains were post-fixed for maximum 24 h, cryoprotected in 30% sucrose in PBS, embedded in 7.5% gelatin/10% sucrose in 0.12 M phosphate buffer, and frozen in isopentane at -50^{o}C. Cryosections of 20 µm or microtome sections of 50 µm were blocked with PBS-GT (0.2% gelatin, 0.25% Triton-X100 (sigma) in PBS) and incubated overnight at RT with the following primary antibodies against Plexin-B2, Pax6, Calbindin (CaBP), Ki67, Tag1, H3P, GFP, Myelin (MOG), Vglut1 as listed in the Key Resources Table. Species-specific Alexa-conjugated secondary antibodies (Jackson ImmunoResearch or Invitrogen) were diluted 1:750 and incubated 1-2 h at RT. Sections were counterstained with DAPI and embedded in Mowiol. Images were acquired with a DM6000 epifluorescence microscope (Leica) and a laser scanning confocal microscope (FV1000, Olympus) using Fluoview FV10-ASW software (Olympus).

Images were reconstructed using FIJI (NIH) or Imaris software (bitplane). Adobe Photoshop was used to adjust brightness, contrast, and levels.

Whole mount immunohistochemistry and 3D-light sheet microscopy

Mice were deeply anesthetized with ketamine (200 mg/kg) and xylazine (20 mg/kg) and transcardially perfused with 4% paraformaldehyde in PBS. Brains were briefly post-fixed, dehydrated in serial Methanol dilutions, bleached ON in Methanol + 5% H_2O_2 at 4 °C and rehydrated. Brains were permeabilized in PBS with 0.2% Gelatin, 0.5% Triton-X100 and 1mg/ml Saponin before incubation with primary antibodies against Pax6, FoxP2, and/or GFP in the same buffer (see Key Resources Table for antibody RRIDs and dilutions). Secondary antibodies conjugated to Alexa-fluorophores (Jackson ImmunoResearch) were incubated (1:750) together with TO-PRO-3 (1:150, Invitrogen). Tissue clearing was conducted using a methanol dehydration series, dichloromethane-mediated delipidation, and dibenzyl ether immersion, according to the iDISCO+ clearing protocol (Belle et al., 2014; Renier et al., 2014). 3D-imaging was performed with a fluorescence light sheet ultramicroscope (Ultramicroscope I, LaVision BioTec). 3D volumes were generated using Imaris x64 software (Bitplane). Videos of tiff image-sequences were converted in FIJI and edited in iMovie (Apple).

EdU labeling and quantification of proliferating cells

Two or 24 h prior to fixation, pups were injected intraperitoneally with 0.1 ml/10g bodyweight EdU solution of 5mg/ml (Invitrogen). Pups were deeply anesthetized with ketamine (200 mg/kg) and xylazine (20 mg/kg) before transcardiac perfusion with 4% PFA in PBS. Brains were post-fixed for 24h and cut in 20 µm thick sections with a

682 cryostat (Leica). Slides were incubated with primary antibody against H3P (see Key
683 Resources Table) followed by Alexa-conjugated secondary antibodies. EDU was
684 revealed using the EdU Click-it imaging kit (Invitrogen). High-resolution images of 3
685 mid-vermis sections per animal were acquired using an inverted Olympus FV1000
686 confocal laser-scanning microscope. Mosaic images were stitched using Imaris
687 stitcher (Bitplane). Imaris software (Bitplane) was used to segment straight-cut
688 stretches of lobe V/VI EGL to be used for semi-manual 'spots' cell count of EDU and
689 H3P positive nuclei in 3D. DAPI signal was used to determine total EGL volume of
690 analyzed area. Mann-Whitney U (MWU) non-parametric statistical analysis was
691 performed using Prism 7 software (Graphpad).
692
693 *In vivo cerebellum electroporation*
694 P7 or P11 mouse pups were ice-anesthetized and approximately 5 µl of a 1 µg/µl
695 DNA solution (pCX-EGFP or pCX-tdTomato) with 0.01% Fast Green was injected
696 subdurally at the level of the cerebellum using a glass needle (FHC PhymEP). CGN
697 precursors in the external granule layer were electroporated with five 50 ms pulses of
698 120 V with 950 ms interval using a tripolar electrode (dal Maschio et al., 2012). The
699 pup's head was held between a platinum-coated tweezer-electrode (positive pole,
700 Harvard Apparatus) and a third platinum electrode (custom-made, negative pole)
701 covered the cerebellar area. After electroporation pups were quickly revived, and
702 placed back in the litter. Two hours prior to transcardiac perfusion, pups were
703 injected intraperitoneally with 0.1 ml/10g bodyweight EdU (Invitrogen) solution of
704 5mg/ml in 0.6% NaCl. Pups were deeply anesthetized with ketamine (200 mg/kg)
705 and xylazine (20 mg/kg) before transcardiac perfusion with 4% PFA in PBS. Brains
706 were post-fixed for 24h. Coronal or sagittal 50 µm thick slices were made using a

freezing microtome. For tridimensional visualization of the morphology of electroporated CGNs, adult mice electroporated at P7 were transcardially perfused as described, and their brains were processed for whole-mount immunohistochemistry and tissue clearing as described above.

EGL explant cultures, time-lapse imaging and immunocytochemistry

P4-5 mouse pups were decapitated, 5 µl of 1 µg/µl pCX-GFP in 0.01% Fast Green was injected subdurally above the cerebellum and CGNs were electroporated as described above. Explants were made from both non-treated and electroporated cerebella (Kerjan et al., 2005). Cerebella were rapidly removed and placed in ice-cold L15 dissection medium (Gibco). 350 µm thick sagittal slices were made using a tissue chopper (MacIlwain) and 300-400 µm blocks of Fast Green containing EGL were dissected. EGL explants were seeded on 100 µg/ml PLL- and 40 µg/µl laminin-coated coverslips, or on similarly treated glass-bottom well plates (MatTec corp.). Explants were incubated in BME supplemented with 5% sucrose, 0.5% BSA, ITS, L-Glutamine and Pen/Strep, at 37^{o}C and 5% CO_2.

15 min interval time-lapsed acquisitions were taken after 24 h (days in vitro (DIV)1) in culture for at least 18 hours with an inverted Olympus FV1000 confocal laser-scanning microscope. Migration of GFP-positive cells was analyzed by semi-manual tracking using FIJI software. Total cell division events were counted using differential interference contrast and GFP signal. Mann-Whitney U non-parametric statistical analysis was performed using Prism 7 software (Graphpad).

For immunocytochemistry, culture medium was half replaced with medium containing 20 µM EDU (ThermoFischer, 10 µM end concentration) 2 h prior to fixation by 1:1 addition of 8% paraformaldehyde and 8% sucrose in PBS. Explants were incubated

overnight with primary antibodies against GFP βIII-tubulin, Pax6, H3P, Sema6a, GFAP, or Olig2 (antibody IDs and dilutions are listed in Key Resources Table). Secondary antibodies conjugated to Alexa fluorophores (1:750 Jackson ImmunoResearch or Invitrogen) were incubated for 1 h. EdU was revealed using the Click-it imaging kit (Invitrogen). Images were taken using an inverted Olympus FV1000 confocal laser-scanning microscope and Fluoview FV10-ASW software (Olympus). For quantification of cell counts and neurite length, images were acquired using a DM6000 epifluorescence microscope (Leica). DAPI and EdU-positive cells were counted using thresholded images and analyzed with FIJI software using particles tool and/or Sholl analysis tool. Mann-Whitney U (MWU) non-parametric statistical analysis was performed using Prism 7 software (Graphpad).

Data analysis and quantification

All statistical tests were performed by comparing averaged material from at least 4 different animals or 3 culture experiment repeats. All specific *N*s and statistical test result information are provided in the Figure legends. Non-parametric Mann-Whitney U tests or student T-test were performed in Prism 7 software. $p < 0.05$ was considered as statistically significant. All graphs (unless otherwise specified) show individual data points and average ± SEM. All source data used to render the graphs is included in excel files.

Cerebellar volume (Figure 3-figure supplement 1A) was measured by manual segmentation in Imaris of 5 to 6 P4 and P30 cerebella from both *Plxnb2*$^{fl/fl}$ control and *En1*^{Cre};*Plxnb2*$^{fl/fl}$ mutant animals (paraflocculus was not taken into account since it was sometimes removed during the dissection).

Cerebellar layer thickness (Figure 4A) was measured from coronal sections from 11 control and 13 mutant P9 brains. Thickness was measured in FIJI from 1-3 sections per brain, and averaged from 12 points per section in mid-cerebellar regions.

The amount of EdU-positive and/or H3P or Ki67 nuclei (Figure 4C, D, Figure 4-figure supplement 1A) was counted semi-automatically using the 'spots' function in Imaris from 5 control and 5 mutant animals for each condition. 3 sagittal sections (50 µm thick) per brain were imaged at high-magnification with a confocal microscope. The DAPI signal was segmented and used as value for EGL volume in which EdU cells were counted.

GFP-positive CGN cell body measurements, process length, and GFP/EdU or GFP/Pax6 co-staining were assessed with FIJI from 50 µm thick coronal sections imaged at high-magnification with a confocal. Specific N for each experiment can be found in figure legends. Cells with clear leading process(es) were considered uni- or bipolar CGN. Cells with a multipolar or round appearance were considered as CGN precursors. (Figure 5 and Figure 5-figure supplement 1)

DAPI/Calbindin signal in confocal z-stacks of 50 µm thick coronal sections (usually 2-3 sections per brain) was used to equally divide the EGL in two bins since in *Plxnb2* mutant, the EGL did not display clear inner/outer EGL boundary. All GFP^{+} CGNs were counted and assigned to multipolar or bipolar morphology. Percentages of multipolar cells or bipolar cells were calculated per bin (Figure 5-figure supplement 1C).

The relative distribution of parallel fibers in the molecular layer (Figure 6A) was measured in FIJI from 50 µm thick coronal sections and averaged from 3 different points per cerebellum from 7 $Plxnb2^{fl/fl}$ and 4 $En1^{Cre};Plxnb2^{fl/fl}$ cerebella. The

780 thickness of the part of the ML containing GFP^+ or $tdTom^+$ parallel fibers was
781 measured and normalized to the total thickness of the ML.
782 The distribution of Vglut1-positive puncta (Figure 6-figure supplement 1A) was
783 assessed by measuring the integrated density of the Vglut1 fluorescent signal in 5
784 distal and 5 proximal 10 x 10 µm squares along different Purkinje cells per animal,
785 from high-magnification confocal z-stacks from 20 µm thick sagittal sections. Data
786 was averaged from 4 animals for both genotypes. A ratio closer to 0 means that the
787 Vglut1 density in the distal square (dendrite tips) is much lower than the Vglut1
788 density in the proximal square (dendrite trunk). A ratio closer to 1 means that the
789 Vglut1 signal in the distal square is almost the same as the signal in the proximal
790 region.
791 The distribution of DAPI-positive nuclei in DIV1 EGL explants (Figure 7B) was
792 measured by Sholl analysis in FIJI. Cells were counted by the analyze particles tool
793 of FIJI. Multiple t-tests were used to calculate statistical difference between the
794 distance (continuous Sholl circles, 1 µm apart) neurons migrated outward control or
795 *Plxnb2* mutant explants.
796 The colocalization of DAPI/Pax6, GFP/Pax6, EdU/H3P or GFP/EdU (Figure 7, Figure
797 7-figure supplement 1 and 2, Figure 9) in DIV1 and/or DIV2 EGL explants was
798 assessed in FIJI from thresholded high-magnification confocal images. GFP-positive
799 CGNs were considered bipolar when two clear processes pointing in opposite
800 direction were present. Leading and trailing process length was measured in FIJI.
801 Specific Ns for each experiment can be found in the figure legends.
802 Time-lapse imaging was started around DIV1 and continued for at least 18 hours
803 (max 27 hours) with a 15 min interval. The tiff image sequence was opened in FIJI
804 and bipolar GFP-positive CGNs (Figure 8) were traced using semi-manual tracking

from the moment they had a clear bipolar morphology until the end of the imaging period or until the moment they left the field of view. Multipolar GFP-positive CGNs (Figure 10) were traced from the beginning of the imaging period, or the moment they left the explant, until they divided. These measurements were used to calculate and compare movement and total distance. Time between cytokinesis and the acquisition of a bipolar morphology was also measured in FIJI.

References

Addi, C., Presle, A., Frémont, S., Cuvelier, F., Rocancourt, M., Milin, F., Schmutz, S., Chamot-Rooke, J., Douché, T., Duchateau, M., et al. (2020) **The Flemmingsome reveals an ESCRT-to-membrane coupling via ALIX/syntenin/syndecan-4 required for completion of cytokinesis** *Nat Commun* **11**:1941. doi: 10.1038/s41467-020-15205-z

Ayoob, J.C. (2006) **Drosophila Plexin B is a Sema-2a receptor required for axon guidance** *Development* **133**:2125–35. doi: 10.1242/dev.02380

Azzarelli, R., Pacary, E., Garg, R., Garcez, P., van den Berg, D., Riou, P., Ridley, A.J., Friedel, R.H., Parsons, M., and Guillemot, F. (2014) **An antagonistic interaction between PlexinB2 and Rnd3 controls RhoA activity and cortical neuron migration** *Nat Commun* **5**:3405. doi: 10.1038/ncomms4405

Ballester-Lurbe, B., Poch, E., Mocholí, E., Guasch, R.M., Pérez-Roger, I., and Terrado, J. (2009) **RhoE is spatiotemporally regulated in the postnatal mouse CNS** *Neuroscience* **163**:586–593. doi: 10.1016/j.neuroscience.2009.06.062

Van Battum, E.Y., Brignani, S., and Pasterkamp, R.J. (2015) **Axon guidance proteins in neurological disease** *Lancet Neurol* **14**:532–546. doi: 10.1016/S1474-4422(14)70257-1

Van Battum, E.Y., Gunput, R.-A.F., Lemstra, S., Groen, E.J.N., Yu, K. Lou, Adolfs, Y., Zhou, Y., Hoogenraad, C.C., Yoshida, Y., Schachner, M., et al. (2014) **The intracellular redox protein MICAL-1 regulates the development of hippocampal mossy fibre connections** *Nat Commun* **5**:4317. doi: 10.1038/ncomms5317

Belle, M., Godefroy, D., Dominici, C., Heitz-Marchaland, C., Zelina, P., Hellal, F., Bradke, F., and Chédotal, A. (2014) **A Simple Method for 3D Analysis of**

Immunolabeled Axonal Tracts in a Transparent Nervous System *Cell Rep* **9**:1191–201. doi: 10.1016/j.celrep.2014.10.037

Binamé, F., Pham - Van, L.D., Spenlé, C., Jolivel, V., Birmpili, D., Meyer, L.A., Jacob, L., Meyer, L., Mensah - Nyagan, A.G., Po, C., et al. (2019) **Disruption of Sema3A/Plexin - A1 inhibitory signalling in oligodendrocytes as a therapeutic strategy to promote remyelination** *EMBO Mol Med* **11**:e10378. doi: 10.15252/emmm.201910378

Bulloj, A., Maminishkis, A., Mizui, M., and Finnemann, S.C. (2018) **Semaphorin4D-PlexinB1 Signaling Attenuates Photoreceptor Outer Segment Phagocytosis by Reducing Rac1 Activity of RPE Cells** *Mol Neurobiol* **55**:4320–4332. doi: 10.1007/s12035-017-0649-5

Chédotal, A. (2010) **Should I stay or should I go? Becoming a granule cell** *Trends Neurosci.* **33**:163–172. doi: 10.1016/j.tins.2010.01.004

dal Maschio, M., Ghezzi, D., Bony, G., Alabastri, A., Deidda, G., Brondi, M., Sato, S.S., Zaccaria, R.P., Di Fabrizio, E., Ratto, G.M., et al. (2012) **High-performance and site-directed in utero electroporation by a triple-electrode probe** *Nat Commun* **3**:960. doi: 10.1038/ncomms1961

Danielian, P.S., Muccino, D., Rowitch, D.H., Michael, S.K., and McMahon, A.P. (1998) **Modification of gene activity in mouse embryos in utero by a tamoxifen-inducible form of Cre recombinase** *Curr Biol* **8**:1323-6. doi: 10.1016/s0960-9822(07)00562-3

Deng, S., Hirschberg, A., Worzfeld, T., Penachioni, J.Y., Korostylev, A., Swiercz, J.M., Vodrazka, P., Mauti, O., Stoeckli, E.T., Tamagnone, L., et al. (2007) **Plexin-B2, but not Plexin-B1, critically modulates neuronal migration and patterning of the developing nervous system in vivo** *J Neurosci* **27**:6333-47. doi: 10.1523/JNEUROSCI.5381-06.2007

Espinosa, J.S., and Luo, L. (2008) **Timing neurogenesis and differentiation: insights from quantitative clonal analyses of cerebellar granule cells** *J Neurosci* **28**:2301-12. doi: 10.1523/JNEUROSCI.5157-07.2008

Frémont, S., Romet-Lemonne, G., Houdusse, A., and Echard, A. (2017) **Emerging roles of MICAL family proteins - from actin oxidation to membrane trafficking during cytokinesis** *J Cell Sci* **130**:1509–1517. doi: 10.1242/jcs.202028

882

883 Friedel, R.H., Kerjan, G., Rayburn, H., Schüller, U., Sotelo, C., Tessier-Lavigne, M.,
884 and Chédotal, A. (2007) **Plexin-B2 controls the development of cerebellar**
885 **granule cells** *J. Neurosci* **27**:3921–3932. doi: 10.1523/JNEUROSCI.4710-06.2007
886

887 Giacobini, P., Messina, A., Morello, F., Ferraris, N., Corso, S., Penachioni, J.,
888 Giordano, S., Tamagnone, L., and Fasolo, A. (2008) **Semaphorin 4D regulates**
889 **gonadotropin hormone–releasing hormone-1 neuronal migration through**
890 **PlexinB1–Met complex** *J Cell Biol* **183**:555–66. doi: 10.1083/jcb.200806160
891

892 Giordano, S., Corso, S., Conrotto, P., Artigiani, S., Gilestro, G., Barberis, D.,
893 Tamagnone, L., and Comoglio, P.M. (2002) **The semaphorin 4D receptor controls**
894 **invasive growth by coupling with Met** *Nat Cell Biol* **4**:720–24. doi: 10.1038/ncb843
895

896 Govek, E.E., Wu, Z., Acehan, D., Molina, H., Rivera, K., Zhu, X., Fang, Y., Tessier-
897 Lavigne, M., and Hatten, M.E. (2018) **Cdc42 Regulates Neuronal Polarity during**
898 **Cerebellar Axon Formation and Glial-Guided Migration** *iScience* **1**:35–48. doi:
899 10.1016/j.isci.2018.01.004
900

901 Gurrapu, S., Pupo, E., Franzolin, G., Lanzetti, L., and Tamagnone, L. (2018)
902 **Sema4C/PlexinB2 signaling controls breast cancer cell growth, hormonal**
903 **dependence and tumorigenic potential** *Cell Death Differ* **25**:1259–1275. doi:
904 10.1038/s41418-018-0097-4
905

906 Harding, B.N., Moccia, A., Drunat, S., Soukarieh, O., Tubeuf, H., Chitty, L.S.,
907 Verloes, A., Gressens, P., El Ghouzzi, V., Joriot, S., et al. (2016) **Mutations in**
908 **Citron Kinase Cause Recessive Microlissencephaly with Multinucleated**
909 **Neurons** *Am J Hum Genet* **99**:511–20. doi: 10.1016/j.ajhg.2016.07.003
910

911 Hirschberg, a, Deng, S., Korostylev, A., Paldy, E., Costa, M.R., Worzfeld, T.,
912 Vodrazka, P., Wizenmann, A., Götz, M., Offermanns, S., et al. (2010) **Gene deletion**
913 **mutants reveal a role for semaphorin receptors of the plexin-B family in**
914 **mechanisms underlying corticogenesis** *Mol Cell Biol* **30**, 764–780. doi:
915 10.1128/MCB.01458-09
916

917 Hung, R.-J., Yazdani, U., Yoon, J., Wu, H., Yang, T., Gupta, N., Huang, Z., van
918 Berkel, W.J.H., and Terman, J.R. (2010) **Mical links semaphorins to F-actin**
919 **disassembly** *Nature* **463**:823–7. doi: 10.1038/nature08724
920

921 Jossin, Y., and Cooper, J.A. (2011) **Reelin, Rap1 and N-cadherin orient the**
922 **migration of multipolar neurons in the developing neocortex** *Nat Neurosci* **14**:
923 697–703. doi: 10.1038/nn.2816
924
925 Kawaji, K., Umeshima, H., Eiraku, M., Hirano, T., and Kengaku, M. (2004) **Dual**
926 **phases of migration of cerebellar granule cells guided by axonal and dendritic**
927 **leading processes** *Mol Cell Neurosci* **25**:228–240. doi: 10.1016/j.mcn.2003.10.006
928
929 Kerjan, G., Dolan, J., Haumaitre, C., Schneider-Maunoury, S., Fujisawa, H., Mitchell,
930 K.J., and Chédotal, A. (2005) **The transmembrane semaphorin Sema6A controls**
931 **cerebellar granule cell migration** *Nat Neurosci* **8**:1516–24. doi: 10.1038/nn1555
932
933 Kimmel, R.A., Turnbull, D.H., Blanquet, V., Wurst, W., Loomis, C. a., and Joyner,
934 A.L. (2000) **Two lineage boundaries coordinate vertebrate apical ectodermal**
935 **ridge formation** *Genes Dev* **14**:1377–89. PMC316660
936 Komuro, H., Yacubova, E., and Rakic, P. (2001) **Mode and tempo of tangential cell**
937 **migration in the cerebellar external granular layer** *J Neurosci* **21**:527–40. doi:
938 10.1523/JNEUROSCI.21-02-00527.2001
939
940 Yacubova , E. and Komuro, H. (2002) **Intrinsic program for migration of**
941 **cerebellar granue cells in vitro** *J Neurosci* **22**:5966-5981. doi:
942 10.1523/JNEUROSCI.22-14-05966.2002
943
944 Konishi, Y., Stegmüller, J., Matsuda, T., Bonni, S., and Bonni, A. (2004) **Cdh1-APC**
945 **controls axonal growth and patterning in the mammalian brain** *Science* **303**:
946 1026–30. doi: 10.1126/science.1093712
947
948 Kuzirian, M.S., Moore, a. R., Staudenmaier, E.K., Friedel, R.H., and Paradis, S.
949 (2013) **The Class 4 Semaphorin Sema4D Promotes the Rapid Assembly of**
950 **GABAergic Synapses in Rodent Hippocampus** *J Neurosci* **33**:8961–73. doi:
951 10.1523/JNEUROSCI.0989-13.2013
952
953 Legue, E., Riedel, E., and Joyner, A.L. (2015) **Clonal analysis reveals granule cell**
954 **behaviors and compartmentalization that determine the folded morphology of**
955 **the cerebellum** *Development* **142**:1661–71. doi: 10.1242/dev.120287
956
957 Leto, K., Arancillo, M., Becker, E.B.E., Buffo, A., Chiang, C., Ding, B., Dobyns, W.B.,
958 Dusart, I., Haldipur, P., Hatten, M.E., et al. (2016) **Consensus Paper: Cerebellar**
959 **Development** *Cerebellum* **15**:789–828. doi: 10.1007/s12311-015-0724-2
960

Lewis, A.E., H Vasudevan, H.N., O'Neill, A.K., Soriano P. and Bush, J.O. (2013) **The widely used Wnt1-Cre transgene causes developmental phenotypes by ectopic activation of Wnt signaling**. *Dev Biol* 379:229-34. doi: 10.1016/j.ydbio.2013.04.026.

Li, H., Bielas, S.L., Zaki, M.S., Ismail, S., Farfara, D., Um, K., Rosti, R.O., Scott, E.C., Tu, S., Chi, N.C., et al. (2016) **Biallelic Mutations in Citron Kinase Link Mitotic Cytokinesis to Human Primary Microcephaly** *Am J Hum Genet* **99**, 501–510. doi: 10.1016/j.ajhg.2016.07.004

Maier, V., Jolicoeur, C., Rayburn, H., Takegahara, N., Kumanogoh, A., Kikutani, H., Tessier-Lavigne, M., Wurst, W., and Friedel, R.H. (2011) **Semaphorin 4C and 4G are ligands of Plexin-B2 required in cerebellar development** *Mol Cell Neurosci* **46**:419–31. doi: 10.1016/j.mcn.2010.11.005

Marillat, V., Sabatier, C., Failli, V., Matsunaga, E., Sotelo, C., Tessier-Lavigne, M., and Chédotal, A. (2004) **The Slit Receptor Rig-1/Robo3 Controls Midline Crossing by Hindbrain Precerebellar Neurons and Axons** *Neuron* **43**:69–79. doi: 10.1016/j.neuron.2004.06.018

Martz, M.K., Grabocka, E., Beeharry, N., Yen, T.J., and Wedegaertner, P.B. (2013) **Leukemia-associated RhoGEF (LARG) is a novel RhoGEF in cytokinesis and required for the proper completion of abscission** *Mol Biol Cell* **24**:2785–94. doi: 10.1091/mbc.E12-07-0533

McColl, B., Garg, R., Riou, P., Riento, K., and Ridley, A.J. (2016) **Rnd3-induced cell rounding requires interaction with Plexin-B2** *J Cell Sci* **129**:4046-4056. doi: 10.1242/jcs.192211

Miale, I., and Sidman, R. (1961) **An Autoradiographic Analysis of Histogenesis in the Mouse Cerebellum** *Exp Neurol* **4**:277–96. doi: 10.1016/0014-4886(61)90055-3

Mocholí, E., Ballester-Lurbe, B., Arqué, G., Poch, E., Peris, B., Guerri, C., Dierssen, M., Guasch, R.M., Terrado, J., and Pérez-Roger, I. (2011) **Rhoe deficiency produces postnatal lethality, profound motor deficits and neurodevelopmental delay in mice** *PLoS One* **6**:e19236. doi: 10.1371/journal.pone.0019236

Molofsky, A. V, Kelley, K.W., Tsai, H.-H., Redmond, S. a, Chang, S.M., Madireddy, L., Chan, J.R., Baranzini, S.E., Ullian, E.M., and Rowitch, D.H. (2014) **Astrocyte-encoded positional cues maintain sensorimotor circuit integrity** *Nature* 509: 189–94. doi: 10.1038/nature13161

Nakamura, T., Ueyama, T., Ninoyu, Y., Sakaguchi, H., Choijookhuu, N., Hishikawa, Y., Kiyonari, H., Kohta, M., Sakahara, M., de Curtis, I., et al. (2017) **Novel role of Rac-Mid1 signaling in medial cerebellar development** *Development* **144**:1863–1875. doi: 10.1242/dev.147900

Nichols, D.H., and Bruce, L.L. (2006) **Migratory routes and fates of cells transcribing the Wnt-1 gene in the murine hindbrain** *Dev Dyn* **235**:285–300. doi: 10.1002/dvdy.20611

Obara, Y., Horgan, A.M., and Stork, P.J.S. (2007) **The requirement of Ras and Rap1 for the activation of ERKs by cAMP, PACAP, and KCl in cerebellar granule cells** *J Neurochem* **101**:470–82. doi: 10.1111/j.1471-4159.2006.04390.x

Oinuma, I. (2004) **The Semaphorin 4D Receptor Plexin-B1 Is a GTPase Activating Protein for R-Ras** *Science* **305**:862–5. doi: 10.1126/science.1097545

Orr, B.O., Fetter, R.D., and Davis, G.W. (2017) **Retrograde semaphorin–plexin signalling drives homeostatic synaptic plasticity** *Nature* **550**:109-113. doi: 10.1038/nature24017

Otero, J.J., Kalaszczynska, I., Michowski, W., Wong, M., Gygli, P.E., Gokozan, H.N., Griveau, A., Odajima, J., Czeisler, C., Catacutan, F.P., et al. (2013) **Cerebellar cortical lamination and foliation require cyclin A2** *Dev Biol* **385**:328-39. doi: 10.1016/j.ydbio.2013.10.019

Paldy, E., Simonetti, M., Worzfeld, T., Bali, K.K., Vicuña, L., Offermanns, S., and Kuner, R. (2017) **Semaphorin 4C Plexin-B2 signaling in peripheral sensory neurons is pronociceptive in a model of inflammatory pain** *Nat Commun* **8**:176. doi: 10.1038/s41467-017-00341-w

Park, H., Kim, T., Kim, J., Yamamoto, Y., and Tanaka-Yamamoto, K. (2019) **Inputs from Sequentially Developed Parallel Fibers Are Required for Cerebellar Organization** *Cell Rep* **28**:2939-2954.e5. doi: 10.1016/j.celrep.2019.08.010

Pascoe, H.G., Gutowski, S., Chen, H., Brautigam, C.A., Chen, Z., Sternweis, P.C., and Zhang, X. (2015) **Secondary PDZ domain-binding site on class B plexins enhances the affinity for PDZ–RhoGEF** *Proc Natl Acad Sci* **112**:14852–7. doi: 10.1073/pnas.1508931112

Pasterkamp, R.J. (2012) **Getting neural circuits into shape with semaphorins** *Nat Rev Neurosci* **13**:605–18. doi: 10.1038/nrn3302

Pecho-Vrieseling, E., Sigrist, M., Yoshida, Y., Jessell, T.M., and Arber, S. (2009) **Specificity of sensory–motor connections encoded by Sema3e–Plxnd1 recognition** *Nature* **459**:842–6. doi: 10.1038/nature08000

Perrot, V., Vazquez-Prado, J., and Gutkind, J.S. (2002) **Plexin B regulates Rho through the guanine nucleotide exchange factors leukemia-associated Rho GEF (LARG) and PDZ-RhoGEF** *J Biol Chem* **277**:43115–20. doi: 10.1074/jbc.M206005200

Ramón y Cajal, S. (1909). Histologie du système nerveux de l'homme & des vertébrés.

Renaud, J., and Chédotal, A. (2014) **Time-lapse analysis of tangential migration in Sema6A and PlexinA2 knockouts** *Mol Cell Neurosci* **63**:49–59. doi: 10.1016/j.mcn.2014.09.005

Renier, N., Wu, Z., Simon, D.J., Yang, J., Ariel, P., and Tessier-Lavigne, M. (2014) **iDISCO: A Simple, Rapid Method to Immunolabel Large Tissue Samples for Volume Imaging** *Cell* **159**:896–910. doi: 10.1016/j.cell.2014.10.010

Renier, N., Adams, E.L., Kirst, C., Wu, Z., Azevedo, R., Kohl, J., Autry, A.E., Kadiri, L., Umadevi Venkataraju, K., Zhou, Y., et al. (2016) **Mapping of Brain Activity by Automated Volume Analysis of Immediate Early Genes** *Cell* **165**:1789–1802. doi: 10.1016/j.cell.2016.05.007

Rohm, B., Rahim, B., Kleiber, B., Hovatta, I., and Püschel, A.W. (2000) **The semaphorin 3A receptor may directly regulate the activity of small GTPases** *FEBS Lett* **486**:68–72. doi: 10.1016/s0014-5793(00)02240-7

Roney, K.E., O'Connor, B.P., Wen, H., Holl, E.K., Guthrie, E.H., Davis, B.K., Jones, S.W., Jha, S., Sharek, L., Garcia-Mata, R., et al. (2011) **Plexin-B2 negatively regulates macrophage motility, Rac, and Cdc42 activation** *PLoS One* **6**:e24795. doi: 10.1371/journal.pone.0024795

Saha, B., Ypsilanti, A.R., Boutin, C., Cremer, H., and Chédotal, A. (2012) **Plexin-B2 Regulates the Proliferation and Migration of Neuroblasts in the Postnatal and**

Adult Subventricular Zone *J Neurosci* **32**:16892–905. doi: 10.1523/JNEUROSCI.0344-12.2012

Seiradake, E., Jones, E.Y., and Klein, R. (2016) **Structural Perspectives on Axon Guidance** *Annu Rev Cell Dev Biol* **32**:577–608. doi: 10.1146/annurev-cellbio-111315-125008

Sekine, Y., Algarate, P.T., Cafferty, W.B.J., and Strittmatter, S.M. (2019) **Plexina2 and CRMP2 Signaling Complex Is Activated by Nogo-A-Liganded Ngr1 to Restrict Corticospinal Axon Sprouting after Trauma** J *Neurosci* **39**:3204–3216. doi: 10.1523/JNEUROSCI.2996-18 .2019

Shah, B., Lutter, D., Tsytsyura, Y., Glyvuk, N., Sakakibara, A., Klingauf, J., and Püschel, A.W. (2017) **Rap1 GTPases Are Master Regulators of Neural Cell Polarity in the Developing Neocortex** *Cereb Cortex* **27**:1253–1269. doi: 10.1093/cercor/bhv341

Simonetti, M., Paldy, E., Njoo, C., Bali, K.K., Worzfeld, T., Pitzer, C., Kuner, T., Offermanns, S., Mauceri, D., and Kuner, R. (2019) **The impact of Semaphorin 4C/Plexin-B2 signaling on fear memory via remodeling of neuronal and synaptic morphology** *Mol Psychiatry* **26**:1376–1398. doi: 10.1038/s41380-019-0491-4

Singh, S., Howell, D., Trivedi, N., Kessler, K., Ong, T., Rosmaninho, P., Raposo, A.A.S.F., Robinson, G., Roussel, M.F., Castro, D.S., et al. (2016) **Zeb1 controls neuron differentiation and germinal zone exit by a mesenchymal-epithelial-like transition** *Elife* **5**:e12717. doi: 10.7554/eLife.12717

Sotelo, C. (2011) **Camillo Golgi and Santiago Ramon y Cajal: The anatomical organization of the cortex of the cerebellum. Can the neuron doctrine still support our actual knowledge on the cerebellar structural arrangement?** *Brain Res Rev* **66**:16–34. doi: 10.1016/j.brainresrev.2010.05.004

Subramanian, V., Crabtree, B., and Acharya, K.R. (2008) **Human angiogenin is a neuroprotective factor and amyotrophic lateral sclerosis associated angiogenin variants affect neurite extension/ pathfinding and survival of motor neurons** *Hum Mol Genet* **17**:130–49. doi: 10.1093/hmg/ddm290

Sudarov, A., and Joyner, A.L. (2007) **Cerebellum morphogenesis: the foliation pattern is orchestrated by multi-cellular anchoring centers** *Neural Dev* 2:26. doi: 10.1186/1749-8104-2-26

Swiercz, J.M., Kuner, R., Behrens, J., and Offermanns, S. (2002) **Plexin-B1 Directly Interacts with PDZ-RhoGEF/LARG to Regulate RhoA and Growth Cone Morphology** *Neuron* **35**:51–63. doi: 10.1016/s0896-6273(02)00750-x

Swiercz, J.M., Kuner, R., and Offermanns, S. (2004) **Plexin-B1/RhoGEF–mediated RhoA activation involves the receptor tyrosine kinase ErbB-2** *J Cell Biol* **165**: 869–80. doi: 10.1083/jcb.200312094

Tamagnone, L., Artigiani, S., Chen, H., He, Z., Ming, G., Song, H., Chedotal, A., Winberg, M.L., Goodman, C.S., Poo, M., et al. (1999) **Plexins Are a Large Family of Receptors for Transmembrane, Secreted, and GPI-Anchored Semaphorins in Vertebrates** *Cell* **99**:71–80. doi: 10.1016/s0092-8674(00)80063-x

Terman, J.R., Mao, T., Pasterkamp, R.J., Yu, H.-H., and Kolodkin, A.L. (2002) **MICALs, a family of conserved flavoprotein oxidoreductases, function in plexin-mediated axonal repulsion** *Cell* **109**:887–900. doi: 10.1016/s0092-8674(02)00794-8

Tomassy, G.S., Berger, D.R., Chen, H.-H.H.-H., Kasthuri, N., Hayworth, K.J., Vercelli, A., Seung, H.S., Lichtman, J.W., and Arlotta, P. (2014) **Distinct profiles of myelin distribution along single axons of pyramidal neurons in the neocortex** *Science* ***344***:319–24. doi: 10.1126/science.1249766

Tong, Y., Chugha, P., Hota, P.K., Alviani, R.S., Li, M., Tempel, W., Shen, L., Park, H.-W., and Buck, M. (2007) **Binding of Rac1, Rnd1, and RhoD to a novel Rho GTPase interaction motif destabilizes dimerization of the plexin-B1 effector domain** J *Biol Chem* **282**:37215–24. doi: 10.1074/jbc.M703800200

Turner, L.J., Nicholls, S., and Hall, A. (2004) **The activity of the plexin-A1 receptor is regulated by Rac** *J Biol Chem* **279**:33199–205.

Umeshima, H., Hirano, T., and Kengaku, M. (2007) **Microtubule-based nuclear movement occurs independently of centrosome positioning in migrating neurons** *Proc Natl Acad Sci U S A* **104**:16182–7. doi: 10.1073/pnas.0708047104

Vikis, H.G., Li, W., He, Z., and Guan, K.L. (2000) **The semaphorin receptor plexin-B1 specifically interacts with active Rac in a ligand-dependent manner** *Proc Natl Acad Sci U S A* **97**:12457–62. doi: 10.1073/pnas.220421797

Voogd, J. (2003) Cerebellum and Precerebellar Nuclei (Elsevier Inc.).

Wang, Y., He, H., Srivastava, N., Vikarunnessa, S., Chen, Y., Jiang, J., Cowan, C.W., and Zhang, X. (2012) **Plexins are GTPase-activating proteins for Rap and are activated by induced dimerization** Sci Signal **5**:ra6. doi: 10.1126/scisignal.2002636

Wang, Y., Pascoe, H.G., Brautigam, C.A., He, H., and Zhang, X. (2013) **Structural basis for activation and non-canonical catalysis of the Rap GTPase activating protein domain of plexin** *Elife* **2**:e01279. doi: 10.7554/eLife.01279

Worzfeld, T., and Offermanns, S. (2014) **Semaphorins and plexins as therapeutic targets** *Nat Rev Drug Discov* **13**:603–21. doi: 10.1038/nrd4337

Worzfeld, T., Puschel, A.W., Offermanns, S., and Kuner, R. (2004) **Plexin-B family members demonstrate non-redundant expression patterns in the developing mouse nervous system: an anatomical basis for morphogenetic effects of Sema4D during development** *Eur J Neurosci* **19**:2622–32. doi: 10.1111/j.0953-816X.2004.03401.x

Worzfeld, T., Rauch, P., Karram, K., Trotter, J., Kuner, R., and Offermanns, S. (2009) **Mice lacking Plexin-B3 display normal CNS morphology and behaviour** *Mol Cell Neurosci* **42**:372–81. doi: 10.1016/j.mcn.2009.08.008

Worzfeld, T., Swiercz, J.M., Sentürk, A., Genz, B., Korostylev, A., Deng, S., Xia, J., Hoshino, M., Epstein, J.A., Chan, A.M., et al. (2014) **Genetic dissection of plexin signaling in vivo** *Proc Natl Acad Sci U S A* **111**:2194–9. doi: 10.1073/pnas.1308418111

Wylie, T., Garg, R., Ridley, A.J., and Conte, M.R. (2017) **Analysis of the interaction of Plexin-B1 and Plexin-B2 with Rnd family proteins** *PLoS One* **12**:e0185899. doi: 10.1371/journal.pone.0185899

Xia, J., Swiercz, J.M., Bañón-Rodríguez, I., Matković, I., Federico, G., Sun, T., Franz, T., Brakebusch, C.H., Kumanogoh, A., Friedel, R.H., et al. (2015) **Semaphorin-**

Plexin Signaling Controls Mitotic Spindle Orientation during Epithelial Morphogenesis and Repair *Dev Cell* **33**:299–313. doi: 10.1016/j.devcel.2015.02.001

Yoshida, Y. (2012) **Semaphorin signaling in vertebrate neural circuit assembly**. *Front Mol Neurosci* **5**:71. doi: 10.3389/fnmol.2012.00071

Yu, W., Goncalves, K.A., Li, S., Kishikawa, H., Sun, G., Yang, H., Vanli, N., Wu, Y., Jiang, Y., Hu, M.G., et al. (2017) **Plexin-B2 Mediates Physiologic and Pathologic Functions of Angiogenin** *Cell* **171**:849-864.e25. doi: 10.1016/j.cell.2017.10.005

Yukawa, K., Tanaka, T., Yoshida, K., Takeuchi, N., Ito, T., Takamatsu, H., Kikutani, H., and Kumanogoh, A. (2010) **Sema4A induces cell morphological changes through B-type plexin-mediated signaling** *Int J Mol Med* **25**:225–30.

Zanata, S.M., Hovatta, I., Rohm, B., and Püschel, A.W. (2002) **Antagonistic effects of Rnd1 and RhoD GTPases regulate receptor activity in Semaphorin 3A-induced cytoskeletal collapse** *J Neurosci* **22**:471–7. doi: 10.1523/JNEUROSCI.22-02-00471.2002

Zervas, M., Millet, S., Ahn, S., and Joyner, A.L. (2004) **Cell behaviors and genetic lineages of the mesencephalon and rhombomere 1** *Neuron* **43**:345–57. doi: 10.1016/j.neuron.2004.07.010

Zhang, J., and Zhang, Y.P. (2003) **Pseudogenization of the tumor-growth promoter angiogenin in a leaf-eating monkey** *Gene* **308**:95–101. doi: 10.1016/s0378-1119(03)00470-0

Zhang, L., Polyansky, A., and Buck, M. (2015) **Modeling Transmembrane Domain Dimers/Trimers of Plexin Receptors: Implications for Mechanisms of Signal Transmission across the Membrane** *PLoS One* **10**:e0121513. doi: 10.1371/journal.pone.0121513

Zhao, X.F., Kohen, R., Parent, R., Duan, Y., Fisher, G.L., Korn, M.J., Ji, L., Wan, G., Jin, J., Püschel, A.W., et al. (2018) **PlexinA2 Forward Signaling through Rap1 GTPases Regulates Dentate Gyrus Development and Schizophrenia-like Behaviors** *Cell Rep* **22**:456–470. doi: 10.1016/j.celrep.2017.12.044

Zhou, X., Wahane, S., Friedl, M., Kluge, M., Friedel, C.C., Avrampou, K., Zachariou, V., Guo, L., Zhang, B., He, X., et al. (2020) **Microglia and macrophages promote**

corralling, wound compaction and recovery after spinal cord injury via Plexin-B2 *Nat Neurosci* **23**:337–350. doi: 10.1038/s41593-020-0597-7

Zong, H., Espinosa, J.S., Su, H.H., Muzumdar, M.D., and Luo, L. (2005) **Mosaic analysis with double markers in mice** *Cell* **121**:479–92. doi: 10.1016/j.cell.2005.02.012

Figure Legends

Figure 1 – Plexin-B2 expression and generation of cerebellum-specific *Plxnb2* conditional knockout models

(A, B, C), Plexin-B2 protein distribution in the cerebellar cortex during different stages of postnatal development. (**A**) Plexin-B2 immunostaining on cryostat sections immunolabeled with the Purkinje cell (PC) marker Calbindin (CaBP) and counterstained with DAPI shows that Plexin-B2 is expressed in the external granule layer (EGL). (**B**) Plexin-B2 immunoreactivity coincides with EdU (injected 2 h prior to fixation to visualize proliferating cells) showing that this receptor is restricted to proliferating cerebellar granule neurons (CGNs) in the outer external granular cell layer (oEGL). It is downregulated in Tag1+ postmitotic CGNs in the inner EGL (iEGL). (**C**) High-magnification images show Plexin-B2 expression in the oEGL (stained with EdU), which regresses between P6 and P15. (**D**) Sagittal section of P27 cerebellum $Plxnb2^{-/-}$ (full knockout) cerebellum stained with DAPI. The structure and layers of the cerebellar cortex are disorganized. Clear gaps in the internal granule layer structure can be observed (yellow asterisks), as well as patches of cells that accumulated at the cerebellar surface (arrowhead). (**E**) Schematic representation of the genomic *Plxnb2* sequence of the conditional *Plxnb2* mutant described in (Worzfeld et al., 2014). The *loxP* sites flanking exons 19-23 are depicted with red triangles. $Plxnb2^{fl/fl}$ conditional mutant mice were crossed with $En1^{Cre}$ or *Wnt1-Cre*

mice. (**F**) *In situ* hybridization, on cerebellar sections at P4 and P7, with a probe recognizing the floxed exons of the *Plxnb2* gene. Sections incubated with *sense* probe are devoid of signal. In *cre*-negative *Plxnb2*$^{fl/fl}$ control mice, *Plxnb2* mRNA is only detected in the oEGL. In both *En1*^{Cre}*;Plxnb2*$^{fl/fl}$ and *Wnt1-Cre;Plxnb2*$^{fl/fl}$ littermates, *Plxnb2* mRNA is deleted from the oEGL. (**G**) Plexin-B2 immunostaining on sagittal cerebellar sections of *En1*^{Cre}*;Plxnb2*$^{fl/fl}$ (P5) and *Wnt1-Cre;Plxnb2*$^{fl/fl}$ (P7) animals shows the absence of Plexin-B2 protein in the EGL. Sections were also labeled with anti-CaBP antibodies and DAPI. Impaired cerebellar foliation (white arrowheads) and Purkinje cell islands (yellow asterisks) are observed in both conditional knockouts. (**H**) P20 sagittal cerebellar sections immunostained for CaBP and counterstained with DAPI. Both *En1*^{Cre}*;Plxnb2*$^{fl/fl}$ and *Wnt1-Cre;Plxnb2*$^{fl/fl}$ conditional knockouts phenocopy the cerebellar defects found in *Plxnb2*$^{-/-}$ mutants. White arrowheads mark altered foliation, whereas yellow arrowheads in the magnified panels show surface accumulations of CGNs. Yellow asterisks indicate Purkinje cell islets. *En1*^{Cre}*;Plxnb2*$^{fl/fl}$ mice display the *Plxnb2* phenotype to a greater extent.

Scale bars: A: 1 mm. B, C: 10 µm. D: low magnification 1 mm, high magnification 500 µm. F: low magnification overview panels: 500 µm, high magnification panels: 100 µm. G: overview panels: 500 µm, high magnification EGL panels: 10 µm. H: low magnification panels 300 µm, high magnification panels 100 µm.

Figure 2 – Developmental time course of cerebellar *Plxnb2* phenotype.

The time course of cerebellar foliation and lamination during early postnatal cerebellar development is delayed in *Plxnb2* conditional knockout. (**A**) Pax6 immunostaining labels both pre- and postmitotic CGNs in the developing cerebellum,

and Calbindin (CaBP) labels Purkinje cells. In controls, many cerebellar fissures have formed at P0, and deepen further at P2 and P4, whereas the cerebellum of *En1^{Cre};Plxnb2$^{fl/fl}$* mutant displays a very shallow primary fissure (prf) at P0 and aberrant fissure development over time. Furthermore, ectopic Purkinje cell islets (arrowheads) are observed in *Plxnb2* mutant internal granule layer. (**B**) 3D- Light-sheet microscope imaging of TO-PRO-3 stained and iDISCO+ cleared (see methods) P4 cerebellum illustrating the foliation delay in *Plxnb2* conditional KO. Right panels are optical sections (coronal or horizontal) through 3D-reconstructed images. *Plxnb2* mutants develop aberrant shallow fissures and additional folia in different orientations Abbreviations: pfr: primary fissure, ppf: prepyramidal fissure, sf: secondary fissure, pcn: precentral fissure, pcuf: preculminate fissure, pfl: posterolateral fissure.

Scale bars: overview panels A, B: 500 µm, magnifications in A: 100 µm.

Figure 3 – Ruffled IGL and ectopic CGN patches in cerebellum-specific *Plxnb2* mutant.

(**A- D**) Whole-mount TO-PRO-3 staining of P14 and P30 cerebella from *Plxnb2$^{fl/fl}$* and *En1^{Cre};Plxnb2$^{fl/fl}$* littermates cleared with iDISCO+. In 3D, TO-PRO-3 staining mainly reveals the structure of the cell-dense IGL. *Plxnb2$^{fl/fl}$* control cerebella **(A)** display a very smooth IGL. A thin layer of EGL remains at P14 but not at P30 **(C)**. In P14 *En1^{Cre};Plxnb2$^{fl/fl}$* mice, the regressing EGL contains ectopic clusters of CGNs (**B**) that remain at P30 **(D)**. In addition, *Plxnb2* mutant IGL (**B, D**) shows many invaginations in different directions, independent of normal fissure orientation. Although some fissures are clearly formed and visible (prf, ppf), many others are absent. The paraflocculus (pf), present in P30 control, was lost during dissection in the *Plxnb2* mutant. Greek numbers indicate cerebellar lobes. Scale bars: 700 µm for the 3D

images, 500 µm for the coronal and horizontal sections. Pfr: primary fissure, psf: posterior superior fissure, ppf: prepyramidal fissure, sf: secondary fissure. Figure 3-figure supplement 1A shows quantification of 3D cerebellar volume (Figure 3-figure supplement 1-source data 1)

Figure 4 – Proliferating CGNs intermingle with migrating CGNs and have a longer cell-cycle.

(**A**) Coronal sections of P9 cerebella of *Plxnb2*$^{fl/fl}$ control and *En1*^{Cre}*;Plxnb2*$^{fl/fl}$ littermates injected with EdU 2 h before perfusion. EdU labels proliferating CGN precursors and Calbindin (CaBP) immunostaining labels Purkinje cells. Sections were counterstained with DAPI. In control, proliferating CGNs (EdU^{+}) are restricted to the outer layer of the EGL (oEGL). In *Plxnb2* mutant, EdU^{+} CGN precursors are found throughout the EGL. The developing molecular layer, containing CaBP^{+} Purkinje cell dendrites, is thinner in *Plxnb2* mutant. The graph shows the quantification of the thickness of the EGL, oEGL, and molecular layer (ML). Error bars represent SEM. EGL: 42.63 ± 1.19 µm in ctl *vs.* 43.62 ± 2.04 µm, in mut, MWU(295) p=0.77, NS: not significant. oEGL 24.78 ± 0.42 µm in ctl *vs.* 35.32 ± 0.76 µm in mut. MWU(70) p < 0.0001. ML: 32.04 ± 0.71 µm in ctl *vs.* 27.44 ± 0.64 µm in mut. MWU(159) p= 0.027. (Figure 4-source data 1) (**B**) Coronal sections of P9 cerebella from *Plxnb2*$^{fl/fl}$ control and *En1*^{Cre}*;Plxnb2*$^{fl/fl}$ littermates, immunostained for Ki67 and Tag1. Ki67 labels proliferating CGN precursors in the oEGL and Tag1 postmitotic CGNs that migrate tangentially in the inner EGL (iEGL). These two populations of precursors and postmitotic neurons are strictly separated in controls, whereas they intermingle in *Plxnb2* mutants. (**C**) Sagittal sections of P8 cerebella from *Plxnb2*$^{fl/fl}$ and *En1*^{Cre}*;Plxnb2*$^{fl/fl}$ littermates injected with EdU 2 h, or 24 h prior to

fixation. EdU^+ cells were counted and averaged from 3 sections per animal from 5 ctl and 5 mut animals. No difference in the production of new CGNs between 2 and 24h of EdU were observed. Graph shows the percentage of EdU^+ cells in the EGL after 24 h compared to 2 h (ctl 157.4 ± 12.64% *vs.* mut 168.8 ± 9.22%, MWU(9), p = 0.55, not significant). Error bars represent SEM. (Figure 4-source data 1) Graph in Figure 4-figure supplement 1A shows that there is no difference in the raw amount of EdU^+ cells per μm^3 after 2 h or 24 h post-injection as counted from these sections (Figure 4-figure supplement 1-source data 1). (**D**) Immunohistochemistry of sagittal sections of P9 cerebella from *Plxnb2*$^{fl/fl}$ and *En1*^{Cre}*;Plxnb2*$^{fl/fl}$ littermates injected with EdU 24 h prior to fixation. EdU labels cells that started their division cycle in the last 24 h while H3P staining labels dividing cells. The graph shows the amount of cells in the EGL that are both EdU and H3P positive is higher in the *Plxnb2* mutant. Error bars represent SEM. Ctl: 2.44 ± 0.29% *vs.* mut: 6.45 ± 1.07%. MWU(0) p = 0.0079. (Figure 4-source data 1) Scale bars: 50 μm in A, B, C and D, 10 μm in high magnification panels of D.

Figure 5 – *Plxnb2* mutant CGNs display aberrant proliferative and tangential stages.

(**A**) Schematic representation of the *in vivo* cerebellum electroporation protocol. See methods for details. (**B**) Cerebellar sections of electroporated brains at 1 day, 2 days, 1 week and 3 weeks after electroporation at P7, to illustrate the different stages of CGN development. Sections were immunostaining for GFP, Calbindin (CaBP), to label Purkinje cells. EdU was injected 2 h prior to fixation, to label proliferating CGNs in the oEGL. One day after electroporation, GFP^+ CGNs are still proliferating or became postmitotic and initiated tangential migration. 2 days after electroporation

GFP$^+$ CGNs start to migrate radially towards the IGL. 1 week after electroporation all GFP$^+$ CGNs reached the IGL, where they start growing dendrites. After 3 weeks, GFP$^+$ cells have their characteristic morphology with 3-4 claw-shaped dendrites. (**C**) Immunohistochemistry of coronal sections of cerebellum 1 day post-electroporation. GFP shows the electroporated CGNs and EdU, which was injected 2 h before fixation, labels proliferating CGNs. Both the distribution and the morphology of migrating *Plxnb2* mutant GFP$^+$ CGNs are altered. (**D**) The graph shows aberrant process length of tangentially migrating CGNs in *En1^{Cre};Plxnb2$^{fl/fl}$* pups. Error bars represent SEM. Bipolar leading process (longest process): ctl 70.86 ± 3.94 µm *vs.* mut 52.12 ± 2.92 µm, MWU(955) p = 0.0002. Bipolar trailing process: ctl 31.1 ± 2.68 µm *vs.* mut 23.1 ± 1.84 µm, MWU(1117) p = 0.0057. Unipolar leading process: ctl: 52.71 ± 9.32 µm *vs.* mut 45.07 ± 3.02 µm. MWU(416) p = 0.75 (not significant). 44 wildtype bipolar cells and 73 mutant bipolar cells from, and 16 wildtype unipolar and 66 mutant unipolar cells of 6 wildtype and 4 *Plxnb2* mutant animals were quantified. (Figure 5-source data 1) (**E**) Quantification of the % of EDU + and GFP+ GCNs. In *Plxnb2* mutants, many bipolar GFP+ GCNs are also EdU$^+$, unlike in controls (see Figure 5-figure supplement 1). By contrast the % EdU+/GFP+ GCN precursors is similar in *Plxnb2$^{fl/fl}$* controls and *En1^{Cre};Plxnb2$^{fl/fl}$* mutants. 447 ctl and 297 mutant precursors, and 451 ctl and 533 mutant bipolar CGNs were counted, from 6 wildtype and 4 *Plxnb2* mutant animals. Error bars represent SEM. Precursors: ctl 53.91 ± 3.01% *vs.* mut 42.97 ± 9.51%, MWU(8) p = 0.48 (not significant). Bipolar cells: ctl 6.82 ± 1.17% *vs.* mut 27.53 ± 4.86%, MWU(0) p = 0.0095. (Figure 5-source data 1) (**F**) P8 coronal sections of the cerebellum, 1 day post-electroporation. Mitotic GCNs in the EGL are immunostained with anti-H3P antibodies. At this stage, GFP$^+$ cells are either in a precursor state (outlined and marked P) or display a clear bipolar

morphology (outlined and marked B) and express Tag1, a marker of tangentially migrating CGNs. In controls, only GCN precursor cells express H3P, whereas in *Plxnb2* mutants, H3P is found in precursors but also in some Tag1+ bipolar GCNs. (**G**) Coronal sections of the cerebellum 2 days post-electroporation. GFP immunostaining labels the electroporated CGNs, and EdU (injected 2 h before fixation) stains proliferating CGNs. Calbindin (CaBP) labels Purkinje cells. GFP^+ cells were counted and grouped in radial, tangential and precursor cell stages based on their morphology. In controls, most CGNs have reached radial stage 2 days after electroporation. By contrast, many GFP+ CGNs are still in the tangential phase in *Plxnb2* mutants. Radial CGNs are not labelled by EdU. Graph shows that in *Plxnb2* mutants, more cells are in the radial stage (ctl 50 ± 2.77% *vs.* mut 38.28 ± 2.37%, MWU(1) p = 0.0159) and less cells in the tangential stage (ctl 34 ± 1.33% *vs.* mut 47.85 ± 2.37%, MWU(0) p = 0.0079). There is no significant difference in cells still in the precursor stage (ctl 16 ± 1.98% *vs.* mut 13.9 ± 1.71%. MWU(10) p = 0.65). Error bars represent SEM. 899 ctl and 744 mutant CGNs were counted, from 5 animals per genotype. (Figure 5-source data 1) (**H**) Sagittal sections of the cerebellum more than 3 weeks after electroporation with GFP. Electroporated CGNs are stained with GFP, Purkinje cells with Calbindin (CaBP) and sections were counterstained with DAPI. 3 different types of defects are seen in *Plxnb2* mutants: I) Parallel fibers that usually occupy a thin part within the molecular layer (Ia) disperse through the entire molecular layer in the mutant (Ib); II) Whereas the white matter of control cerebella is devoid of parallel fibers (IIa), some mutant CGNs send their axons into the cerebellar white matter (IIb); and III) ectopic patches of CGNs accumulate at the cerebellar. Ectopic GCNs still acquire their characteristic morphology.

Scale bars: B, C, E: 50 µm; D: 10 µm; F overview panels: 500 µm, high magnification panels: 20 µm.

Figure 6 – Abnormal parallel fiber layering in *Plxnb2* mutants

(**A**) Coronal sections of the cerebellum of P25 mice electroporated with GFP at P7 and re-electroporated with tdTomato (tdTom) at P11. Double immunostaining for GFP and tdTomato. In control (left) the parallel fibers of CGNs that became postmitotic early (GFP^+) are at the bottom of the molecular layer, whereas the CGNs that became postmitotic later ($tdTom^+$) extend parallel fibers at the surface of the molecular layer. In $En1^{Cre};Plxnb2^{fl/fl}$ mutants, there is an important overlap in the molecular layer, between parallel fibers of early and late-born CGNs. The graph ss a quantification of the portion of the molecular layer that is occupied by parallel fibers of either early (GFP^+) or late ($tdTom^+$) CGNs (eg. (GFP^+ width / ML total width) x 100%). Error bars represent SEM. The molecular layer measurements and its double-electroporated parallel fiber content was averaged from 3 different points per cerebellum from 7 $Plxnb2^{fl/fl}$ and 4 $En1^{Cre};Plxnb2^{fl/fl}$ cerebella. P7 GFP ctl: 31.96 ± 2.07% *vs.* mut: 81.48 ± 4.53% (MWU(0) p = 0.0061) and P11 tdTom ctl: 27.45 ± 2.26% *vs.* mut: 68.74 ± 2.75% (MWU(0) p = 0.0061). (Figure 6-source data 1) (**B**) Coronal sections of cerebella electroporated at P7 and collected at P9 (EdU was injected 2h before termination). Sections were stained for GFP, CaBP and EdU. In controls (left panel), nascent parallel fibers normally extend at the base of the iEGL, just above the tips of developing Purkinje dendritic arbors (yellow arrowheads). However, in *Plxnb2* mutant (right panel) parallel fibers extend throughout the EGL and cross the Purkinje dendrites in the ML (yellow arrowheads indicate the tips of Purkinje dendrites). (**C**) The abnormal presence of young GFP+ parallel fibers deep

in the molecular layer is also seen on coronal sections of cerebella electroporated at P11 and collected at P13 (Control, left panel and *Plxnb2* mutant, right panel). Scale bars 50 µm.

Figure 7 – *Plxnb2* CGNs recapitulate *in vitro* the developmental defects found *in vivo*.

(**A**) EGL explants from P4-P5 wildtype cerebella, fixed after 1, 2, 3 and 5 days *in vitro* (DIV). Immunocytochemistry for βIII-tubulin and DAPI shows that cells migrate away from the explant and extend long neurites. After DIV2, cells start accumulating in clusters around the original explant. (**B**) EGL explants from P4-P5 $Plxnb2^{fl/fl}$ and $En1^{Cre};Plxnb2^{fl/fl}$ cerebella at DIV1. Cultures were stained for DAPI and βIII-tubulin. *Plxnb2* mutant explants show DAPI+ nuclei closer to the explant and different neurite outgrowth. (**C**) $DAPI^{+}$ nuclei around the explant were counted and their migration was assessed using a Sholl-analysis. Graph shows that less cells migrate from $En1^{Cre};Plxnb2^{fl/fl}$ explants and that they stay closer to the explant. Multiple t-test with the Holm-Sidak method were applied to the mean intersections of DAPI-positive nuclei with the Sholl circles. $p < 0.0001$. 36 ctl and 34 mutant explants were analyzed from 3 different experiments. Error bars represent SEM. (Figure 7-source data 1) (**D**) EGL explants from cerebella electroporated *ex vivo* with GFP and fixed at DIV1 and DIV2. Immunocytochemistry for GFP and DAPI shows the morphology of migrating cells. GFP+ CGNs have either a multipolar (m) or a bipolar (b) shape. After DIV2, almost all GFP^{+} cells have a bipolar morphology, with their trailing process attached (b-a) or not (b-na) to the explant. (**E**) Quantification of the proportion of GFP^{+} CGNs with multipolar or bipolar morphologies. Data is expressed as percentage from total number of GFP^{+} cells per explant ± SEM. DIV1 multipolar: ctl 48.88 ± 2.65% *vs.* mut

65,42 ± 2.37%, MWU(353) p < 0.0001. DIV1 bipolar: ctl 51.12 ± 2.65% *vs.* mut 34.58 ± 2.37%, MWU(353) p < 0.0001. DIV2 multipolar ctl 11.36 ± 1.33% *vs.* mut 17.58± 3.02%, MWU(226) p = 0.13, not significant. DIV2 bipolar ctl 88.67 ± 1.37% *vs.* mut 80.31 ± 3.07%, MWU(189) p = 0.03. All GFP^+ cells (amounts between brackets) were counted from 46 ctl (2728) and 33 mut (835) explants (DIV1) and 32 ctl (2284) and 19 mut (617) explants (DIV2) from at least 3 different experimental repeats. (Figure 7-source data 1) (**F**) Quantification (Box-plots) of leading and trailing process length of bipolar GFP^+ CGNs at DIV1. Leading ctl 106 ± 3.9 µm *vs.* mut 67.6 ± 5.62 µm, MWU(11147) p < 0.0001; trailing ctl 79.5 ± 3.4 µm *vs.* mut 40.9 ± 2.76 µm, MWU(68833) p < 0.0001. 385 ctl and 93 mut cells were analyzed from 29 ctl and 13 mut explants from 3 experimental repeats. (Figure 7-source data 1) (**G**) Proportion of bipolar GFP^+ CGNs attached to the explant. DIV1 attached: ctl 52.19 ± 2.49% *vs.* mut 50.55 ± 4.27%, (MWU(709.5) p = 0.63, not significant. DIV2 attached: ctl 53.63 ± 2.69% *vs.* mut 34.92 ± 2.31%, MWU(36.5) p < 0.0001. All GFP^+ cells (amounts between brackets) were counted from 46 ctl (2728) and 33 mut (835) explants (DIV1) and 32 ctl (2284) and 19 mut (617) explants (DIV2) from at least 3 different experimental repeats. (Figure 7-source data 1) Scale bars: overviews 500 µm (A, B, D); magnifications in D: 50 µm.

Figure 8 – *Plxnb2* mutant CGNs in culture display aberrant tangential migration.

(**A**) 15-minute-time-lapse confocal still images at t 0, 1, 2, 3, 4, and 5 hours showing GFP^+ CGNs migrating from a DIV1 explant (located on the left side of the images). Scale bars 50 µm. (**B**) Bipolar CGNs migrate at an equal speed. (ctl: 26.75 ± 1.23 µm/h *vs.* mut: 27.77 ± 1.25 µm/h, MWU(973) p =0.75, not significant). 45 bipolar cells

were tracked for each condition, from 13 ctl and 11 mut cultures from 5 independent experiments. Error bars represent SEM. (**C**) *En1*^{Cre};*Plxnb2*$^{fl/fl}$ CGNs cover more distance (ctl 9.42 ± 1.60% *vs.* mut 32.21 ± 3.10%, MWU(306) $p < 0.0001$) and spend more time (ctl 15.15 ± 1.77% *vs.* mut 35.86 ± 2.80%, MWU(352.5) $p < 0.0001$) going in negative direction (towards instead of away from the explant). 45 bipolar cells were tracked for each condition, from 13 ctl and 11 mut cultures. Error bars represent SEM. (Figure 8-source data 1)

Figure 9 – Aberrant proliferation of CGN precursors in *Plxnb2* mutant explants. (**A**) EGL explants from P4-P5 cerebella at DIV1. 2 hours prior to fixation, 10 µM EdU was added to the culture medium. Cultures were stained for EdU, H3P and DAPI. (**B**) The number of DAPI$^+$ nuclei/migrating cells around DIV1 explants, is significantly decreased in *Plxnb2* mutants (485.79 ± 34.77 cells) compared to controls (748.89 ± 53.54 cells; MWU(290.5) $p = 0.0001$). Error bars represent SEM. 36 ctl and 34 mut explants were analyzed from 3 different experiments. (Figure 9-source data 1) (**C**) At DIV1, there is no significant difference in the total amount of EdU$^+$ cells (that incorporated EdU in the last 2 hours) per explant. Ctl 75.19 ± 11.28 *vs.* mut 72.03 ± 7.85 cells (MWU(596.5) $p = 0.86$. Error bars represent SEM. 36 ctl and 34 mut explants were analyzed from 3 different experimental replicates. (Figure 9-source data 1) (**D**) Likewise, the portion of EdU$^+$ cells also positive for H3P (an M-phase marker) at the moment of fixation) is similar in controls (13.77 ± 3.80%) and mutants (14.10 ± 0.93%, MWU(477) $p = 0.11$). Error bars represent SEM. 36 ctl and 34 mut explants were analyzed from 3 different experimental repeats. (Figure 9-source data 1) (**E**) EGL explants from P4-P5 cerebella electroporated with GFP *ex vivo*. 10 µM EdU was added to the medium after 6 hours of culture. Explants were fixed at DIV1

or DIV2 and EdU incorporation was quantified in multipolar and bipolar GFP$^+$ cells. (**F**) Quantification of the proportion of multipolar and bipolar GFP$^+$ CGNs that have taken up EdU in the past 18 h at DIV1 (EdU administered from 6 to 24h after plating). Multipolar ctl: 9.394 ± 1.35% *vs.* mut 13.75 ± 2.31%, MWU(595) p = 0.10, not significant; bipolar ctl: 0.41 ± 0.27% *vs.* mut 0.47 ± 0.27%, MWU(740) p = 0.78, not significant. Error bars represent SEM. 2814 ctl and 890 mut GFP$^+$ CGNs were counted from 47 ctl and 33 mut explants from 3 experimental replicates. (Figure 9-source data 1) (**G**) Quantification of the proportion of multipolar and bipolar GFP$^+$ CGNs that have taken up EdU in the past 42 h at DIV2 (EdU administered from 6 to 48h after plating). Multipolar ctl: 69.81 ± 4.50% *vs.* mut 77.03 ± 6.55%, MWU(189) p = 0.25, not significant. Bipolar ctl: 7.76 ± 1.00% *vs.* mut 23.3 ± 4.20%, MWU(113) p = 0.0001. Error bars represent SEM. 2284 ctl and 617 mut GFP-positive cells were counted from 32 ctl and 20 mut explants from 3 experimental repeats. (Figure 9-source data 1) Scale bars 100 µm, high magnifications 10 µm.

Figure 10 – Aberrant CGN (precursor) motility before and after division in *Plxnb2* mutant explants.

(**A, B**) Time-lapse confocal imaging series (21 hours) of GFP$^+$ multipolar CGNs in control (A) and *Plxnb2* mutant explants at DIV1. (**A**) In a control, a multipolar cell (outlined in pink at t 0 (h) divides (cytokinesis, t 16h) to give rise to two daughter cells (1 and 2) which later adopt a bipolar morphology. (**B**) In a *Plxnb2* mutant, multipolar cells (outlined in pink) are more motile and the transition to the bipolar stage is delayed. Scale bars 50 µm. (**C-F**) Quantifications of multipolar cell velocity, cumulative distance before cytokinesis, time that daughter cells take to become bipolar after cytokinesis, and the amount of visible divisions of GFP-positive cells per

hour. Error bars represent SEM. 75 ctl and 107 mut multipolar GFP-positive CGNs were tracked from 13 ctl and 11 mutant explants from 5 different experimental repeats. (**C**) Velocity ctl 25.41 ± 1.04 µm/h *vs.* mut 34.11 ± 1.24 µm/h, MWU(2279) p < 0.0001. (Figure 10-source data 1) (**D**) Cumulative distance ctl 196.3 ± 11.08 µm *vs.* mut 321.8 ± 19.73 µm, MWU(2516) p < 0.0001. (Figure 10-source data 1) (**E**) Time before bipolarity ctl 7.80 ± 0.45 h *vs.* 9.21 ± 0.44 h, MWU(3254) p = 0.0298. (Figure 10-source data 1) (**F**) Divisions per hour ctl 0.044 ± 0.016 *vs.* mut 0.11 ± 0.027, MWU(36) p = 0.034. (Figure 10-source data 1)

Figure 3 Supplement 1 – Difference in cerebellar volume but not motor function.

(**A**) Quantification of cerebellar volume was done by 3D segmentation of the cerebellum in Imaris. Data is normalized to control cerebellum (dotted line at 100%) P4: 85.64 ± 4.425%. Mann Whitney U (MWU) test. MWU(0) p = 0.0079, N = 5 ctl and 5 mut. P30: 84.03 ± 1.808%. MWU(0) p = 0.0022, N = 6 ctl and 6 mut. (Figure 3-figure supplement 1-source data 1) (**B**) Quantification of the time to fall in rotarod assay on three consecutive trial. Day1 ctl 151.3 ± 16.6 s vs. mut 132.6 ± 9.7 s (Not significant); Day 2 ctl 155.6 ± 16.1 s vs. mut 169.8 ± 10.0 s (Not significant); Day 3 ctl 168.8 ± 20.8 s vs. mut 189.9 ± 12.5 s (Not significant). 6 control and 10 mutant mice, 19 weeks old, were tested. (Figure 3-figure supplement 1-source data 1)

Figure 4-figure supplement 1 - No difference in amounts of EdU^+ and $H3P^+$ CGNs in EGL.

(**A**) Graph shows the quantification of the amount of EdU^+ cells 2 h and 24 h after EdU injection as described in Figure. 4D, and the amount of H3P-positive cells per

1562 μm^3 of EGL. EdU^+ and $H3P^+$ cells were counted and averaged from 3 sections per
1563 animal from 5 ctl and 5 mut animals. 2h EdU: ctl $1{,}01e^{-3} \pm 8.76e^{-5}$ *vs.* mut $0.89e^{-3} \pm$
1564 $3.06e^{-5}$ cells μm^{-3} EGL, MWU(8), p = 0.42, not significant. 24h EdU: ctl $1{,}55e^{-3} \pm$
1565 $12.46e^{-5}$ *vs.* mut $1.51e^{-3} \pm 8{,}08e^{-5}$ cells μm^{-3} EGL, MWU(12.5), p > 0.99, not
1566 significant. H3P: ctl $0.19e^{-3} \pm 5.21e^{-5}$ *vs.* mut $0.29e^{-3} \pm 2.84e^{-5}$ cells μm^{-3} EGL,
1567 MWU(5), p = 0.15. Error bars represent SEM. (Figure 4-figure supplement 1-source
1568 data 1) (**B**) 50um thick slices of P8 brains 2h after EdU injection were immunostained
1569 for EdU and Ki67 to assess CGN proliferation rate. Spot detection in Imaris software
1570 was used to count EdU- and Ki67-positive cells in comparable stretches of EGL. 3 to
1571 4 slices per brain were analyzed. Colocalization is represented as percentage of
1572 EdU-positive spots, that are also Ki67-positive. Ctl 53 ± 7.36% vs. mut 51.8 ± 5.3%,
1573 MWU(8) p = 0.67, data averaged from 4 control and 5 mutant brains. Error bars
1574 represent SEM. (Figure 4-figure supplement 1-source data 1)
1575
1576 **Figure 5-figure supplement 1 – Identity of electroporated cells and**
1577 **quantification of morphological features.**
1578 (**A**) Immunohistochemistry of coronal sections of cerebellum 2 days post-
1579 electroporation. GFP shows the electroporated cells and Pax6 marks pre- and
1580 postmitotic CGNs. Graph shows that 99.6 ± 0.21% of all GFP-positive cells are also
1581 Pax6-positive. Error bars represent SEM. 198 ctl and 382 mutant GFP^+ cells were
1582 counted and pooled from 4 animals. (Figure 5-figure supplement 1-source data 1) (**B**)
1583 Graph shows quantification of cell body measurements of GFP^+ CGNs 1-day-post-
1584 electroporation as shown in Figure 5C. Cells can be classified as precursors, of
1585 CGNs with unipolar or bipolar morphologies. No difference is seen between controls
1586 and *Plxnb2* mutants. Width/length ratio of 74 ctl and 159 mut CGNs from 3 different

pups per genotype were calculated. Bipolar cells: ctl 0.47 ± 0.02 *vs.* mut 0.45 ± 0.02, MWU(1400) p = 0.25; Unipolar cells: ctl 0.42 ± 0.03 *vs.* mut 0.47 ± 0.02, MWU(382) p = 0.43; Precursors: ctl 0.62 ± 0.03 *vs.* mut 0.57 ± 0.03, MWU(509) p = 0.26. Error bars represent SEM. (Figure 5-figure supplement 1-source data 1) (**C**) EGL of cerebella electroporated 24 h before isolation at P8 were equally divided in two bins. 6 control and 4 mutant brains were analyzed. All GFP^+ cells were counted and quantified as multipolar or bipolar. CGN-appearance per bin was then analyzed as a percentage of total CGNs in that morphology. Percentage of all multipolar cells residing in bin 1 ctl 87.5 ± 3.19% *vs.* mut 70.41 ± 1.2% MWU(0) p=0.0095; Percentage of all bipolar cells residing in bin 2 ctl 90.22 ± 2.64% *vs.* mut 52.24 ± 2.34% MWU(0) p=0.0095; Bipolar in ML ctl 5.19 ± 2.84% *vs.* 27.89 ± 4.17% MWU(0) p=0.0095. Error bars represent SEM. (**D**) High magnification images of Immunohistochemical staining of *En1^{Cre};Plxnb2$^{fl/fl}$* P8 brains showing bipolar GFP^+-CGNs that bear both proliferation markers EdU (injected 2 h before brain isolation) and H3P. (**E**) Representative examples of *Plxnb2$^{fl/fl}$* and *En1^{Cre};Plxnb2$^{fl/fl}$* CGNs 2 days post-electroporation. Axons and leading processes are pointed out. Graphs show axon and leading process lengths, and ratio of cell body width and length. Error bars represent SEM. No significant difference is found in process length (leading process: ctl 28.11 ± 0.72 µm *vs.* mut 30.86 ± 1.67 µm, MWU(17024) p = 0.27; axon length: ctl 60.07 ± 2.5 µm *vs.* mut 64.98 ± 3.0 µm, MWU(17380) p = 0.44). *Plxnb2* mutant CGNs in their radial phase appear slightly rounder (width/length ratio ctl 0,47 ± 0.01 *vs.* mut 0.55 ± 0.01, MWU(13379) p < 0.0001). 199 ctl and 183 mut CGNs were analyzed from at least 3 different pups per genotype. (Figure 5-figure supplement 1-source data 1) (**F**) Representative examples of *Plxnb2$^{fl/fl}$* and *En1^{Cre};Plxnb2$^{fl/fl}$* CGNs, 2 and 3 weeks after electroporation. (**G**) Whisker plots show

quantification results from cells as in (**F**). In P20 *En1^{Cre};Plxnb2$^{fl/fl}$* mutants, more CGNs have acquired their characteristic mature morphology, with 3-4 claw-shaped dendrites. 198 ctl and 251 mutant CGNs at P20, and 204 ctl and 213 mutant CGNs at P30 were analyzed from at least 3 different pups from each age and genotype. No significant difference was found in cell body measurements at P20 and P30, and the number of dendrites was also similar at P30. However, at P20 a higher portion of mutant CGNs, electroporated at P7 with GFP, already pruned their dendrites to the amount of 4 (MWU(21308) $p < 0.0001$). (Figure 5-figure supplement 1-source data 1) Scale bar A, C, D: 10 µm.

Figure 5-figure supplement 2 – Misplaced and misprojecting CGNs keep their identity.

(**A**) Immunohistochemistry of a sagittal section from an *En1^{Cre};Plxnb2$^{fl/fl}$* cerebellum, more than 3 weeks after electroporation with GFP. GFP labels electroporated CGNs, Calbindin (CaBP) stains Purkinje cells, MOG stains myelin, and sections were counterstained with DAPI. (**B**) High magnification of the framed region in (A) showing that CGN axons misprojecting in the white matter are not myelinated, similar to parallel fibers in control cerebella.

Scale bars: A: 500 µm; B: 5 µm.

Figure 6-figure supplement 1 – Abnormal localization of parallel fiber synapses in *Plxnb2* mutant.

(**A**) Mice were electroporated with GFP at P7 and their cerebellum collected at P9. Sagittal sections were incubated with antibodies against GFP (to label CGNs and parallel fibers), Calbindin (CaBP, Purkinje cells) and Vglut1 (parallel fiber synapses).

In Controls, the density of VGlut1$^+$ synapses is high along the proximal regions of Purkinje cell dendrites and low at their tips. In the molecular layer of *Plxnb2* mutants, GFP$^+$ fibers are disorganized, and there is a high density of Vglut1 puncta on both proximal and distal CaBP$^+$ dendritic branches. Graph shows the quantification of the ratio between the fluorescent integrated density of distal and proximal Vglut1-labelling. Ctl: 0.21 ± 0.03 *vs.* mut 0.64 ± 0.07, MWU(0) p = 0.028. Vglut1 integrated density was measured and averaged from 5 distal and 5 proximal 10 x 10 µm squares taken from different Purkinje cells per animal, from 4 animals for both genotypes. Error bars represent SEM. (Figure 6-figure supplement 1-source data 1) (**B**) Sagittal sections of the cerebellum at P30, immunolabelled for Calbindin (Purkinje cells) and Vglut1 (parallel fibers/Purkinje Cell synapses). The synaptic distribution of Vglut1$^+$ synapses appears similar in control and *Plxnb2* mutants. Scale bars A, B, C: 50 µm.

Figure 7-figure supplement 1 – Migrating cells have a CGN identity.

(**A**) Immunocytochemistry of DIV2 EGL explants for Pax6 (pre- and postmitotic CGNs) with DAPI counterstaining. Cells were counted in 400x400 pixel squares close to the explant. Almost all migrating cells are Pax6$^+$ in controls (Pax6$^+$/DAPI$^+$ ctl 98.78 ± 0.28%) and *Plxnb2* mutants (98.64 ± 0.43%, MWU(68) p = 0.83, not significant). In total 2412 and 2361 DAPI-positive cells were counted from 19 ctl and 18 mut explants respectively from 3 different experiments at DIV1 and DIV2. (Figure 7-figure supplement 1-source data 1) (**B**) Immunocytochemistry of EGL explants at DIV2 for GFAP (glia) with DAPI staining. Explants contain glia but their cell bodies do not exit the explant.

Scale bars: low magnifications 100 µm, high magnifications 10 µm.

Figure 7-figure supplement 2 – Electroporated cells migrating away from EGL explants have CGN identity.

(**A**) EGL explants from P4-P5 cerebella electroporated *ex vivo* with GFP just before culture. Immunocytochemistry for GFP and Pax6 with DAPI staining shows that in both controls and *Plxnb2* mutants (almost) all GFP+ cells are also Pax6+ (white arrows; $Pax6^+/GFP^+$ ctl 98.77 ± 0.70% *vs.* mut 98.61 ± 0.64%, MWU(28.5) p = 0.72, not significant). Error bars represent SEM. Cells were counted from 8 DIV1 explants from both genotypes (667 ctl and 348 mut cells). (Figure 7-figure supplement 2-source data 1) (**B**) E*x vivo* GFP-electroporated EGL explants at DIV2 immunostained for GFP and Sema6A (tangentially migrating CGNs) and counterstained with DAPI. High magnifications show that GFP^+ cells co-express Sema6a. (**C**) E*x vivo* GFP electroporated EGL explants at DIV2 immunostained for GFP and GFAP and counterstained with DAPI. High magnifications show that GFP^+ cells are not positive for glial markers.

Scale bars: A: 50 µm; B, C: overview panels 100 µm, high magnifications 10 µm.

Figure 10-figure supplement 1 – Quantification of the distribution of multi- and bipolar CGNs during time-lapse.

(**A**) Still images at the beginning (t = 0 h, DIV1) and at the end (t = 18 h, DIV2) of a time-lapse imaging series of migrating GFP^+ CGNs in EGL explants. *Plxnb2* mutant explants show relatively more multipolar-shaped CGNs (arrowheads) compared to controls. After 18 h of imaging, when all CGNs that exited control explants turned bipolar, mutant explants still contain multipolar CGNs (arrowheads). Schematic shows experimental design. 15 min time-lapse recordings were performed from 24h

(DIV1) after plating (t 0), and continued for 18 to 27 h. (**B**) Quantification of the percentages of multipolar- or bipolar-shaped GFP$^+$ cells at the beginning and at the end of time-lapse. Beginning of time-lapse (DIV1) multipolar ctl 32.28 ± 7.17% *vs.* mut 66.61 ± 7.33%, MWU(20.5) p = 0.002; bipolar ctl 66.27 ± 7.89% *vs.* mut 35.56 ± 7.12%, MWU(28.5) p = 0.0111. End of time-lapse (DIV2) multipolar ctl 0.28 ± 0.28% *vs.* mut 11.04 ± 4.63%, MWU(16) p = 0.0001; bipolar ctl 99.72 ± 0.28% *vs.* mut 88.96 ± 4.63%, MWU(16) p = 0.0001. 745 ctl and 414 mut GFP$^+$ cells were counted at the end of recordings from 13 ctl and 11 mut explants from 5 experimental repeats. (Figure 10-figure supplement 1-source data 1) Scale bars: 100 µm.

Video 1 – 3D movie of P4 iDisco+ cleared *Plxnb2$^{fl/fl}$* and *En1^{Cre};Plxnb2$^{fl/fl}$* cerebella. All cell nuclei are stained with TO-PRO-3, Pax6 and FoxP2-staining is used to visualize CGNs and Purkinje cell bodies respectively.

Video 2 – 3D movie of P14 iDisco+ cleared *Plxnb2$^{fl/fl}$* and *En1^{Cre};Plxnb2$^{fl/fl}$* cerebella. All cell nuclei are stained with TO-PRO-3.

Video 3 - 3D movie of P30 iDisco+ cleared *Plxnb2$^{fl/fl}$* and *En1^{Cre};Plxnb2$^{fl/fl}$* cerebella. All cell nuclei are stained with TO-PRO-3.

Video 4 – 3D movie of P20 iDisco+ cleared *En1^{Cre};Plxnb2$^{fl/fl}$* cerebellum stained with TO-PRO-3 for all cell nuclei and FoxP2 to visualize Purkinje cell bodies.

Video 5 - 3D movie of P65 iDisco+ cleared *Plxnb2$^{fl/fl}$* cerebellum electroporated at P7 with GFP. Whole mount immunostaining was performed with GFP to stain

electroporated CGNs, FoxP2 to visualize Purkinje cell bodies, and TO-PRO-3 to stain all cell nuclei and visualize cerebellar anatomy.

Video 6 - 3D movie of P65 iDisco+ cleared *En1^{Cre};Plxnb2$^{fl/fl}$* cerebellum electroporated at P7 with GFP. Whole mount immunostaining was performed with GFP to stain electroporated CGNs, FoxP2 to visualize Purkinje cell bodies, and TO-PRO-3 to stain all cell nuclei and visualize cerebellar anatomy.

Video 7 – Representative examples of confocal time-lapse recording of EGL explant cultures of P4-P5 *Plxnb2$^{fl/fl}$* and *En1^{Cre};Plxnb2$^{fl/fl}$* cerebella with 15 minute interval, starting from DIV1. Cerebella were electroporated *ex vivo* with GFP to visualize individual CGNs and follow their migration over time (some striking examples are pseudo-colored). Control CGNs with a bipolar morphology migrate away from the explant in a straight direction. *Plxnb2* mutant CGNs change their direction of migration multiple times and cover long distances in reverse direction (back to the explant).

Video 8 – Representative examples of confocal time-lapse recording of EGL explant cultures of P4-P5 *Plxnb2$^{fl/fl}$* and *En1^{Cre};Plxnb2$^{fl/fl}$* cerebella with 15 minute interval, starting from DIV1. Cerebella were electroporated *ex vivo* with GFP to visualize individual CGNs and follow their migration over time.

Figure 4 - source data 1: Layer thickness and proliferation markers in EGL.

Figure 5 - source data 1: CGN morphology in vivo and colocalization with proliferation markers.

Figure 6 - source data 1: Parallel fiber distribution.

Figure 7 - source data 1: EGL explants: in vitro CGN morphology.

Figure 8 - source data 1: EGL explants: live imaging of bipolar CGN migration.

Figure 9 - source data 1: EGL explants: in vitro proliferation.

Figure 10 - source data 1: EGL explants: live imaging of multipolar CGNs.

Figure 3-figure supplement 1-source data 1: Cerebellar volume and function.

Figure 4-figure supplement 1-source data 1: No difference in amounts of EdU^+ and $H3P^+$ CGNs in EGL.

Figure 5-figure supplement 1-source data 1: Identity of electroporated cells in vivo, morphology of electroporated CGNs.

Figure 6-figure supplement 1-source data 1: Synaptogenesis between parallel fibers and Purkinje cells.

Figure 7-figure supplement 1-source data 1: Identity of electroporated cells migrating out of EGL explants.

Figure 7-figure supplement 2-source data 1: Identity of cells migrating out of EGL explants.

Figure 10-figure supplement 1-source data 1: Morphology of CGNs during live imaging.

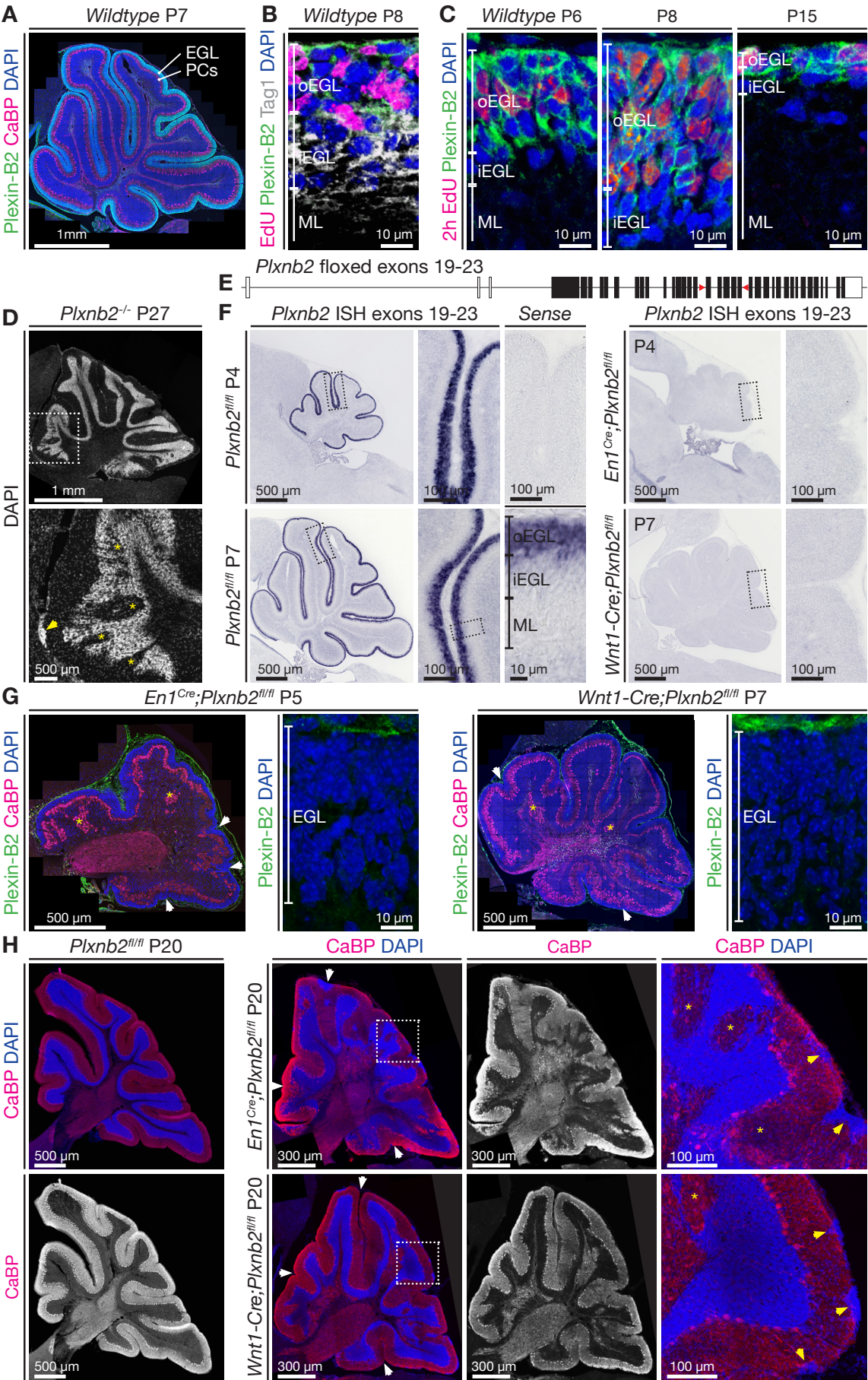
A
Wildtype P7
Plexin-B2 CaBP DAPI
EGL
PCs
1mm
B
Wildtype P8
EdU Plexin-B2 Tag1 DAPI
oEGL
iEGL
ML
10 µm
C
Wildtype P6
P8
P15
2h EdU Plexin-B2 DAPI
oEGL
iEGL
ML
10 µm
E
Plxnb2 floxed exons 19-23
D
Plxnb2-/- P27
DAPI
1 mm
500 µm
F
Plxnb2 ISH exons 19-23
Sense
Plxnb2 ISH exons 19-23
Plxnb2fl/fl P4
Plxnb2fl/fl P7
En1Cre;Plxnb2fl/fl
Wnt1-Cre;Plxnb2fl/fl
P4
P7
500 µm
100 µm
10 µm
G
En1Cre;Plxnb2fl/fl P5
Wnt1-Cre;Plxnb2fl/fl P7
Plexin-B2 CaBP DAPI
Plexin-B2 DAPI
EGL
500 µm
10 µm
H
Plxnb2fl/fl P20
CaBP DAPI
CaBP
En1Cre;Plxnb2fl/fl P20
Wnt1-Cre;Plxnb2fl/fl P20
500 µm
300 µm
100 µm

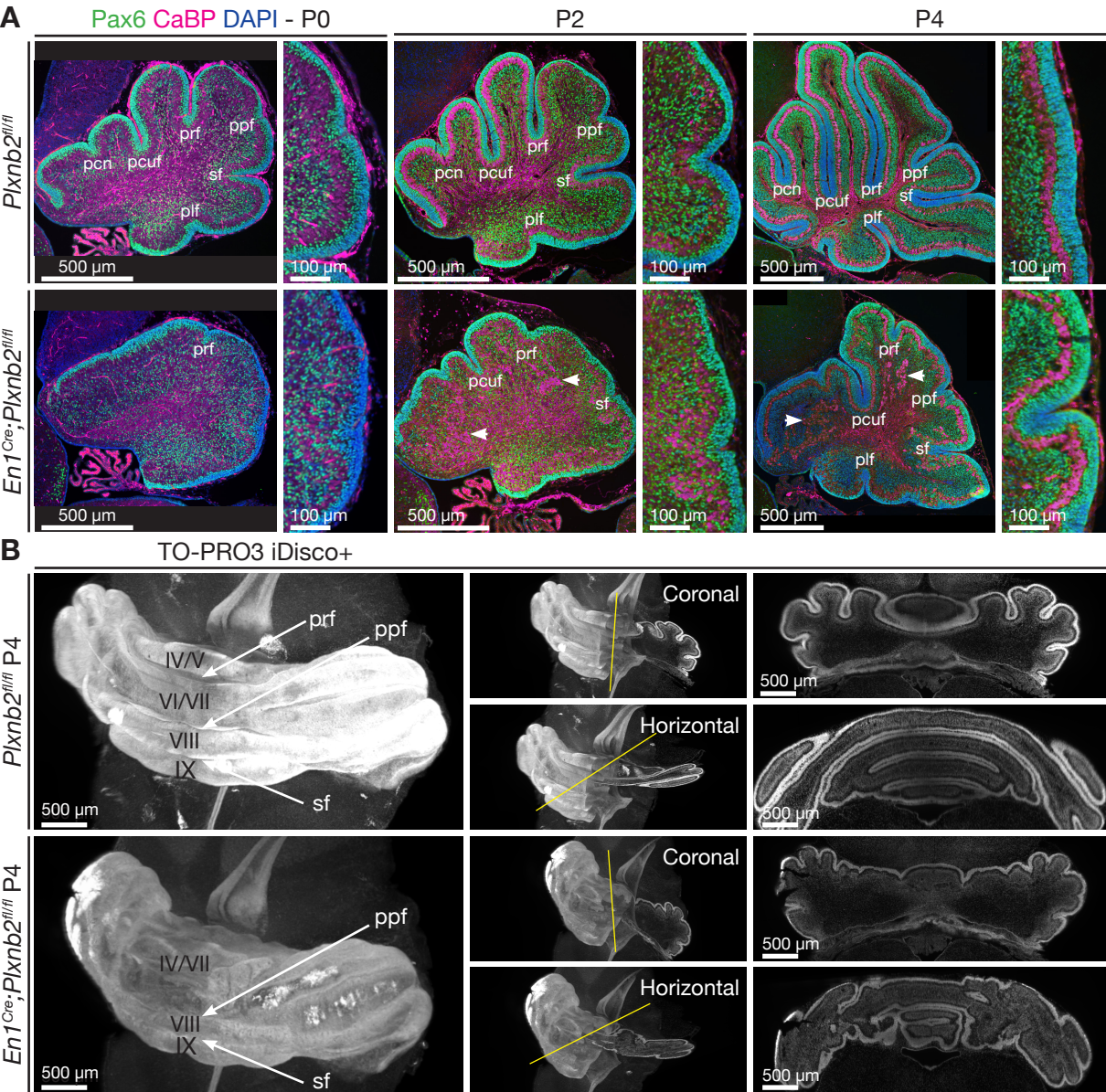
A
Pax6 CaBP DAPI - P0
P2
P4
Plxnb2fl/fl
En1Cre;Plxnb2fl/fl
prf
ppf
pcn
pcuf
sf
plf
500 µm
100 µm
B
TO-PRO3 iDisco+
Plxnb2fl/fl P4
En1Cre;Plxnb2fl/fl P4
IV/V
VI/VII
VIII
IX
IV/VII
Coronal
Horizontal

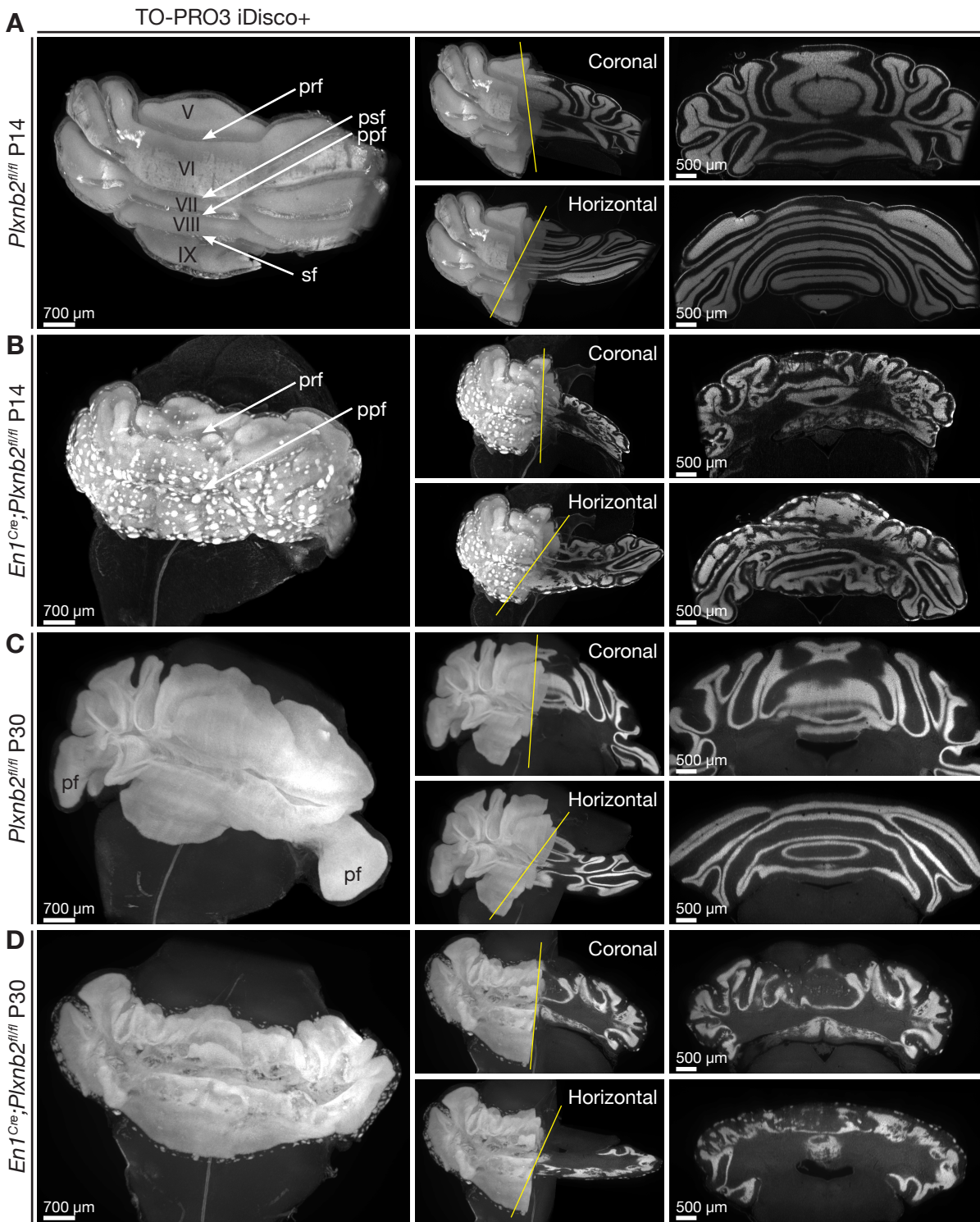
A
TO-PRO3 iDisco+
Plxnb2fl/fl P14
prf
psf
ppf
V
VI
VII
VIII
IX
sf
700 µm
Coronal
500 µm
Horizontal
500 µm
B
En1Cre;Plxnb2fl/fl P14
prf
ppf
700 µm
Coronal
500 µm
Horizontal
500 µm
C
Plxnb2fl/fl P30
pf
pf
700 µm
Coronal
500 µm
Horizontal
500 µm
D
En1Cre;Plxnb2fl/fl P30
700 µm
Coronal
500 µm
Horizontal
500 µm

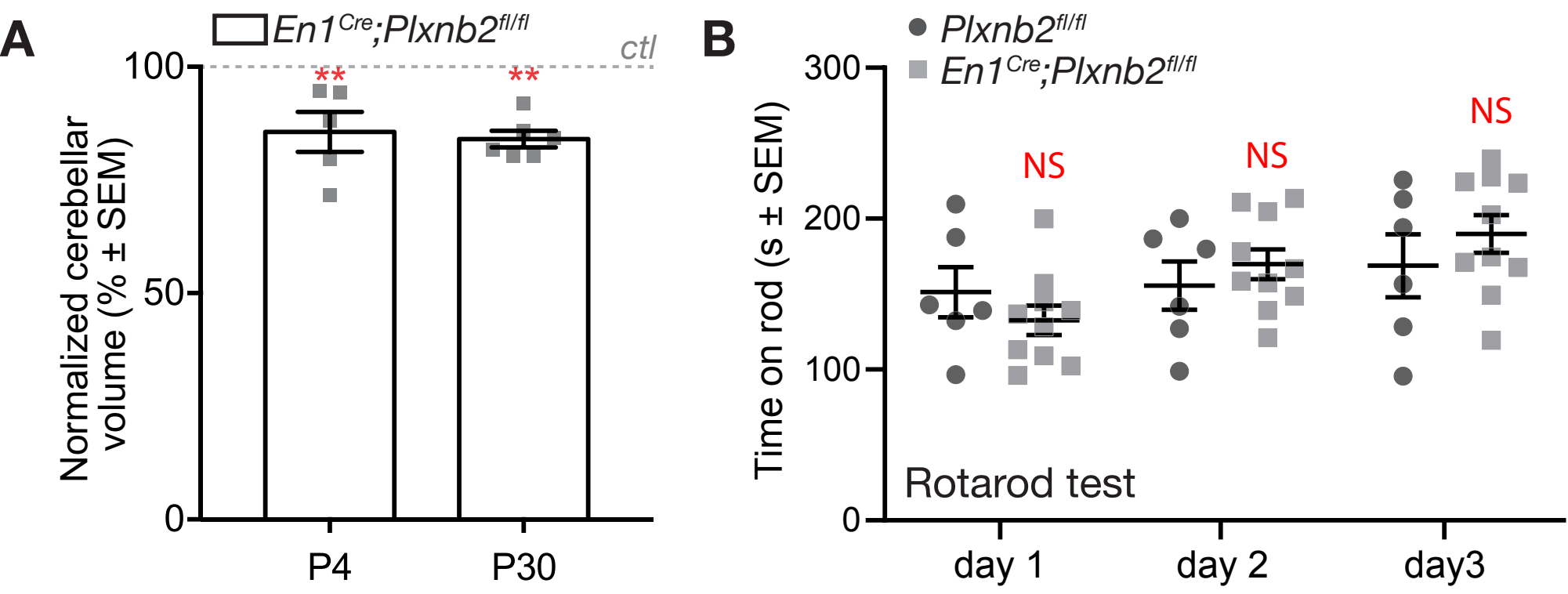
A
En1Cre;Plxnb2fl/fl
ctl
100
50
0
**
**
Normalized cerebellar volume (% ± SEM)
P4
P30
B
Plxnb2fl/fl
En1Cre;Plxnb2fl/fl
300
200
100
0
NS
NS
NS
Time on rod (s ± SEM)
Rotarod test
day 1
day 2
day3

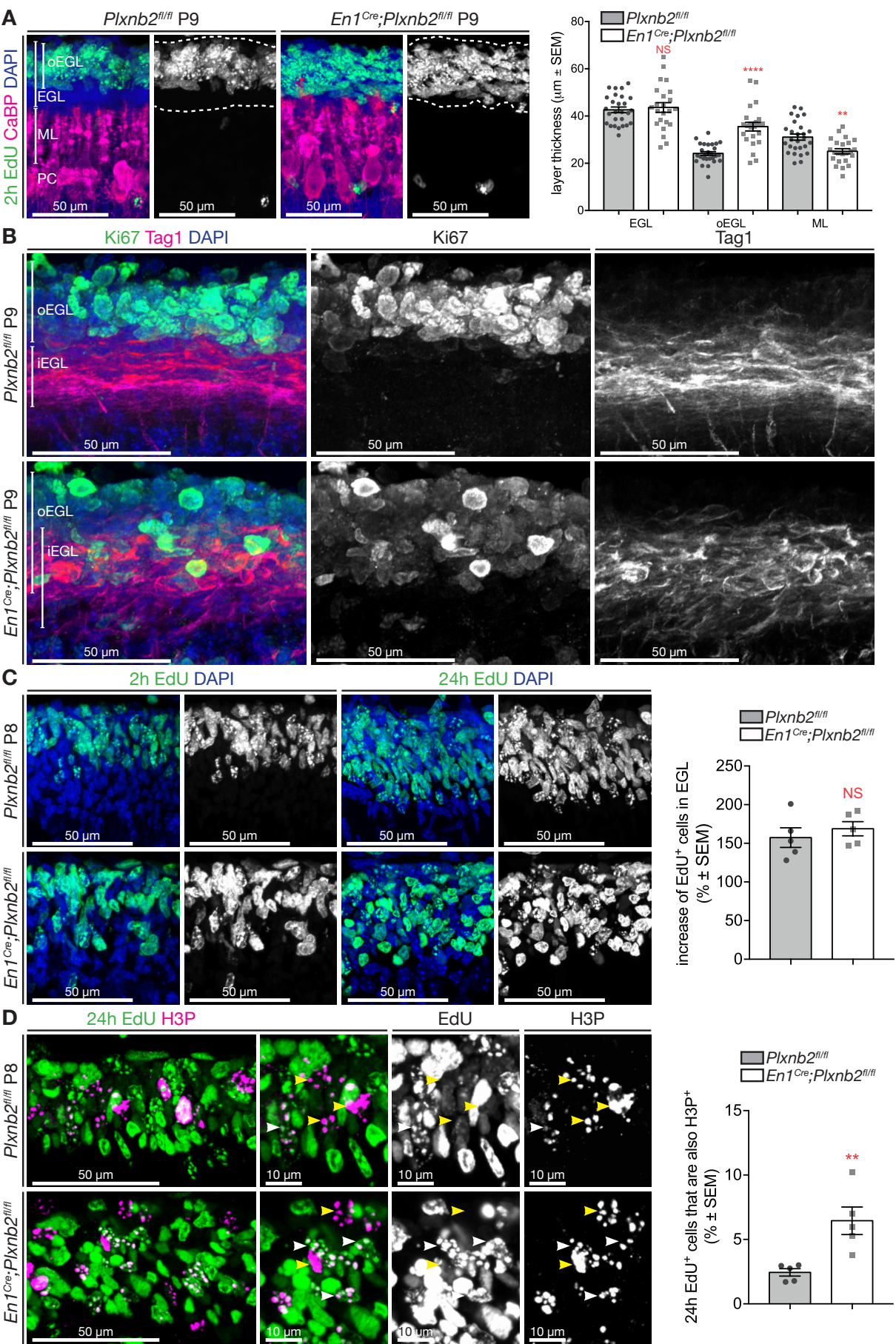
A
Plxnb2fl/fl P9
En1Cre;Plxnb2fl/fl P9
2h EdU CaBP DAPI
oEGL
EGL
ML
PC
50 µm
Plxnb2fl/fl
En1Cre;Plxnb2fl/fl
layer thickness (µm ± SEM)
NS
****
**
EGL
oEGL
ML
B
Ki67 Tag1 DAPI
Ki67
Tag1
Plxnb2fl/fl P9
En1Cre;Plxnb2fl/fl P9
oEGL
iEGL
C
2h EdU DAPI
24h EdU DAPI
Plxnb2fl/fl P8
En1Cre;Plxnb2fl/fl
increase of EdU+ cells in EGL (% ± SEM)
NS
D
24h EdU H3P
EdU
H3P
10 µm
24h EdU+ cells that are also H3P+ (% ± SEM)
**

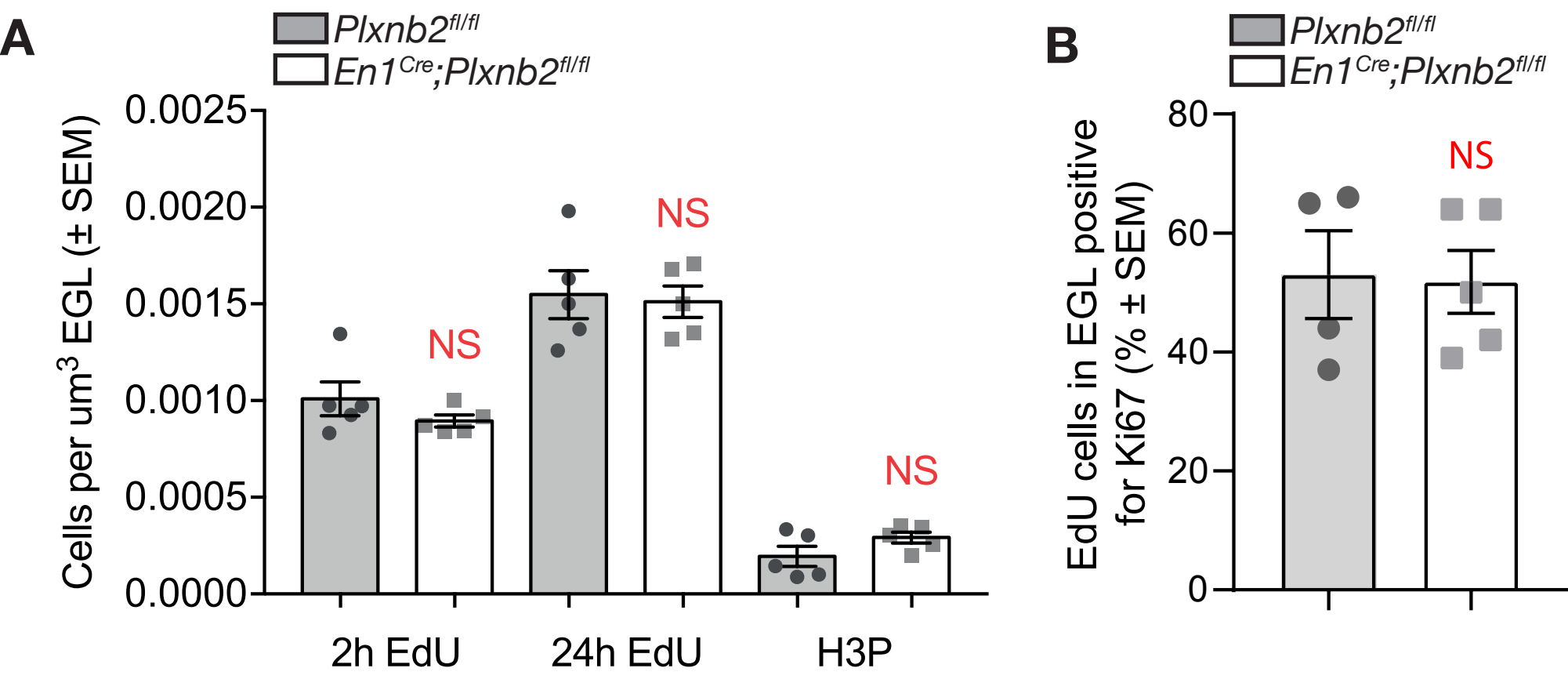
A
Plxnb2fl/fl
En1Cre;Plxnb2fl/fl
Cells per um3 EGL (± SEM)
0.0025
0.0020
0.0015
0.0010
0.0005
0.0000
NS
NS
NS
2h EdU
24h EdU
H3P
B
Plxnb2fl/fl
En1Cre;Plxnb2fl/fl
EdU cells in EGL positive for Ki67 (% ± SEM)
80
60
40
20
0
NS

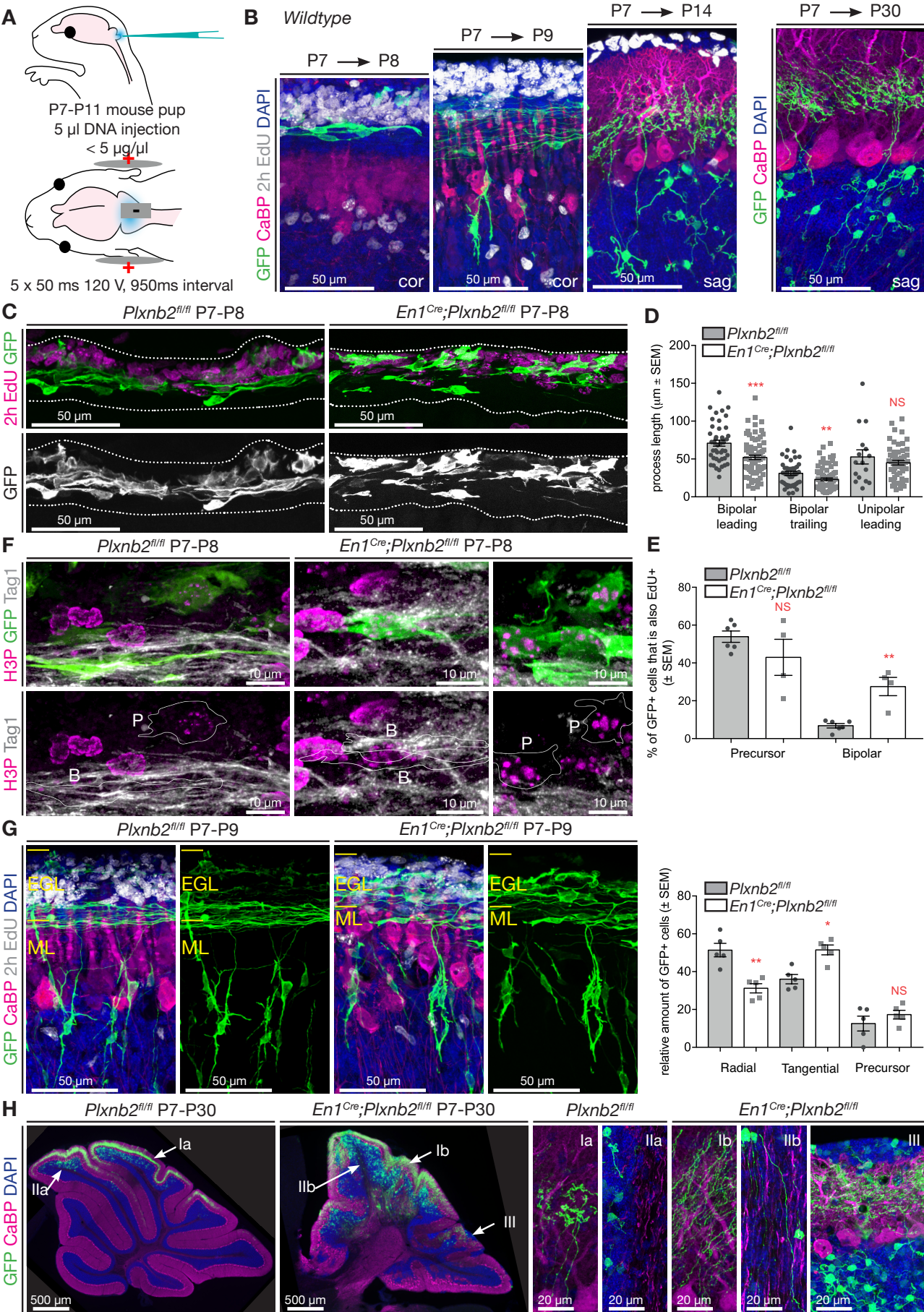
A
P7-P11 mouse pup
5 µl DNA injection
< 5 µg/µl
5 x 50 ms 120 V, 950ms interval
B
Wildtype
P7 → P8
P7 → P9
P7 → P14
P7 → P30
GFP CaBP 2h EdU DAPI
50 µm
cor
sag
C
Plxnb2fl/fl P7-P8
En1Cre;Plxnb2fl/fl P7-P8
2h EdU GFP
GFP
D
Plxnb2fl/fl
En1Cre;Plxnb2fl/fl
process length (µm ± SEM)
***
**
NS
Bipolar leading
Bipolar trailing
Unipolar leading
E
% of GFP+ cells that is also EdU+ (± SEM)
Precursor
Bipolar
F
H3P GFP Tag1
H3P Tag1
P
B
10 µm
G
GFP CaBP 2h EdU DAPI
EGL
ML
relative amount of GFP+ cells (± SEM)
Radial
Tangential
Precursor
H
Plxnb2fl/fl P7-P30
En1Cre;Plxnb2fl/fl P7-P30
Ia
IIa
Ib
IIb
III
500 µm
20 µm

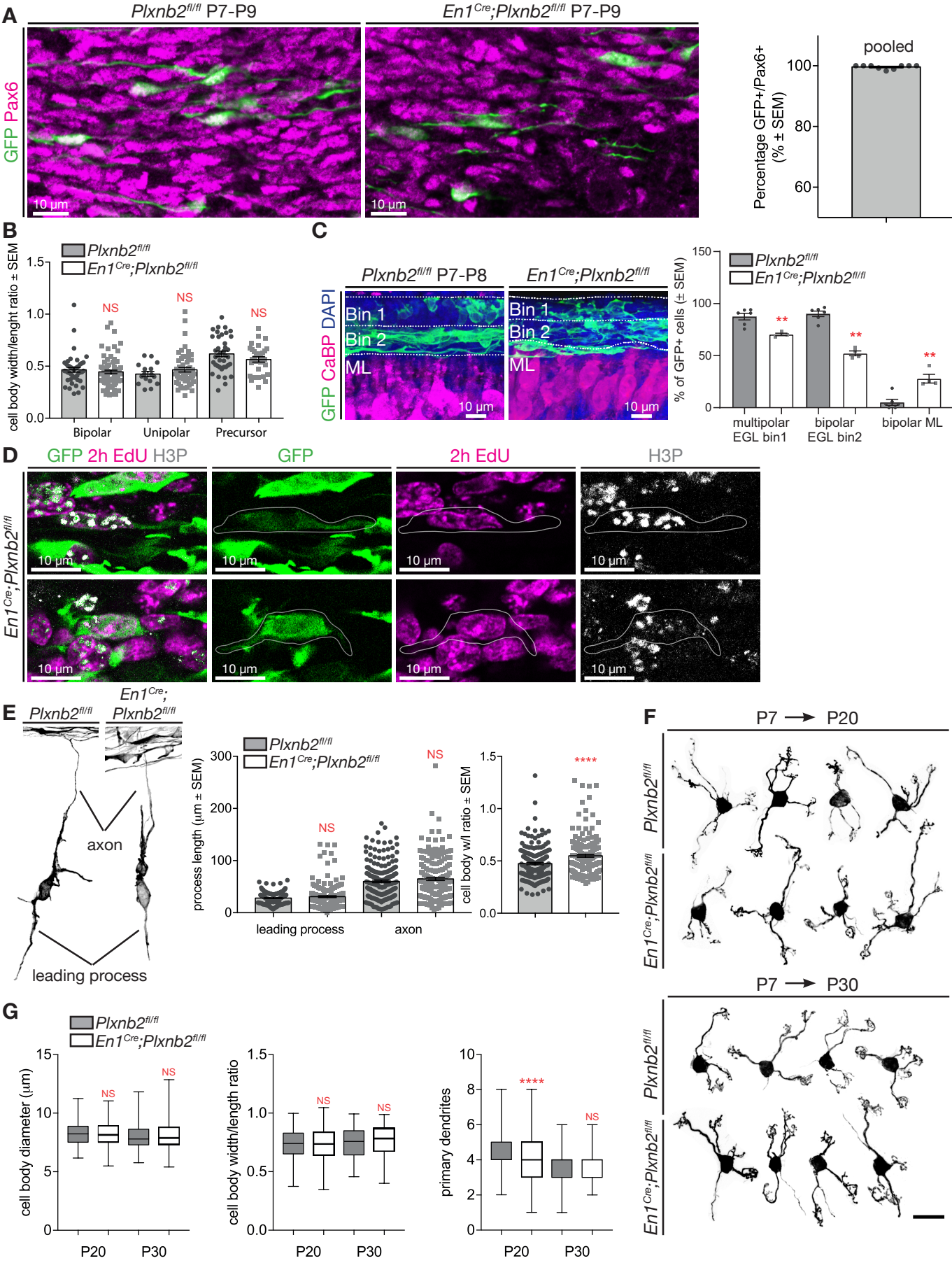
A
Plxnb2fl/fl P7-P9
En1Cre;Plxnb2fl/fl P7-P9
GFP Pax6
10 µm
pooled
Percentage GFP+/Pax6+ (% ± SEM)
100
80
60
B
Plxnb2fl/fl
En1Cre;Plxnb2fl/fl
cell body width/lenght ratio ± SEM
1.5
1.0
0.5
0.0
NS
Bipolar
Unipolar
Precursor
C
Plxnb2fl/fl P7-P8
En1Cre;Plxnb2fl/fl
GFP CaBP DAPI
Bin 1
Bin 2
ML
% of GFP+ cells (± SEM)
150
100
50
0
**
multipolar EGL bin1
bipolar EGL bin2
bipolar ML
D
GFP 2h EdU H3P
GFP
2h EdU
H3P
Plxnb2fl/fl
En1Cre;Plxnb2fl/fl
E
Plxnb2fl/fl
En1Cre; Plxnb2fl/fl
axon
leading process
process length (µm ± SEM)
300
200
100
0
NS
leading process
axon
cell body w/l ratio ± SEM
1.5
1.0
0.5
0.0
****
F
P7 → P20
P7 → P30
Plxnb2fl/fl
En1Cre;Plxnb2fl/fl
G
Plxnb2fl/fl
En1Cre;Plxnb2fl/fl
cell body diameter (µm)
15
10
5
0
NS
P20
P30
cell body width/length ratio
1.5
1.0
0.5
0.0
primary dendrites
10
8
6
4
2
0
****

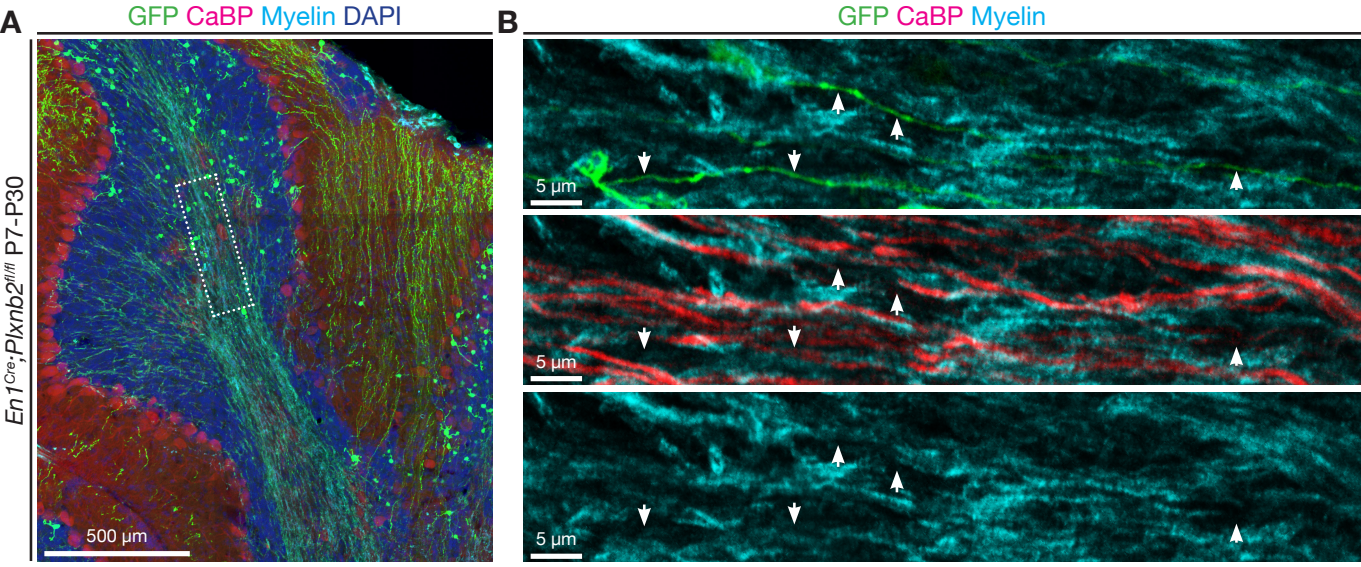
A
GFP CaBP Myelin DAPI
En1Cre;Plxnb2fl/fl P7-P30
500 µm
B
GFP CaBP Myelin
5 µm
5 µm
5 µm

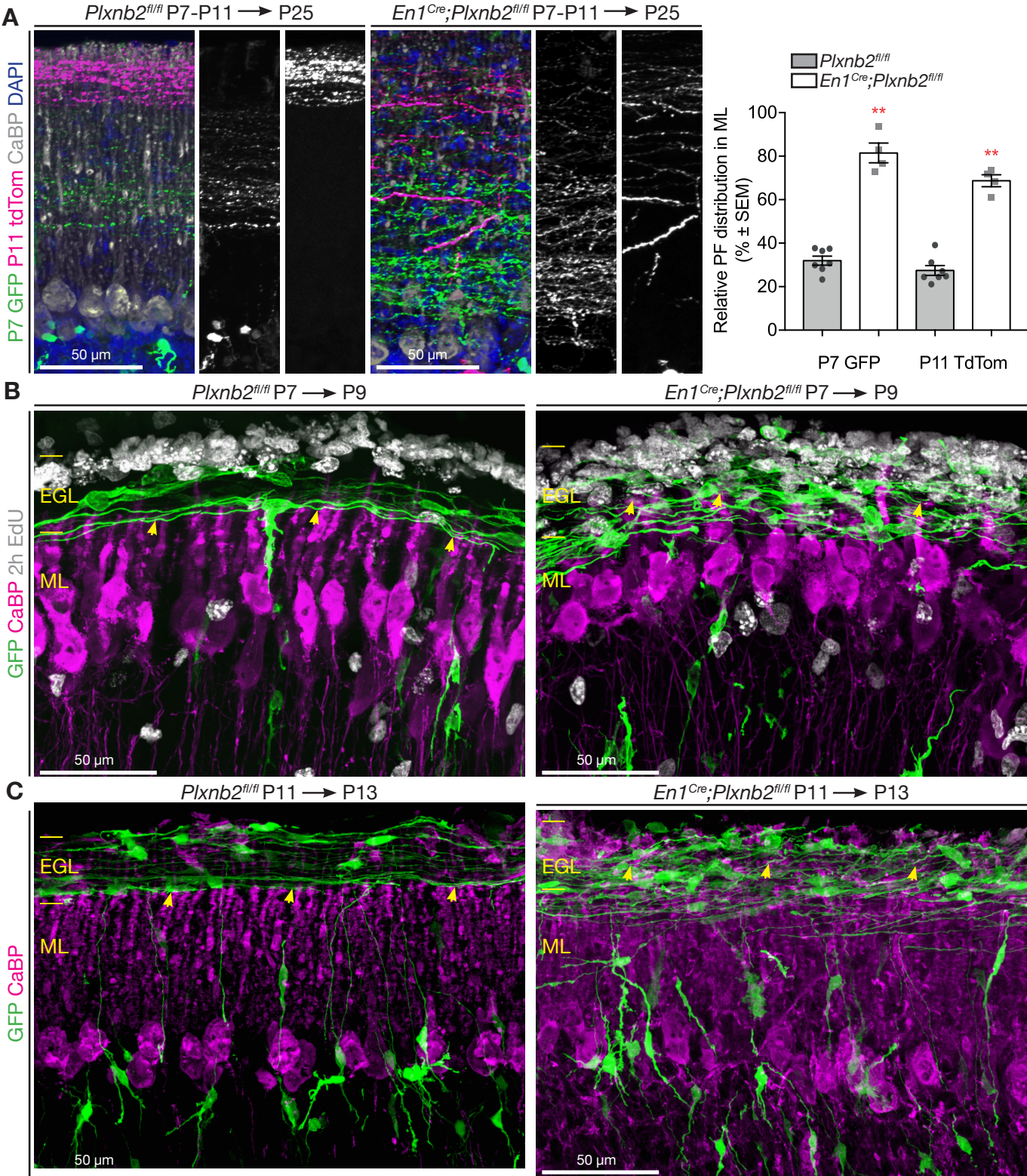
A
Plxnb2fl/fl P7-P11 → P25
En1Cre;Plxnb2fl/fl P7-P11 → P25
P7 GFP P11 tdTom CaBP DAPI
50 µm
50 µm
Plxnb2fl/fl
En1Cre;Plxnb2fl/fl
Relative PF distribution in ML (% ± SEM)
100
80
60
40
20
0
**
**
P7 GFP
P11 TdTom
B
Plxnb2fl/fl P7 → P9
En1Cre;Plxnb2fl/fl P7 → P9
GFP CaBP 2h EdU
EGL
ML
50 µm
EGL
ML
50 µm
C
Plxnb2fl/fl P11 → P13
En1Cre;Plxnb2fl/fl P11 → P13
GFP CaBP
EGL
ML
50 µm
EGL
ML
50 µm

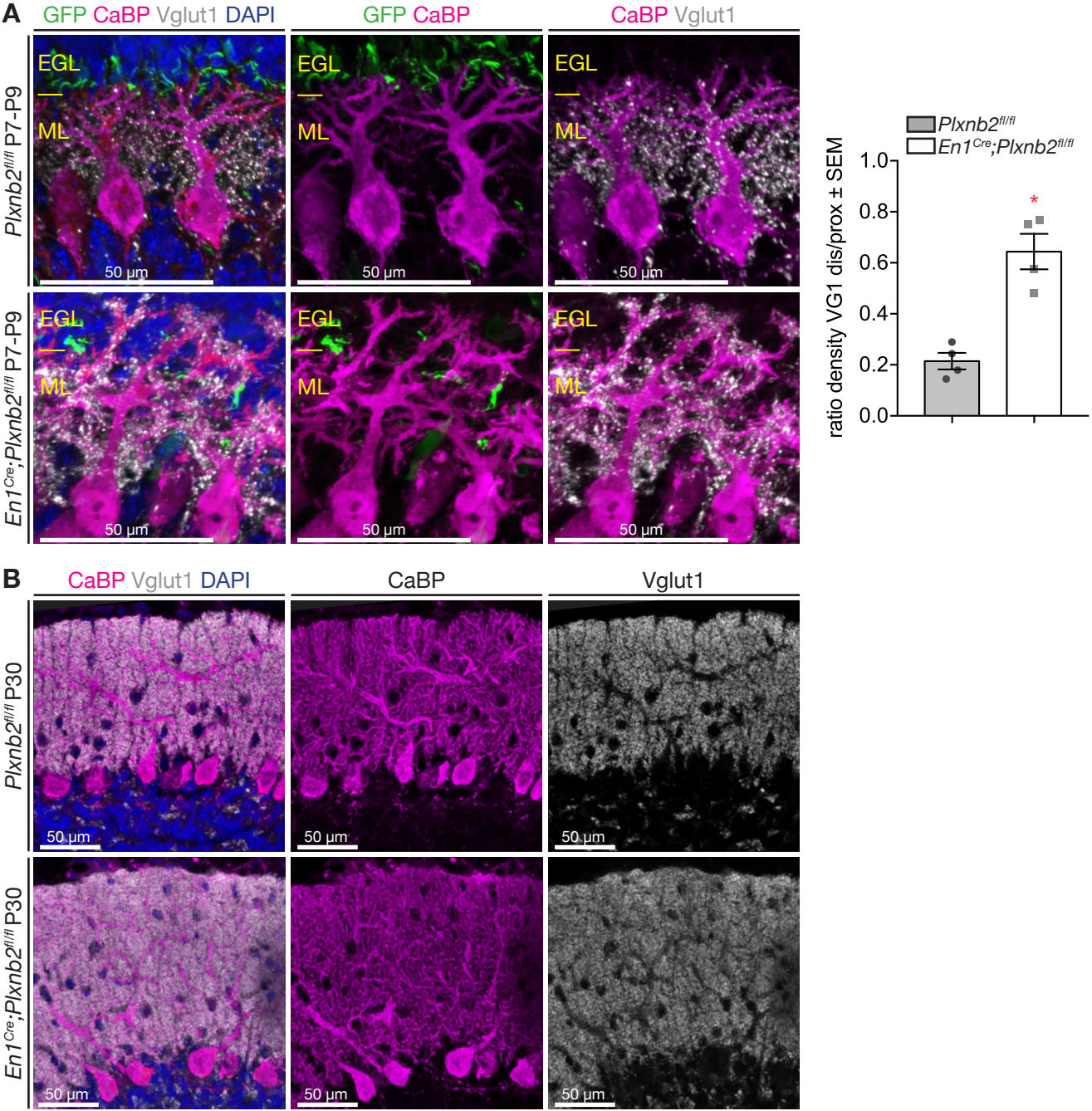
A
GFP CaBP Vglut1 DAPI
GFP CaBP
CaBP Vglut1
Plxnb2fl/fl P7-P9
En1Cre;Plxnb2fl/fl P7-P9
EGL
ML
50 µm
B
CaBP Vglut1 DAPI
CaBP
Vglut1
Plxnb2fl/fl P30
En1Cre;Plxnb2fl/fl P30
Plxnb2fl/fl
En1Cre;Plxnb2fl/fl
ratio density VG1 dis/prox ± SEM
1.0
0.8
0.6
0.4
0.2
0.0
*

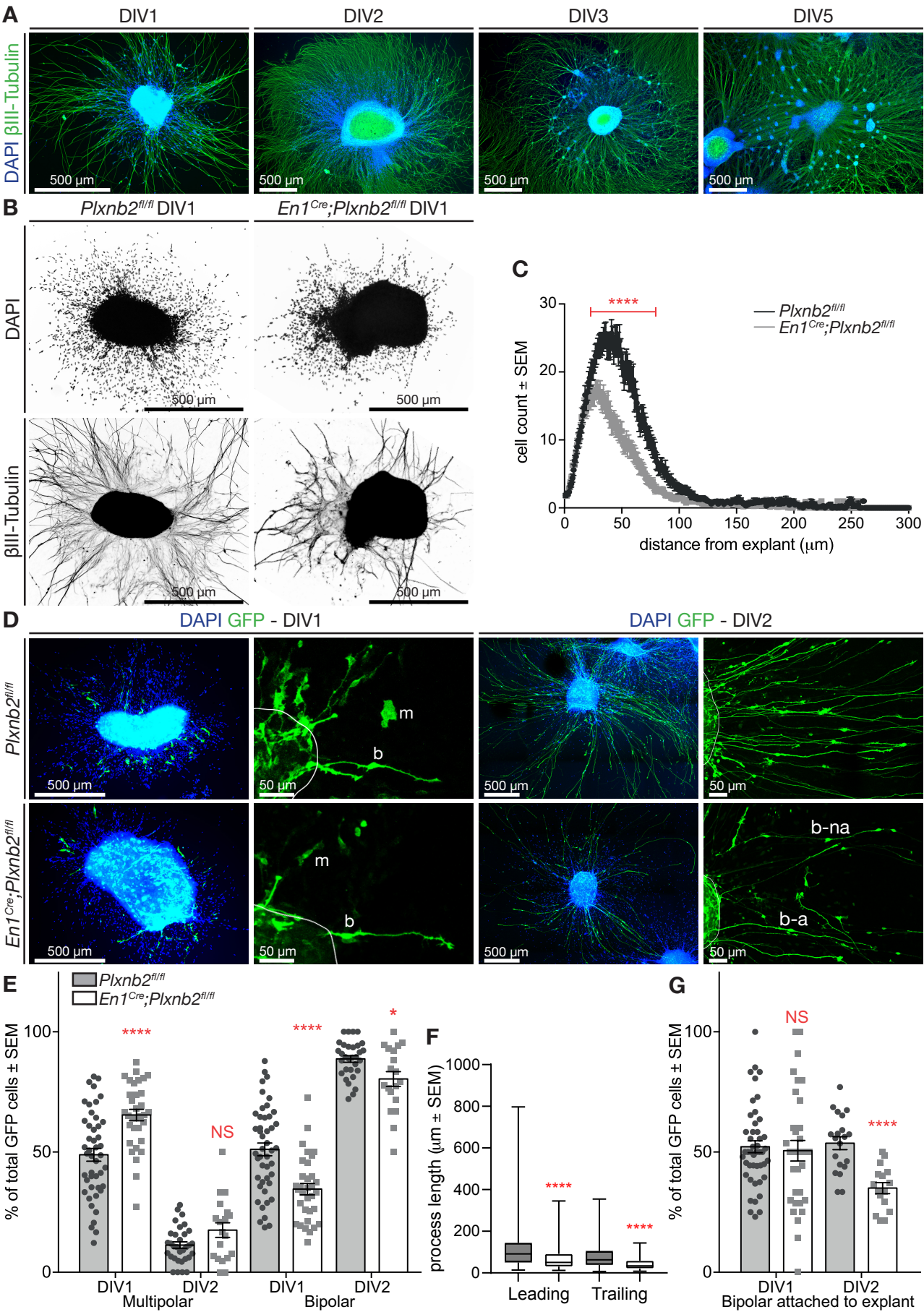
A
DIV1
DIV2
DIV3
DIV5
DAPI βIII-Tubulin
500 µm
B
Plxnb2fl/fl DIV1
En1Cre;Plxnb2fl/fl DIV1
DAPI
βIII-Tubulin
500 µm
C
****
Plxnb2fl/fl
En1Cre;Plxnb2fl/fl
cell count ± SEM
distance from explant (µm)
0
10
20
30
0
50
100
150
200
250
300
D
DAPI GFP - DIV1
DAPI GFP - DIV2
Plxnb2fl/fl
En1Cre;Plxnb2fl/fl
500 µm
50 µm
m
b
b-na
b-a
E
Plxnb2fl/fl
En1Cre;Plxnb2fl/fl
% of total GFP cells ± SEM
****
NS
****
*
DIV1
DIV2
DIV1
DIV2
Multipolar
Bipolar
F
process length (µm ± SEM)
****
****
Leading
Trailing
G
% of total GFP cells ± SEM
NS
****
DIV1
DIV2
Bipolar attached to explant

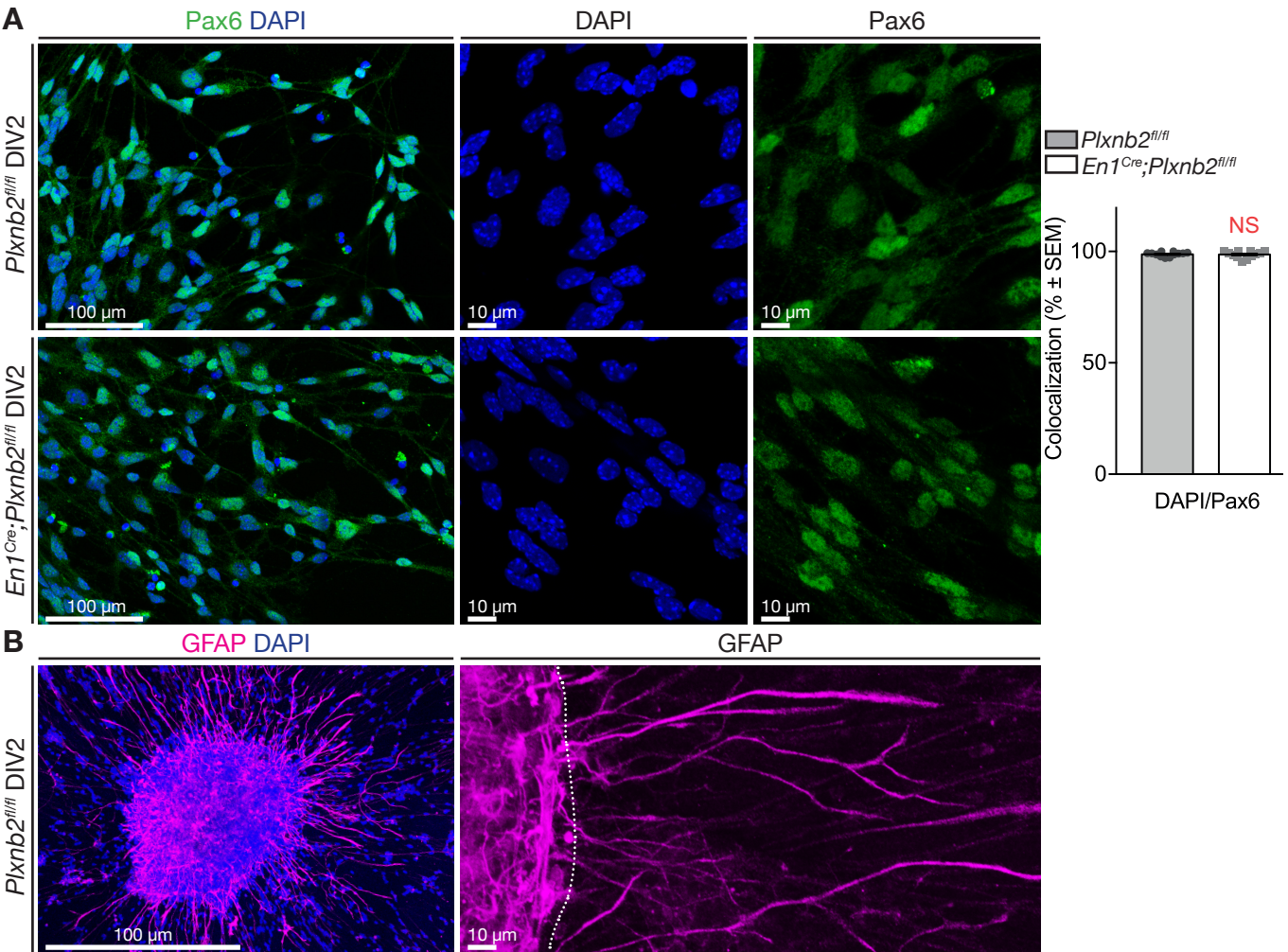
A
Pax6 DAPI
DAPI
Pax6
Plxnb2fl/fl DIV2
En1Cre;Plxnb2fl/fl DIV2
100 µm
10 µm
Plxnb2fl/fl
En1Cre;Plxnb2fl/fl
NS
Colocalization (% ± SEM)
100
50
0
DAPI/Pax6
B
GFAP DAPI
GFAP
Plxnb2fl/fl DIV2
100 µm
10 µm

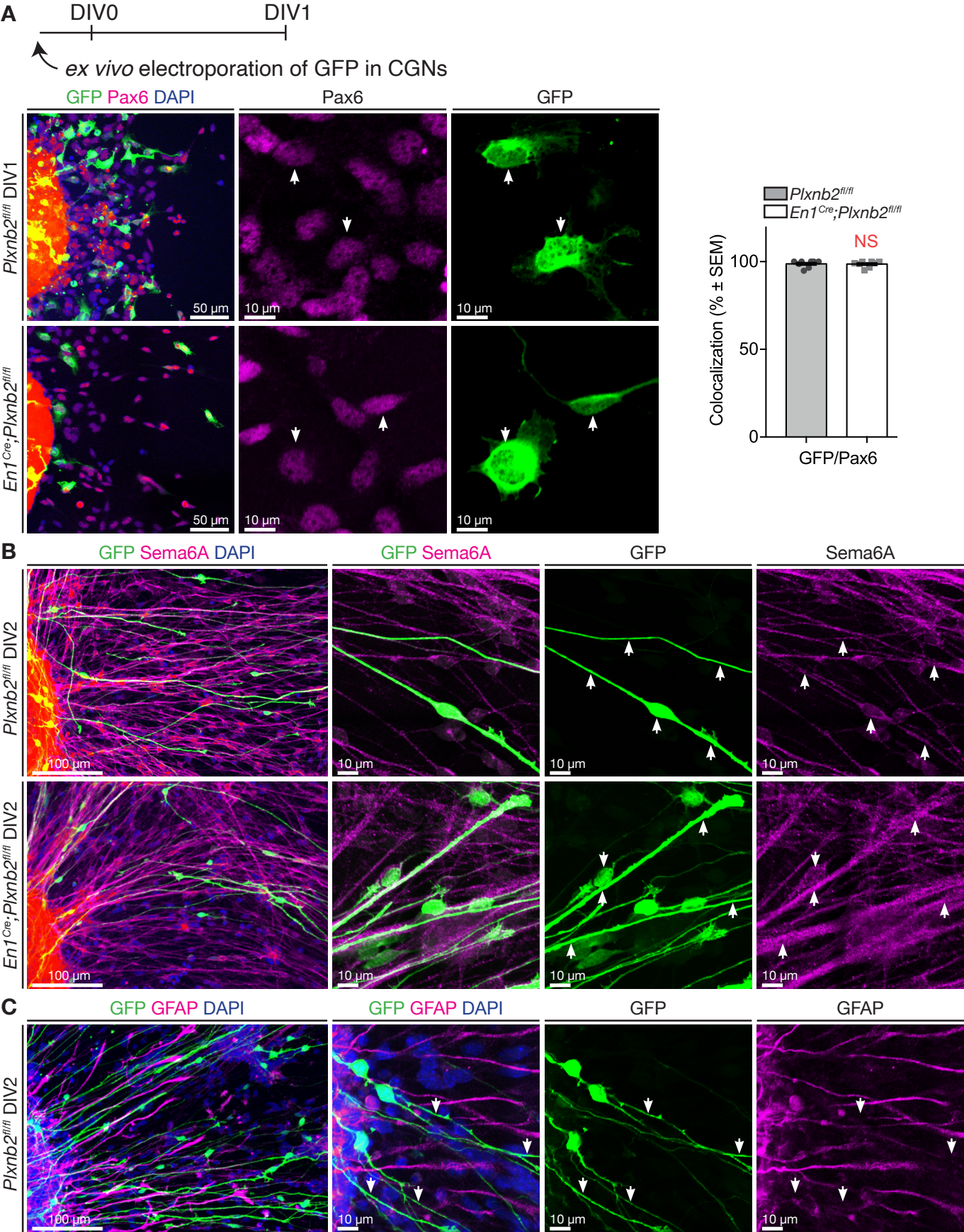
A
DIV0
DIV1
ex vivo electroporation of GFP in CGNs
GFP Pax6 DAPI
Pax6
GFP
Plxnb2fl/fl DIV1
En1Cre;Plxnb2fl/fl
50 µm
10 µm
Plxnb2fl/fl
En1Cre;Plxnb2fl/fl
NS
Colocalization (% ± SEM)
100
50
0
GFP/Pax6
B
GFP Sema6A DAPI
GFP Sema6A
GFP
Sema6A
Plxnb2fl/fl DIV2
En1Cre;Plxnb2fl/fl DIV2
100 µm
10 µm
C
GFP GFAP DAPI
GFP GFAP DAPI
GFP
GFAP
Plxnb2fl/fl DIV2

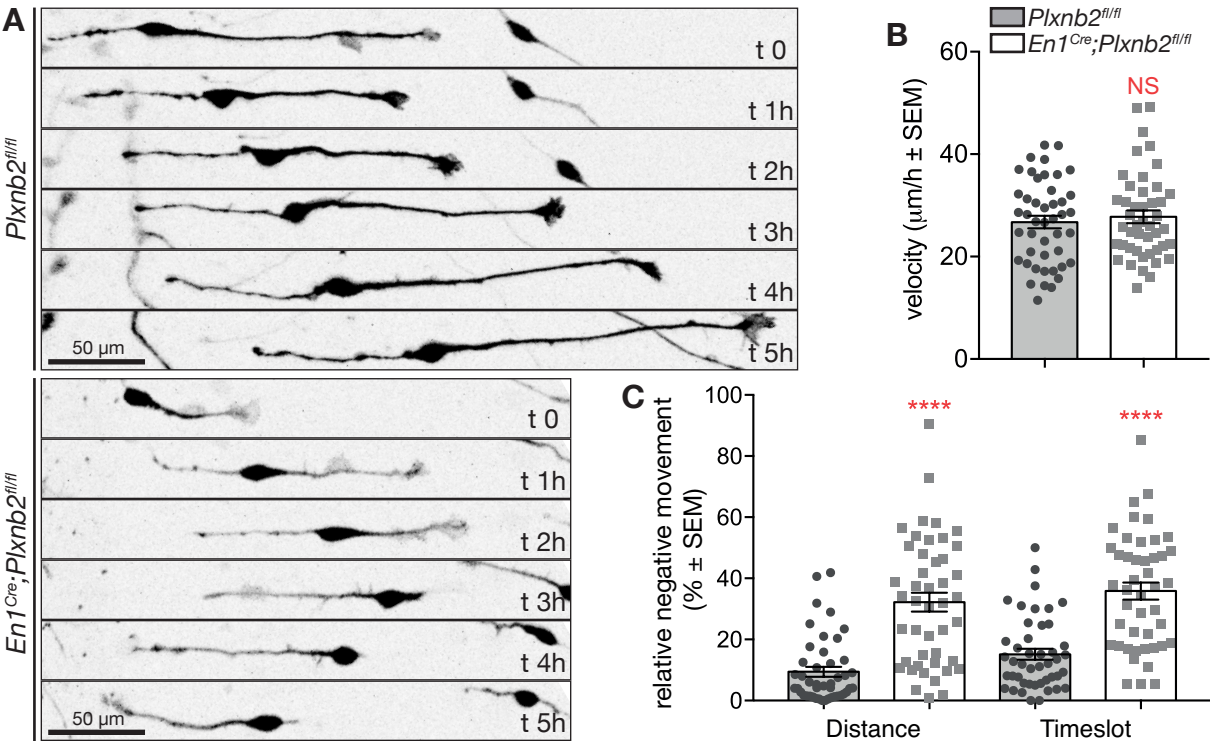
A
Plxnb2fl/fl
t 0
t 1h
t 2h
t 3h
t 4h
t 5h
50 µm
En1Cre;Plxnb2fl/fl
t 0
t 1h
t 2h
t 3h
t 4h
t 5h
50 µm
B
Plxnb2fl/fl
En1Cre;Plxnb2fl/fl
velocity (µm/h ± SEM)
60
40
20
0
NS
C
relative negative movement (% ± SEM)
100
80
60
40
20
0
****
****
Distance
Timeslot

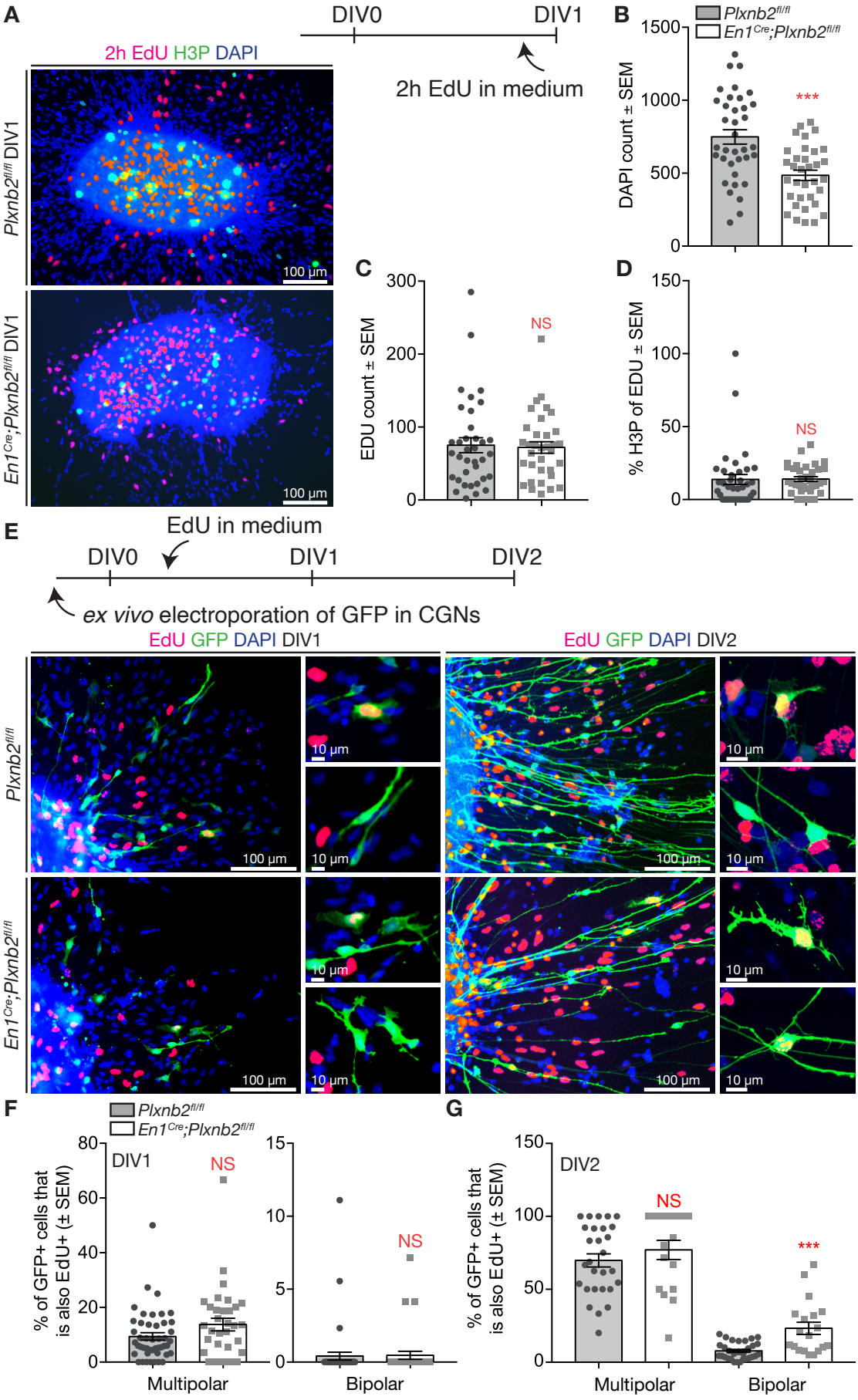
A
DIV0
DIV1
2h EdU in medium
2h EdU H3P DAPI
Plxnb2fl/fl DIV1
En1Cre;Plxnb2fl/fl DIV1
100 µm
B
Plxnb2fl/fl
En1Cre;Plxnb2fl/fl
DAPI count ± SEM
***
C
EDU count ± SEM
NS
D
% H3P of EDU ± SEM
NS
E
EdU in medium
DIV0
DIV1
DIV2
ex vivo electroporation of GFP in CGNs
EdU GFP DAPI DIV1
EdU GFP DAPI DIV2
10 µm
F
% of GFP+ cells that is also EdU+ (± SEM)
DIV1
NS
Multipolar
Bipolar
G
DIV2
NS
***

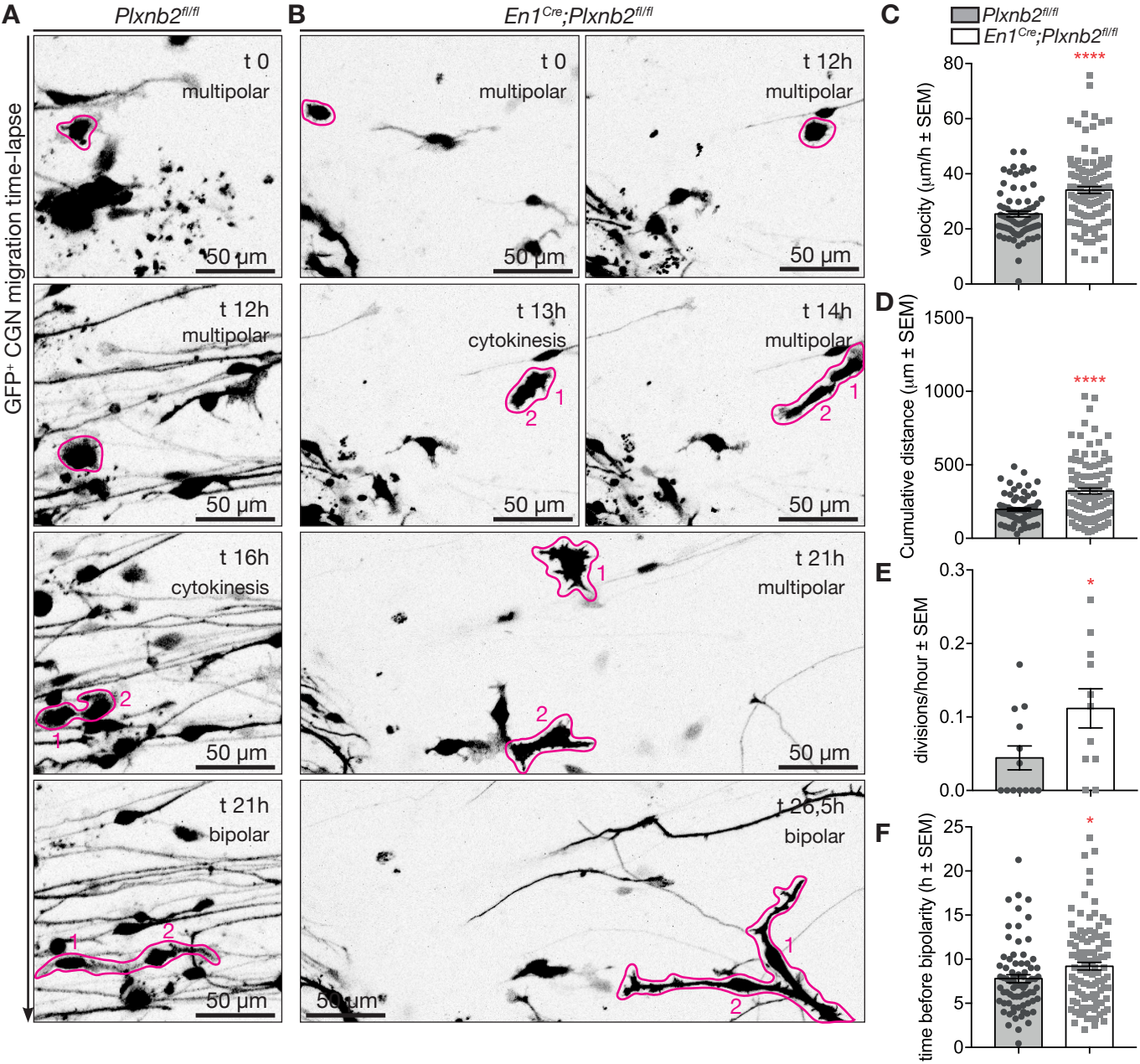
A
Plxnb2fl/fl
B
En1Cre;Plxnb2fl/fl
GFP+ CGN migration time-lapse
t 0
multipolar
50 µm
t 0
multipolar
50 µm
t 12h
multipolar
50 µm
t 12h
multipolar
50 µm
t 13h
cytokinesis
1
2
50 µm
t 14h
multipolar
1
2
50 µm
t 16h
cytokinesis
1
2
50 µm
t 21h
multipolar
1
2
50 µm
t 21h
bipolar
1
2
50 µm
t 26,5h
bipolar
1
2
50 µm
C
Plxnb2fl/fl
En1Cre;Plxnb2fl/fl
velocity (µm/h ± SEM)
80
60
40
20
0
****
D
Cumulative distance (µm ± SEM)
1500
1000
500
0
****
E
divisions/hour ± SEM
0.3
0.2
0.1
0.0
*
F
time before bipolarity (h ± SEM)
25
20
15
10
5
0
*

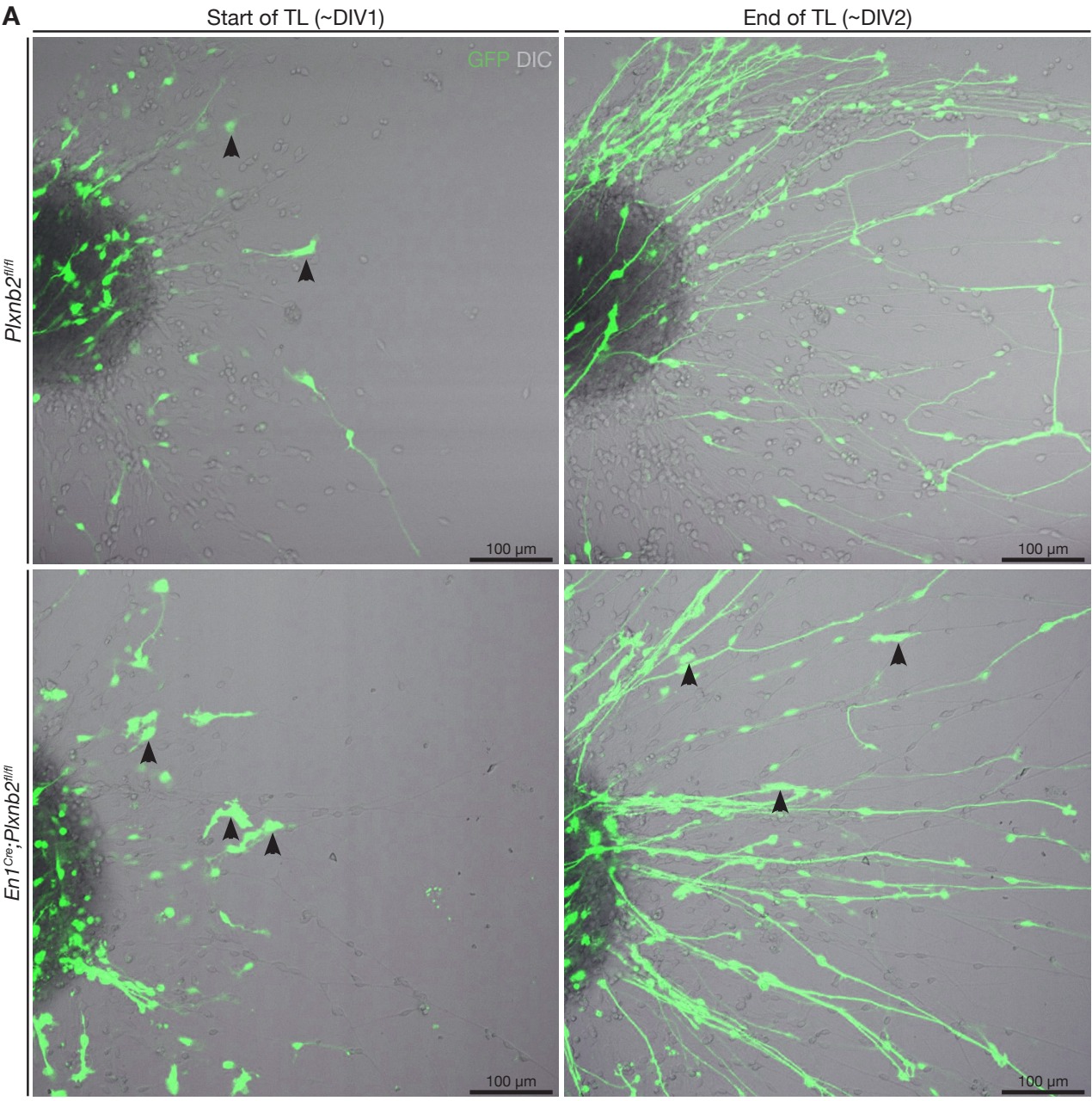
A
Start of TL (~DIV1)
End of TL (~DIV2)
Plxnb2fl/fl
En1Cre;Plxnb2fl/fl
GFP DIC
100 µm

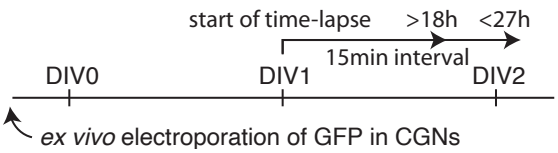
start of time-lapse
>18h
<27h
15min interval
DIV0
DIV1
DIV2
ex vivo electroporation of GFP in CGNs

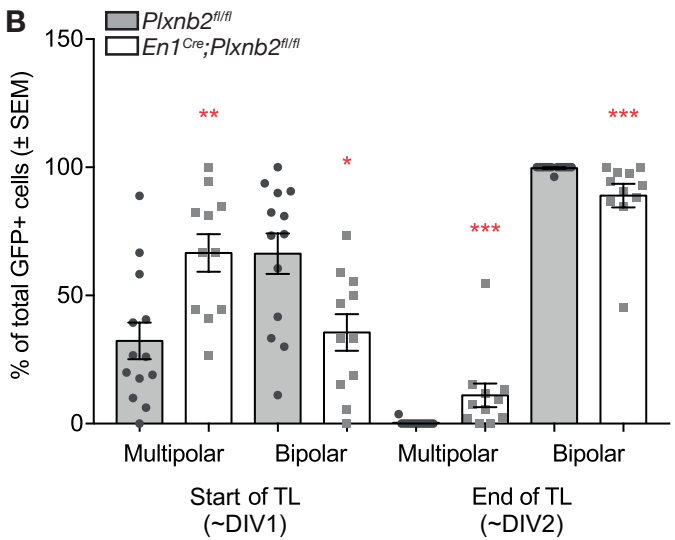
B
Plxnb2fl/fl
En1Cre;Plxnb2fl/fl
% of total GFP+ cells (± SEM)
150
100
50
0
**
*
***
***
Multipolar
Bipolar
Multipolar
Bipolar
Start of TL
(~DIV1)
End of TL
(~DIV2)